Fall 2021

Fine Points for Broad Bumps: The Extension of Rietveld Refinement for Benchtop Powder XRD Analysis of Ultra-Small Supported Nanoparticles

Jeremiah W. Lipp

FINE POINTS FOR BROAD BUMPS: THE EXTENSION OF RIETVELD REFINEMENT FOR BENCHTOP POWDER XRD ANALYSIS OF ULTRA-SMALL SUPPORTED NANOPARTICLES

By

Jeremiah W. Lipp

Associate of Science
Las Positas College, 2012

Bachelor of Science
Oregon Tech, 2016

Bachelor of Science
Oregon Tech, 2016

Submitted in Partial Fulfillment of the Requirements

For the Degree of Doctor of Philosophy in

Chemical Engineering

College of Engineering and Computing

University of South Carolina

2022

Accepted by:

John R. Regalbuto, Major Professor

John R. Monnier, Committee Member

Michael A. Matthews, Committee Member

Aaron K. Vannucci, Committee Member

Tracey L. Weldon, Interim Vice Provost and Dean of the Graduate School

ACKNOWLEDGEMENTS

First and foremost, I want to thank the Lord God, His Son Jesus, and the Holy Spirit. They have led me through every step of my education and have given me wisdom, knowledge, insight, and understanding. They have held on to me throughout every adversity and have pursued me whenever I strayed from them. Our relationship is the foundation for everything in my life. I could not have done any of this without them.

I want to thank my parents, Magnus and Lisa, who have sacrificed so much to raise my siblings and me well. They pulled double duty to teach us at home, and I owe my solid pre-college education to their time and effort. Their biggest gift will always be introducing me to the Lord.

I want to thank J.R., my fantastic adviser who has been a conduit of guidance, wisdom, and knowledge – for life as well as academics. Many significant obstacles have been overcome, thanks to his generosity and sacrifice.

I want to thank Dr. Monnier, my co-adviser, for incredibly practical advice. He is a true hands-on experimentalist, and I have benefitted from many of his stories. I especially appreciate his offer to assist in the birth of our eldest son.

I want to thank Frank Girgsdies, for welcoming me and for teaching me so much about x-ray diffraction. He has given me much insight and our conversations have been invaluable.

I want to thank John Tengco, who has always been the person to ask first about anything related to our research group. I appreciate his efforts to bring our group together.

I want to thank Qiuli Liu, Andrew Wong, Fahad Almalki, Jayson Keels, and Mehdi Zare for mentoring me and walking me through many of the finer points of chemical engineering.

I want to thank my classmate Greg Tate, for assisting me with many experiments and for helpful discussions.

I want to thank all my group members for their friendship and support. It has been enjoyable to work among you and to learn from you.

I want to thank Thomas Lunkenbein and the Electron Microscopy group for hosting me at the Fritz Haber Institute of the Max Planck Society.

I want to thank my office mates from the electronic structure group at the FHI: they made my stay very enjoyable.

I want to thank Ms. Margaret Colter for her friendship, prayers, and encouragement.

I want to thank those I have not mentioned, of whom there are many, for countless acts of encouragement, support, and sacrifice.

Finally, I want to thank my wife, Rachel. She is a true gift from the Lord, and a Proverbs 31 woman. She is a loving mother, a loyal friend, and a true partner.

ABSTRACT

The goal of this work is to demonstrate the capabilities of benchtop Bragg diffraction in characterizing ultra-small (< 2nm) nanoparticles. To this end we have established a method for accurately separating the background, adjusting for relevant intensity effects, and analyzing the results with Rietveld refinement. This method is applied to the characterization of six silica-supported “noble” metals under ambient conditions: Pt, Pd, Ir, Rh, Ru, and Au. Surprisingly, Bragg diffraction is capable of shining light on this difficult-to-characterize size region – revealing the propensity of these metal nanoparticles to oxidize at room temperature. Preliminary findings for future work are also discussed: extending our method to crystalline supports and fluorescent samples.

PREFACE

One of the most interesting – yet unrecognized – technologies ever introduced in science fiction is Star Trek's tricorder. Mr. Spock simply waves it in front of whatever he chooses to analyze, and it provides an immediate flow of information that is then used for making informed decisions. In this device and others like it, science fiction authors portray the ideal qualities for a characterization instrument: it is simple to use, quick to give results, provides accurate and detailed data, and is easy to interpret into meaningful information.

My most memorable graduate school seminar was given by Matthew Melis, a senior NASA scientist. Mr. Melis held a packed room of graduate students and faculty spellbound for nearly two hours as he showed picture after picture of the space shuttle program. He used those pictures to tell a story of the lessons learned from the Challenger and Columbia tragedies. My main take-away from this seminar was the importance of thorough characterization to engineering. The scientists and engineers of NASA would not have been able to identify the cause of the Columbia disaster without videos documenting the shuttle's ascent. Researchers and experimentalists cannot identify active catalytic sites without an accurate picture of the catalyst morphology. Graduate students and their advisors cannot confirm whether the catalysts they have synthesized are what they designed without somehow characterizing them.

Characterization is crucial. Yet it is especially challenging at the nanoscale. A general trend is that the smaller the thing to be analyzed, the more complex the instrument needed, the more difficult the analysis, and the more time required – moving away from the ideal tricorder and expending valuable resources. This dissertation addresses the characterization of ultra-small nanoparticles – covering sizes ranging from a few nanometers to clusters of atoms less than a nanometer across. Our goal was to make the characterization of these systems more “tricorder-like”, and we succeeded.

TABLE OF CONTENTS

LIST OF TABLES

LIST OF FIGURES

LIST OF SYMBOLS

I_0	Incident x-ray beam intensity
θ	Incident angle (Bragg angle)
$I'(\theta)$	Diffractogram intensity, normalized point by point to standard intensity
$I(\theta)$	Measured (raw) diffractogram intensity
$I_{0,\ measured}(\theta)$	Incident x-ray beam intensity measured (ideally) at the same time as $I(\theta)$
$I_{0,\ standard}$	Incident x-ray beam intensity value that all diffractograms are corrected to
μ	Linear absorption coefficient
ρ	Sample density
μ / ρ	X-ray mass attenuation coefficient
w_i	Mass fraction of element *i*
I_i'	Intensity reflected from phase *i*
c_i	Volume fraction of phase *i*
μ_i	Linear absorption coefficient for phase *i*
$\bar{\mu}$	Mean x-ray mass attenuation coefficient of all sample components
b_i	defined as $2B_i / 3$, i.e. two thirds the mean breadth of phase *i* particles
B_i	Mean breadth of particles from phase *i*
$\bar{l}$	Mean chord length of a particle
I_i'	Intensity of reflection from phase i

D	Linear size of a particle

INTRODUCTION

This dissertation makes use of the “manuscript style” – meaning that individual chapters are made up of papers that we either plan to submit or have submitted. Chapter 1 details the methods that allow laboratory x-ray diffraction instruments to access the world inhabited by “ultra-small” nanoparticles. Chapter 2 then applies this method to investigate the ambient oxidation of six noble metals: platinum (Pt), palladium (Pd), iridium (Ir), rhodium (Rh), ruthenium (Ru), and gold (Au). Chapter 3 provides preliminary results for future works: extending the methods of Chapter 1 to crystalline supports and samples containing fluorescent nanoparticles.

It may be helpful to note that Chapter 1 has a methods / protocols style. This is a newer paper style. It is solicited by the journal *Chemistry of Materials* for the purpose of fostering reproducibility in results by providing much more detailed descriptions of methods than is typically seen in a journal article. The journal requests that such an article be written with young scientists in mind – those who are directly working in the laboratories. The article featured in Chapter 1 meets these criteria. It seeks to provide young scientists with the relevant information needed to extend their x-ray diffraction analyses into the ultra-small. In line with their criteria the journal asks for “nuanced” descriptions and then deliberately sets no page limit. I do not think we disappoint.

CHAPTER 1

THE EXTENSION OF RIETVELD REFINEMENT FOR BENCHTOP POWDER XRD ANALYSIS OF ULTRA-SMALL SUPPORTED NANOPARTICLES[1]

[1] Lipp, J., Banerjee, R., Patwary, M. D. F., Patra, N., Dong, A., Girgsdies, F., Bare, S. R., and Regalbuto, J. R. To be submitted to *Chemistry of Materials*.

Abstract

We present a method for characterizing ultra-small (< 2nm) supported crystallites with benchtop XRD. Central to the method is an understanding of the intensity effects at play; these intensity effects and their corrections are discussed in depth. Background subtraction – long considered one of the main barriers to ultra-small crystal characterization – is solved by correcting the diffractogram of a separately measured support for the relevant intensity effects. Rietveld refinement is demonstrated to be an adequate analysis method for the general characterization of simple nano-systems. A 4.8% Pt / SiO_2 sample (1.3 nm, volume-weighted average) is used as a case study; it is found that the Pt spontaneously oxidizes under ambient conditions and consists of a metallic core surrounded by a PtO_2 shell. Both phases have average dimensions smaller than 1 nm. The XRD results also suggest lattice expansion of the Pt core as compared to bulk Pt.

Introduction

Ultra-small (<2nm) supported metal or metal oxide nanoparticles can now be routinely synthesized (Wong, et al. [1]). Supported particles below about 4 nm in size often exhibit interesting chemical properties such as a dramatic dependence of catalytic activity on particle size (Miller, et al. [2]). As particle sizes approach 1 nm, their dispersion (percent of surface atoms) nears 100%, thus allowing efficient catalytic reactions where all atoms can participate. However, systems with such small nanoparticles are difficult to characterize. It is commonly believed that nano crystallites less than 3 nm in size cannot be characterized with workhorse

benchtop x-ray diffraction (XRD) instruments; common reasons cited include low signal to noise and difficulty in separating the diffraction peaks from the background. Gallagher, et al. [3] reported that synchrotron radiation was required to characterize < 2 nm fully reduced nanoparticles; partially oxidized nanoparticles were reported to be unanalyzable. Without XRD, researchers must rely on alternate methods such as aberration corrected scanning transmission electron microscopy (STEM), x-ray absorption spectroscopy (XAS), and pair distribution function (PDF) analysis. These methods are more expensive and less accessible than XRD; for example, the latter two methods are typically performed at a synchrotron and thus typically require weeks to even months of advance notice before experiments can be performed.

There are several reasons why XRD should not be dismissed so quickly. The recent development of solid-state strip detectors for benchtop XRD instruments provides an improvement of signal to noise ratio by about two orders of magnitude over scintillation counters. A preliminary work with such an instrument demonstrated benchtop XRD characterization of 1.2 – 1.6 nm silica-supported gold particles at loadings as low as 0.33 wt% (O'Connell and Regalbuto [4]). Theoretically, the very smallest crystallites will give detectable signals. *Bazin, et al.* [5] numerically simulated the x-ray diffraction patterns from different sized platinum FCC and BCC nanoclusters. Their simulations used the Debye scattering equation with calculated atomic scattering factors from *Cromer and Liberman* [6, 7] and were simplified by assuming kinematic scattering only with no thermal disorder. The results showed that even nanoclusters as small as 9 to 13 atoms will

give a coherent signal, though the peaks are so broad that many of the individual peaks blend together. These results are consistent with the calculations of *Gallezot, et al.* [8] for electron diffraction of Pd, where nanoclusters as small as 6 atoms provided a signal. Indeed, zeolite-supported 13-atom Pd clusters were experimentally characterized by *Vogel, et al.* [9] using XRD with Debye Function Analysis (DFA) even without a solid-sate detector, and model particles as small as 13 atoms were routinely used in the DFA analysis of Pt and Ru nanoparticles (*Gnutzmann and Vogel* [10, 11-12]).

The purpose of this paper is to demonstrate the extension of benchtop powder XRD characterization to ultra-small nanoparticles using Rietveld refinement. With this goal in mind, this work presents the extra details that must be considered when characterizing ultra-small crystallites with powder XRD. Relevant intensity effects and their corrections for Bragg-Brentano diffraction are discussed, along with instructions for how the corrections can be implemented using Microsoft Excel and Topas[13]. Details for sample preparation are provided. A robust method is presented for subtracting the background from a supported nanocrystalline sample; this method is based on correcting an experimentally measured diffractogram of the support for differences in intensity effects between it and the nanoparticle containing sample. Finally, a case study of 4.8 wt% Pt / silica (volume weighted size average = 1.3 nm by scanning transmission electron microscopy, STEM) is examined under ambient conditions and analyzed with Rietveld methods. It will be shown that, contrary to the reports of Gallagher, et al. [3], benchtop XRD is capable of characterizing nanoparticles smaller than 2 nm with

Rietveld refinement, even when the nanoparticles are partially oxidized under ambient conditions and consist of individual crystal domains with dimensions less than 1 nm in size. These results are corroborated with STEM and XAS.

Intensity Effects in Bragg Brentano Geometry

As XRD peaks broaden, intensity effects that effect the x-ray flux scattered by the sample become more relevant. Even for highly symmetric FCC structures with few peaks, as crystallite sizes approach 1 nm and below the diffraction peaks blend together due to broadening and cease to provide useful information on their own. For less symmetric structures and/or samples with multiple phases the blending of peaks occurs at larger crystallite sizes. When individual peaks are no longer distinguishable, meaningful fits must be done against the entire diffractogram. Any effect that changes the relative intensities of the peaks will change the shape of the entire diffractogram. This is also true for the diffractograms of amorphous materials. For this reason, an accurate description of the nano-scale fits must account for all intensity effects that impact the diffractogram. Furthermore, any angle-dependent intensity effects affecting broad peaks must be scaled point-by-point to account for peak-pulling. Since intensity factors are so important for the analysis of samples with small crystallites, this work discusses the major contributing intensity effects that affect the diffraction patterns of ultra-small crystallites and presents how these effects can be accounted for. Table 1.1 lists the intensity effects discussed in this work. For clarity, these effects are separated into two categories: sample effects and instrument effects. Sample effects are caused by physical effects related to the sample, while instrument

effects are caused by the XRD instrument hardware. In some cases, this categorization is somewhat arbitrary (for example, beam spill results from both sample and instrument effects). However, the classification is especially useful when comparing samples. Except for the x-ray source intensity that may change over time, instrument effects are constant between samples provided that the instrument geometry (and sample holder) is not changed. In contrast, sample effects will vary from sample to sample.

In the following sections, the intensity effects will be discussed in the order that they must be addressed when analyzing XRD data, which matches the order shown in Table 1.1. The analysis takes place in three main steps. First, all diffractograms are normalized to an external standard. Second, the background of the nano-crystal diffractogram must be identified and separated. Third, the isolated nanocrystalline sample is analyzed with Rietveld refinement.

Table 1.1. XRD intensity effects discussed in this work. Sample effects are tabulated in the shaded rows; instrument effects are unshaded. The peak pull is calculated for a Pt (111) peak (Cu K-α) with size broadening corresponding to a 0.87 nm domain size. A negative value indicates an apparent shift to lower angles.

Intensity effect	**Angle dependent**	**Peak Pull [° 2θ]**
X-ray source tube	Sometimes*	Negligible
Sample holder (sample-independent)	Yes	N/A
Sample holder (sample-dependent)	Yes	N/A
Absorption	No	N/A
Finite sample thickness	Yes	- 0.10°
Beam spill	Yes	+ 0.30°
Lorentz-Polarization	Yes	- 1.06°
Surface microabsorption (surface roughness)	Yes	+ 0.3°

*Depends on how quickly the source intensity changes. If the source intensity changes significantly during a single XRD scan, then the effect on the diffractogram will be angle dependent.

Step 1: Normalizing for the incident x-ray beam intensity I_0

The first intensity effect to account for is the incident x-ray beam intensity I_0. The diffractogram signal that reaches the detector is directly proportional on the flux of x-rays emitted by the x-ray source. For the Rigaku Miniflex II benchtop XRD used in this work, the emitted x-rays show a significant drift in I_0 over time (Figure 1.1). The main source of this drift is believed to be the varying temperature of the cooling water used to cool the x-ray tube (our instrument uses a closed-loop chiller which does not include temperature control). As the cooling water changes temperature the x-ray tube temperature also changes; this is believed to cause the observed change in intensity. Different XRD instruments will have different amounts of x-ray source drift over time; even instruments with finely tuned temperature control of the x-ray tube will see a slow decrease in intensity over the course of weeks to months as the x-ray tube ages.

The problem introduced by drifting I_0 is that it introduces errors when comparing samples. To fully analyze a single supported nanoparticle-containing sample, several experiments must be conducted: the sample itself, the pure support, the empty sample holder, and (ideally) the sample holder filled with a mixture of highly crystalline materials that contains equal x-ray mass attenuation to the nanoparticle sample. If these diffractograms are measured at different x-ray source intensities, then errors will be introduced when comparing the samples during analysis – unless the differences in I_0 can be accounted for.

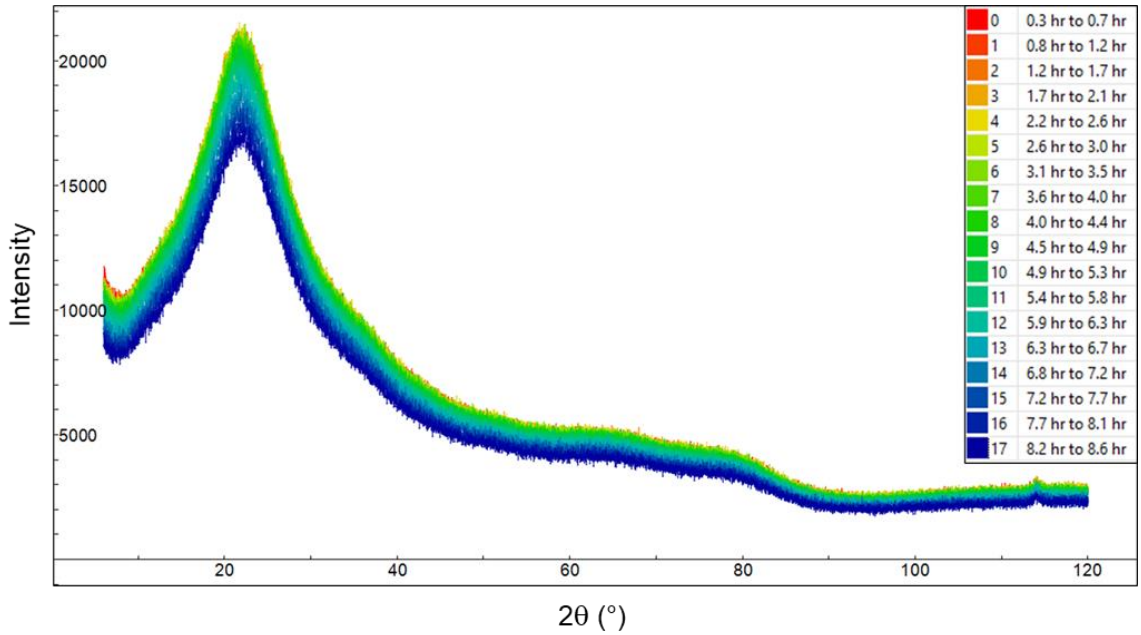

Figure 1.1. Example of x-ray source intensity drift over time. The back-to-back diffractograms display a slow increase in intensity for the first five runs; the remaining runs exhibit a more rapid decrease in intensity.

Changes in x-ray incident intensity are often accounted for by normalizing separate diffractograms to some common point between the diffractogram (Gallagher, et al. [3]). This works well when x-ray intensity drift is negligible over the course of measuring a single diffractogram and when the common point is truly equivalent between samples. However, with nano crystallites the diffraction peaks are so broad that there tends to be no part of the diffractogram for which they do not contribute signal. Furthermore, other intensity effects are present between all samples (be they nano or bulk crystallites). Scaling the diffractogram to a common point incorrectly includes these intensity factors and introduces errors in the background subtraction.

The most accurate way to account for drifting I_0 is to monitor the x-ray intensity over time and to adjust all measured diffractograms accordingly. The

adjustment is a straightforward normalization to a standard reference. If the change in source intensity is significant during the measurement of a diffractogram, then the measured I_0 is angle dependent and should be corrected on a point-by-point basis:

$$I'(\theta) = \frac{I(\theta)}{I_{0,\ measured}(\theta)} \times I_{0,\ standard} \qquad \text{Eq. 1}$$

where $I'(\theta)$ is the entire diffractogram normalized point-by-point to a standard intensity value $I_{0,standard}$, $I(\theta)$ is the measured diffractogram intensity, and $I_{0,\ measured}(\theta)$ is the measured intensity of a standard material (in our case a NIST 1976c corundum intensity standard). Figure 1.2 (A) depicts the result after adjusting for drift and averaging multiple runs together for a series of Au samples supported on silica. It is important to note that after properly adjusting for changes in I_0 other intensity effects become evident. Figure 1.2 (A) shows that after correcting for I_0 the silica peaks (near 2θ = 22°) still have significantly different intensities. These differences are due to other angle-dependent effects. Herein all diffractograms were first corrected for intensity drift against the (1 0 4) reflection of a NIST 1976c intensity standard.

Step 2: Accurately estimating the background

After normalizing I_0 for all samples using an intensity standard, the coherent scattering of the nano-crystals must be separated from the rest of the diffractogram. For a single nano-sample, this is achieved by adjusting the diffractogram of the pure support to match that of the support in the nano-crystal

sample. For comparing a series of samples, one sample is chosen as the standard and the support contributions of all other samples are adjusted to it. The process is illustrated for a series of silica-supported gold samples in Figure 1.2. For each of the samples to be corrected, the portion of the diffractogram corresponding to the contribution of the sample holder must first be identified (Figure 1.2A) and subtracted (Figure 1.2B). Once this is done, the remaining portion of the diffractograms (corresponding to the isolated sample) need to be corrected for two sample effects. The first effect is the absorption of x-rays by the samples. The second effect is the finite thickness of the samples. These two effects are related to one another and must be accounted for together. Once the diffractograms have been adjusted for these effects (Figure 1.2C), the sample holder contribution of the "standard" sample is added back to each diffractogram to preserve proper statistics for the upcoming analysis with Topas (Figure 1.2D). The ideal result will be a set of samples with the same sample holder contribution and identical intensity corrections resulting from sample effects. Figure 1.2D shows that once corrected, the intensity and width of the main amorphous silica peak (22° 2θ) for all the samples are in close agreement. The diffractograms of the pure treated supports now provide a clear baseline above which gold peaks of increasing weight loading can clearly be seen. This baseline is the "background" to be used during the analysis in Topas.

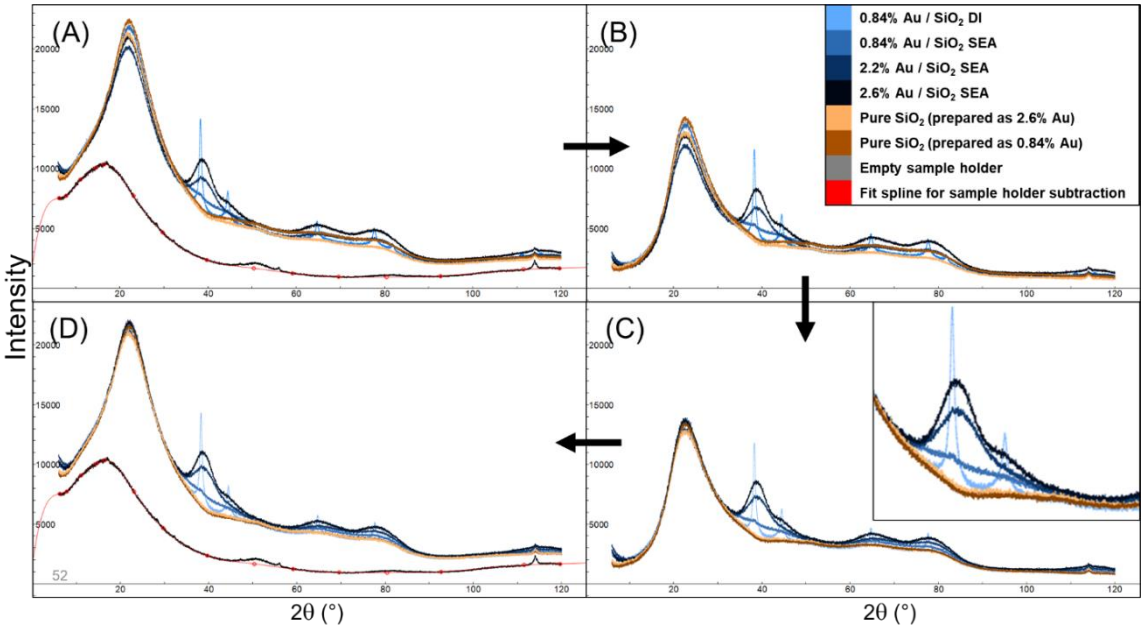

Figure 1.2. A series of Au / silica (Aerosil 300) samples demonstrating the effectiveness of accounting for sample mass, x-ray mass attenuation, and finite thickness intensity factors. Samples were prepared with either dry impregnation (DI) or strong electrostatic adsorption (SEA). (A) Data normalized to a common source intensity. Each diffractogram is the average of six runs taken at 5° min^{-1}. (B) Diffractograms after subtracting the background (fit spline). (C) Background-subtracted diffractograms after correcting for differences in x-ray absorption and finite sample thickness. (D) Corrected diffractograms with the background added back (in preparation for Rietveld analysis).

Sample holder

The sample holder can contribute both sample dependent scattering and sample-independent scattering to a diffractogram. Accurate background subtraction relies on quantifying these contributions. The extent of the contributions will depend on the instrument hardware and sample holder dimensions. For the Rigaku Miniflex II and zero background holder used for this work, there is a significant sample-independent contribution to each diffractogram, and a smaller sample-dependent contribution (Figure 1.3). The reason for this can be seen in Figure 1.4 where the x-ray beam is shown covering a large portion of

the silicon mirror that surrounds the sample cavity. This single crystal of silicon is cut at a low index plane to remove sharp peaks from appearing in the diffractogram. We propose that the surface of the silicon is oxidized and gives a diffuse silica bump that is skewed in shape and position by the different amounts that are illuminated by the XRD beam at varying incident angles. The diffractogram contribution coming from the surface of the mirror will be constant for all samples. Figure 1.3 shows that for our instrument geometry and sample holder this constant contribution (that includes the primary beam scatter from the x-ray source onto the detector, shown in red) from the sample holder can be quite significant (black). The sample-dependent contribution (grey) comes from the silicon/silica at the bottom of the cavity; this contribution is greatest when there is no sample in the holder and decreases when it is covered by sample. The contribution will be lowest when covered by a sample that highly absorbs the x-rays.

The sample holder contributions can be determined by measuring a series of diffractograms. The diffractogram of the empty sample holder provides the combined sample-independent contribution and maximum possible sample-dependent contribution (sum of the red, black, and grey shaded regions in Figure 1.3). The sample-independent region is obtained by filling the sample cavity with a “heavy” sample that completely shields the bottom of the sample holder from the x-rays. This sample must be highly crystalline so that the diffracted peaks can be separated from the sample holder contribution (see the supplementary information for a discussion on how to determine if a sample will function as a highly crystalline reference). The diffractogram of the sample holder filled with the “heavy” sample

is then processed to separate and remove the sample's peaks from the baseline; once isolated the resulting baseline corresponds to the sample-independent holder contribution (sum of the red and black shaded regions in Figure 1.3). By subtracting the sample-independent contribution from the empty sample holder contribution, the sample-dependent region of the sample holder is obtained. To identify the most accurate estimate of the sample-dependent contribution, a third highly crystalline sample could be made that would have the same x-ray mass attenuation as the sample to be corrected for sample effects. This could be achieved by mixing a lightly x-ray absorbing sample with a heavily x-ray absorbing sample, as long as both samples are highly crystalline.

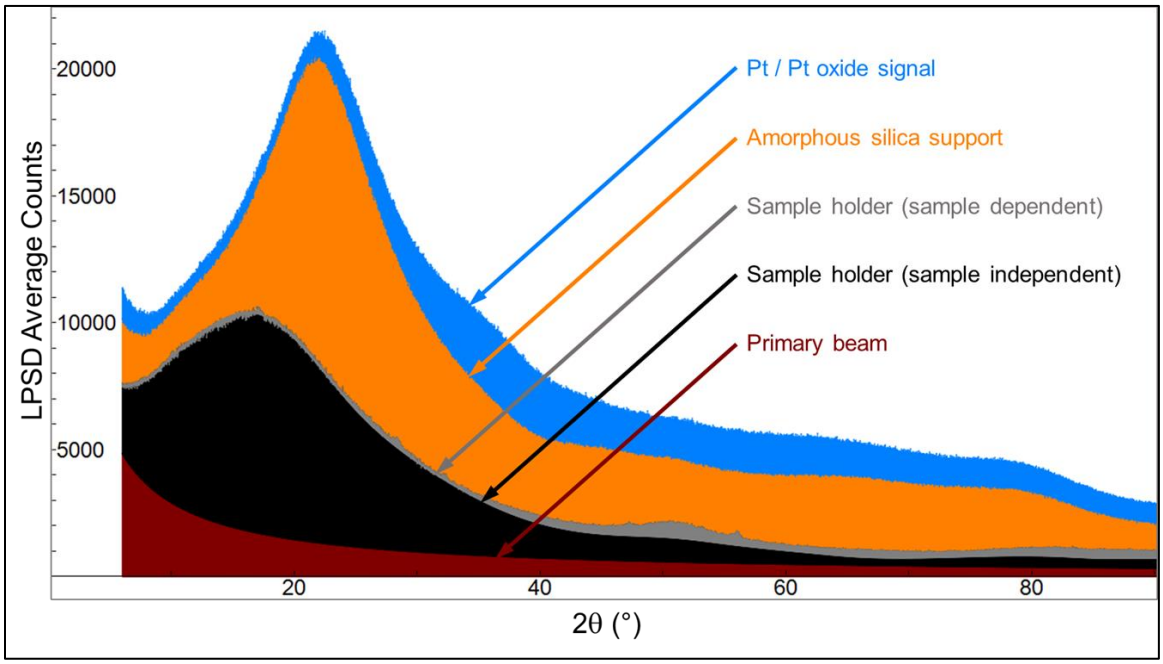

Figure 1.3. 4.8% Pt / silica (Aerosil 300) diffractogram components. Except for the primary beam scatter (red), all the portions of the diffractogram were obtained by separate diffraction measurements, with adjustments for drift and sample intensity effects. The intensity of the primary beam scatter has been arbitrarily chosen and displayed to remind the readers that the sample independent sample holder diffractogram contains the primary beam scatter, therefore changing the

atmosphere through with the x-ray beam travels (for example in an in-situ measurement) may also have an effect on the diffractogram.

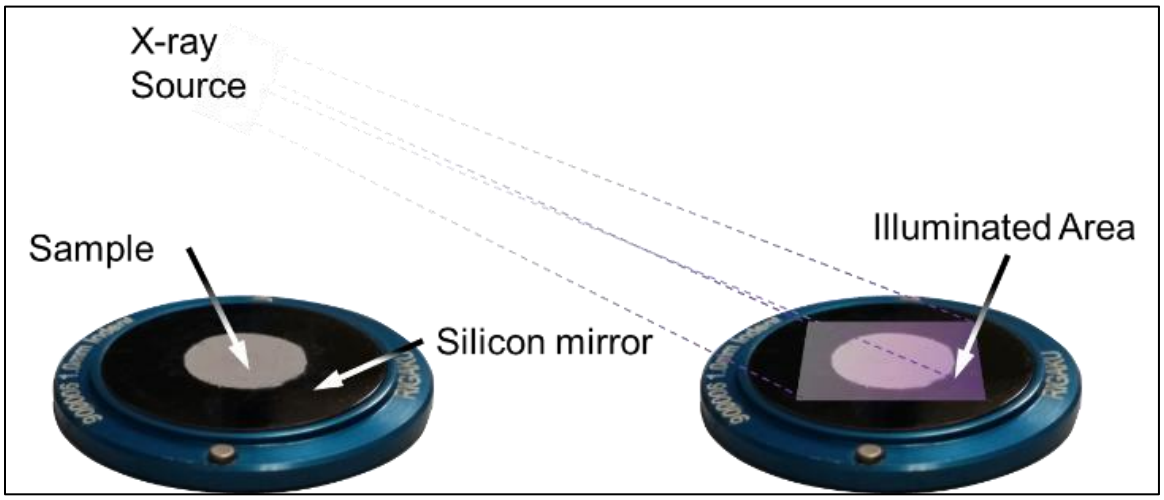

Figure 1.4. Irradiation of a “zero background” sample holder in the Rigaku Miniflex II.

The reason why it is so important to identify the sample holder’s diffractogram contribution is that it must be subtracted from the diffractogram *before* the sample effects can be corrected. The sample-independent contribution from the sample holder depends only on the incident beam intensity, the sample holder itself, and the atmosphere inside the diffractometer. It does not depend on the sample in the holder, so including it in the adjustment for sample effects will introduce errors. These errors will be especially prominent if the sample holder contribution contributes a significant portion of the entire diffractogram (as is the case in Figure 1.3). The sample-dependent contribution from the sample holder will be affected by the differences between samples, but not in the same way as the sample itself. For this reason, it should also be subtracted before the sample effects are corrected.

Once the sample effects have been adjusted to match those of the sample chosen to be the “standard”, the sample holder contribution of the “standard” sample should be added to the corrected sample diffractograms before analysis in Topas. This allows the diffractogram of the nanocrystalline sample to remain unchanged – a desirable trait for an accurate analysis in Topas. Topas works best when operating with raw data; users are encouraged not to adjust their experimental data outside of simply scaling it before importing it into Topas. This is because of the relationship between noise amplitude and total intensity, which Topas uses to calculate errors and fit the data. To identify the background, adjustments must be made to match the diffractograms of the pure supports to those of the supported nanocrystalline samples. By choosing the nanocrystalline sample as the standard and adjusting the pure support to match it, the nanocrystalline data can be preserved in its original form for the analysis in Topas. Since the treated support is used only for identifying the background, the adjustments made to it will not affect the quality of the fit.

Absorption

The attenuation of x-rays as they travel through a sample (also known as x-ray mass absorption) is related to the linear absorption coefficient μ [cm^{-1}], or $\bar{\mu}$ (the average coefficient for a combination of elements). Figure 1.5 shows three samples containing equal amounts of amorphous silica, but physically mixed with different ratios of two crystalline powders: quartz (SiO_2) and tin (Sn). The sample mixed only with quartz has the lowest $\bar{\mu}$ (11.7 cm^{-1}) and therefore the most intense amorphous silica diffractogram (see the broad peak centered around 21° 2θ). The

sample mixed only with tin has the highest $\bar{\mu}$ (17.8 cm^{-1}) and therefore significantly lower intensity of the amorphous silica. Figure 1.6 shows the x-ray mass attenuation coefficients (μ / ρ [cm^2 g^{-1}]; ρ is the density of the sample) by element for Cu K-α radiation; the silicon and oxygen present in quartz have much lower mass attenuation coefficients than that of tin. The physical significance of the mass attenuation coefficient is that x-rays will not pass through elements with higher coefficients as easily as they do through elements with lower coefficients. As x-rays travel through the samples of Figure 1.5, less x-rays pass through the tin than through the quartz. Fewer x-rays are therefore available to scatter from the silica in the tin-containing sample than in the quartz-containing sample, and the ultimate result is that the silica diffractogram is less intense in the tin-containing sample.

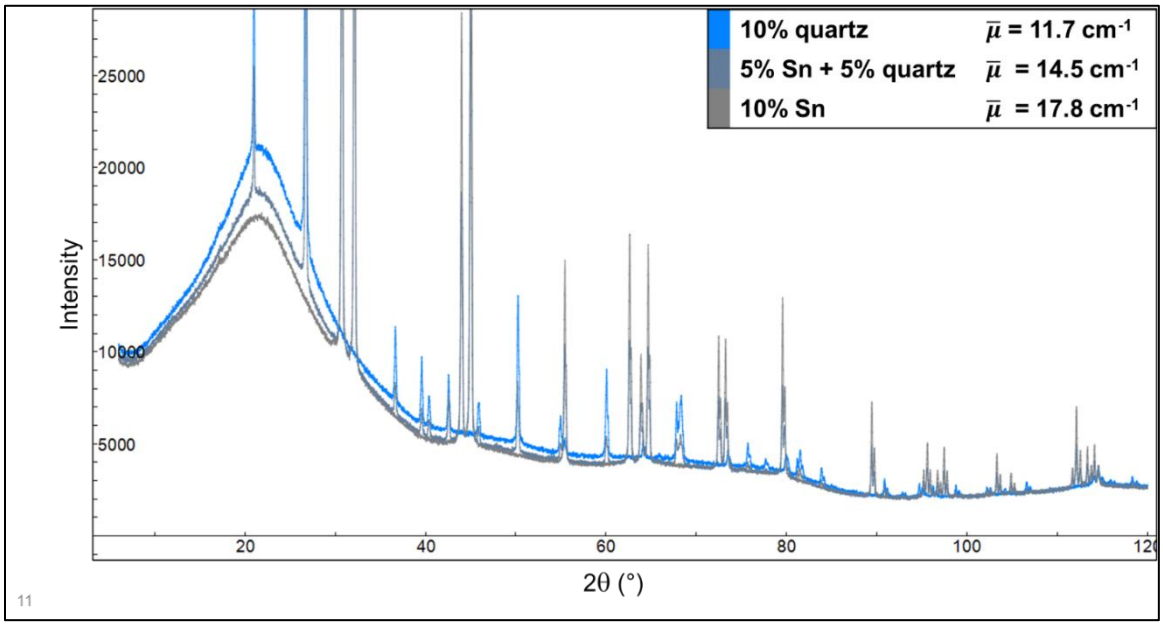

Figure 1.5. Demonstrating the effect of different amounts of microabsorption on equal loadings of amorphous silica.

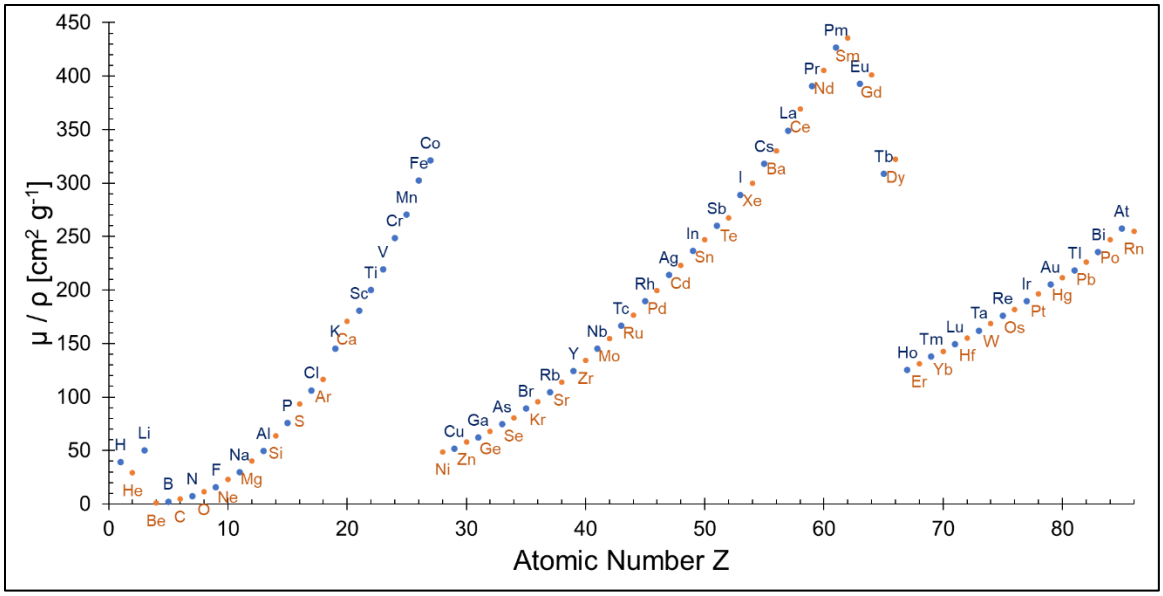

Figure 1.6. X-ray mass attenuation coefficients by element for copper K-α radiation (1.5406 Angstrom). Derived from linear interpolation of NIST data (Table 3 of Ref. [14]). Alternating colors are used to clarify the labeling, where needed.

It is critical to account for absorption in samples with supported nano-crystallites, both for identifying the “background” in the nano-crystallite containing sample and for fitting crystal structures with Rietveld refinement. For a supported nano-crystallite sample, the “background” is obtained by separately measuring the pure support. Any difference in absorption between the sample and its support will cause differences between the measured support and the actual support’s contribution to the nano-crystallite sample’s diffractogram. This is why for many samples the pure support often appears to give a more intense diffractogram than the nanoparticle containing support. For Rietveld refinement, the absorption will cause discrepancies between the calculated diffractograms and experimental data unless it is accounted for.

X-ray mass attenuation coefficients μ / ρ for elements with atomic numbers 1 through 92 can be obtained from Table 3 of Hubbel and Seltzer [14]. The data is

presented by element as a function of wavelength. For compounds and mixtures, μ / ρ values are obtained by adding together the x-ray mass attenuation coefficient of each element present in the mixture multiplied by the element's mass fraction w_i:

$$\frac{\mu}{\rho} = \sum w_i \times \left(\frac{\mu}{\rho}\right)_i \qquad \text{Eq. 2}$$

To obtain the linear mass absorption coefficient μ, the mass attenuation coefficient must be multiplied by the sample's density ρ. For powder samples, the density depends on the volume of the spaces between particles (i.e. packing density). Knowledge of both the sample mass and volume are thus required; therefore, the dimensions of the sample holder must be carefully measured along with the mass of each sample. Also note that the calculation requires knowledge of the mass fractions of each element present; this information is best obtained with a separate characterization technique, e.g. by inductively coupled plasma – optical emission spectroscopy (ICP-OES) or x-ray fluorescence (XRF). It can quickly become tedious to calculate μ for mixtures containing multiple elements; a tool is provided in the supplementary information to aid in the calculation.

According to Hermann and Ermrich [15], absorption in fine multi-phase powders can be corrected as follows:

$$\frac{I_i'}{I_0} = \frac{c_i[1 - 2(\mu_i - \bar{\mu})b_i]}{2\bar{\mu}} \qquad \text{Eq. 3}$$

In this description I_i' is the intensity reflected from phase *i*, I_0 is the incident beam intensity, c_i is the volume fraction of phase *i*, μ_i is the x-ray mass attenuation coefficient of phase *i*, $\bar{\mu}$ is the mean x-ray mass attenuation coefficient of the entire powder sample, and b_i is defined as

$$b_i = \frac{2B_i}{3} \qquad \text{Eq. 4}$$

where B_i is the mean breadth of the particles of phase *i*. In Eq. 3, the $(\mu_i - \bar{\mu})b_i$ term represents the contribution of bulk microabsorption (surface microabsorption is neglected). Microabsorption is discussed in detail later. It is difficult to correct for since corrections discussed in the literature either require knowledge of both the powder particle sizes and detailed knowledge of how the powder volume fraction varies with depth, or refine parameters related to these physical variables. For comparing a sample and its support, the best approach is to reduce the effects of microabsorption as much as possible by finely grinding the samples and by making their surfaces as smooth as possible during the XRD experiment. For very fine particles with x-ray mass attenuation values close to the sample average, the $(\mu_i - \bar{\mu})b_i$ term becomes negligible and the intensity of the reflection from phase *i* is estimated by

$$I_i' = \frac{I_0 c_i}{2\bar{\mu}} \qquad \text{Eq. 5}$$

Zevin, et al. [16] point out that if the $(\mu_i - \bar{\mu})b_i$ term in Eq. 3 is not truly negligible, then for low absorbing phases ($\mu_i < \bar{\mu}$) the adjusted intensity will be amplified, while high absorbing phases ($\mu_i > \bar{\mu}$) will be diminished. Brindley [17]

classifies powders in terms of the parameter μD, where D is the linear size of a particle (according to Hermann and Ermrich [15], usually the mean chord length $\bar{l}$ is used). In this work, we assume that the parameters D and B are equivalent. Microabsorption is directly related to the value of μD, i.e. μB. Fine particles are defined as having $\mu B < 0.01$; these samples will have negligible microabsorption. In terms of Eq. 3 and Eq. 4, the goal of sample preparation would therefore be to have $\mu_i B_i < 0.01$. For nano-crystallites, the value of B is so small that this is valid, even when μ is high (e.g. Au or Pt). For the support, μ tends to be closer to that of the bulk (since the weight loadings of nano-crystallites tend to be low). However, support particle sizes are often large; they can be reduced by grinding the sample before measurement.

To compare the intensity of the same phase between two samples 1 and 2

$$\frac{I_{i,1}{}'}{I_{i,2}{}'} = \frac{c_{i,1}\bar{\mu}_2}{c_{i,2}\bar{\mu}_1} \qquad \text{Eq. 6}$$

where $I_{i,1}'$ is the intensity of the reflection from phase i in sample 1, and $I_{i,2}'$ is the intensity of the reflection from the same phase i in sample 2. If the total volume of the two samples are identical (a reasonable assumption if both samples are carefully prepared in the same sample holder), then the comparison can be made in terms of the individual volumes V,i of each phase

$$\frac{I_{i,1}{}'}{I_{i,2}{}'} = \frac{V_{i,1}\bar{\mu}_2}{V_{i,2}\bar{\mu}_1} \qquad \text{Eq. 7}$$

If the density of phase *i* in each of the samples is assumed identical between samples 1 and 2, this becomes

$$\frac{I_{i,1}{}'}{I_{i,2}{}'} = \frac{m_{i,1}\bar{\mu}_2}{m_{i,2}\bar{\mu}_1} \qquad \text{Eq. 8}$$

where $m_{i,1}$ and $m_{i,2}$ are the masses of phase *i* present in sample 1 and 2, respectively. One of the most prominent experimental differences of this method is the requirement to measure the sample mass. Eq. 8 is a useful form, since the mass of each phase can be calculated from the measured sample mass if the weight loadings of the sample are already known. The x-ray mass absorption coefficients can be obtained per the discussion of the previous section. Note the assumptions required in the derivation of this expression. Particle sizes must be very fine ($\mu D < 0.01$), so it is good practice to finely grind samples before loading them into the sample holder, especially for samples with high μ. Total sample volumes must be equal, so the samples should be carefully prepared in the same sample holder. Phase densities must be equivalent between samples, so the pure support should follow the same treatment as the nanocrystalline sample.

Finite sample thickness

A normal Bragg-Brentano x-ray diffraction analysis assumes an “infinitely thick” sample, i.e., none of the incident x-rays pass completely through the sample. If x-rays do reach the bottom of the sample holder, there is a reduction from the expected diffraction intensity. This “finite thickness” reduction increases with increasing incident angle, since the x-rays will travel through less sample before

reaching the bottom of the holder. Figure 1.7 compares the correction that must be made for four common catalyst supports: carbon, silica, zirconia, and ceria. The correction depends exponentially on the total x-ray attenuation coefficient of the powder sample. Samples with low μ values such as carbon will need significantly more correction than samples with high μ such as ceria. Figure 1.7 also shows the effect of placing 5 wt% Pt onto the carbon support. The large difference in x-ray mass attenuation between Pt and C results in the total sample μ increasing from 2 cm^{-1} to 6 cm^{-1}. For such a system a large correction must be made to match the pure support diffractogram to that of the metal containing sample.

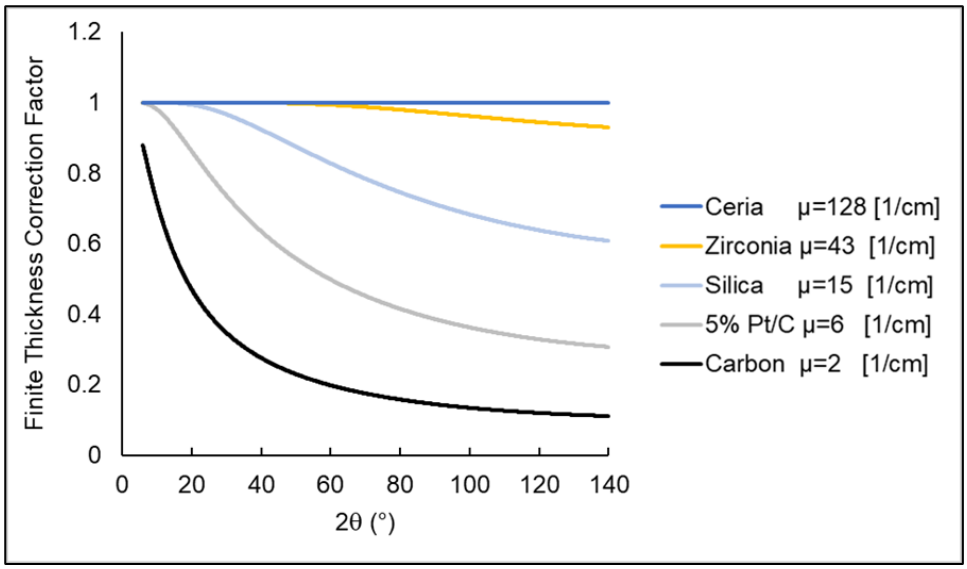

Figure 1.7. Comparing the finite thickness correction factors of different samples. Calculations assume 10mg of sample in a sample holder cavity 0.288mm deep and 10.21 mm in diameter.

For Bragg-Brentano geometry, Dinnebier, et al. [18] report the correction factor A for finite thickness as

$$A = 1 - e^{-\bar{\mu} t_s \frac{2}{sin\theta}} \qquad \text{Eq. 9}$$

where t_s is the thickness of the sample and θ is the incident angle. To compare the intensities of a common phase in two separate samples

$$\frac{I_{i,1}{}'}{I_{i,2}{}'} = \frac{A_1}{A_2} \qquad \text{Eq. 10}$$

Correcting a pure support for absorption and finite thickness

Combining Eq. 10 with Eq. 8 gives

$$\frac{I_{i,1}{}'}{I_{i,2}{}'} = \frac{m_{i,1}\bar{\mu}_2 A_1}{m_{i,2}\bar{\mu}_1 A_2} \qquad \text{Eq. 11}$$

If the nano-crystallite containing sample is designated as sample 1 and the pure support as sample 2, then the intensity of the support reflection in the nano-crystallite sample ($I_{i,1}$') can be obtained from the intensity of the pure support reflection ($I_{i,2}$') as follows

$$I_{i,1}{}' = \frac{I_{i,2}{}' m_{i,1}\bar{\mu}_2 A_1}{m_{i,2}\bar{\mu}_1 A_2} \qquad \text{Eq. 12}$$

$I_{i,2}$' is obtained by subtracting the sample holder contribution from the pure support's XRD pattern. Once $I_{i,1}$' has been estimated using Eq. 12, the sample holder contribution for the nano-crystalline sample is added to it. The final result is an accurate estimate of the "background" for the nano-crystalline sample.

Step 3: Analysis with Rietveld Refinement

Once the "background" has been obtained by adjusting the pure support to match the sample, it is imported into Topas and fit with a high-order Chebyshev

polynomial. The polynomial coefficients of the polynomial are then fixed and the sample's diffractogram is imported into Topas. Phases of interest are identified, and their structures imported into Topas. For the actual Rietveld refinement, very little is allowed to refine, since it is easy to "fit an elephant" with such broad peaks. A typical analysis will only allow the overall scale factor and crystallite size for each phase to refine (for tight size distributions purely Gaussian peaks are used for size broadening since size broadening gives a Gaussian distribution). All other parameters (emission profile, instrument profile, correction factors, etc. are measured or calculated prior to the refinement and are fixed. Once the most promising fits are identified, the metal lattice parameter (if a metallic phase is present) and two surface roughness parameters may be allowed to refine in order to account for any surface roughness that may be present in the sample. It is important to note that all intensity corrections should be made on a point-by-point basis rather than Topas' default of scaling entire peaks by the value of the intensity factor at the peak's center. See the supplementary info for detailed information on what modifications need to be made to the Topas macros in order to scale for the intensity factors point-by-point. In addition to the intensity factors already discussed, there are three remaining intensity factors that come into play only during the Rietveld refinement: beam spill, Lorentz polarization, and surface roughness. The following sections discuss these intensity factors in more detail.

Beam Spill

The calculation of a diffraction pattern from a structure assumes that the intensity of the incident x-rays striking the sample is constant. Beam spill is a

physical effect related to the x-ray beam divergence and incident angle on the sample; at low angles the beam spreads over a wide area while at high angles the beam covers a much smaller area. Beam spill (also known as overspill) occurs when the region illuminated by the x-ray beam on the plane containing the sample extends outside of the sample. Figure 1.8 compares the beam spill vs. incident angle for two separate instrument geometries using the same sample holder. Geometry (A) has much greater beam spill than geometry (B). It is tempting to think that this means geometry (B) is more desirable. However, the benefit of using a wider x-ray beam is that more x-rays strike the sample at high angles, giving a stronger signal to noise ratio (e.g., comparing the instrument geometries of Figure 1.9 at 30° reveals a greater area of the sample struck by x-rays for geometry A). This increased signal from a wider x-ray beam at high angles is desirable - if the decreased low-angle intensities caused by beam spill can be corrected for.

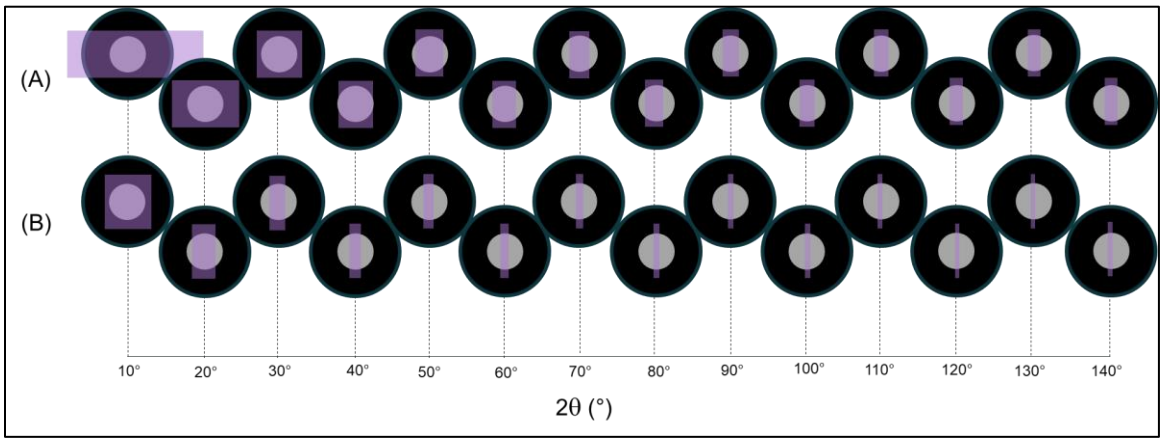

Figure 1.8. Comparing beam spill vs. incident angle for two instrument geometries: (A) Goniometer radius = 150mm, divergence slit = 1.25° (2θ); (B) Goniometer radius = 217.5mm, divergence slit = 0.3° (2θ). The purple shaded region is the total illuminated area of the beam, the sample is depicted by the inner grey circles.

By default, Topas implements a one-dimensional correction for beam spill. This assumption assumes a constant sample length (S) equivalent to the diameter of the sample. Dinnebier, et al. [18] present the correction factor (Ov) as

$$Ov = \frac{S}{L_D} \qquad \text{Eq. 13}$$

where L_D is the irradiated length of the beam in the plane of the sample, approximated by

$$L_D = \frac{R\varphi}{sin\theta} \qquad \text{Eq. 14}$$

where R is the goniometer radius, φ is the divergence slit opening in radians, and θ is the incident angle. This beam spill correction is implemented only at lower angles while L_D is larger than the sample length; at higher angles the correction factor is given a value of 1.

For diffraction patterns with sharp peaks the one-dimensional correction is a useful tool, but for diffraction patterns with nano-crystallite containing samples greater accuracy needed. A two-dimensional correction is needed, where the curvature of the sample with respect to the beam is taken into account. It is also helpful to take any sample displacement into account, since a vertical offset will change the play of the beam over the surface. We start by defining our 2-D correction factor Ov_{2D} as

$$Ov_{2D} = \frac{S_{2D}}{A_{2D}} \qquad \text{Eq. 15}$$

where S_{2D} is the irradiated sample area and A_{2D} is the total area in the plane of the sample that is irradiated by the incident x-ray beam. A_{2D} can be written as

$$A_{2D} = Axial\ beam\ width \times (s_1 + s_2) \quad \text{Eq. 16}$$

where s_1' and s_2' are the equatorial irradiated lengths on the primary and secondary sides of the sample center, respectively, as shown in Figure 1.9 (A). The axial beam width depends on the goniometer radius R and the primary Soller slit angle SS:

$$Axial\ beam\ width = 2Rtan\left(\frac{SS}{2}\right) \quad \text{Eq. 17}$$

Expressions for s_1' and s_2' in terms of the incident angle θ and height displacement h [mm] are derived trigonometrically (see the supplementary info for the derivation):

$$s_1{}' = \frac{Rsin\left({}^{\varphi}/_{2}\right)}{\sin\left(\theta + {}^{\varphi}/_{2}\right)} + \frac{h}{\tan\left(\theta + {}^{\varphi}/_{2}\right)} \quad \text{Eq. 18}$$

$$s_2{}' = \frac{Rsin\left({}^{\varphi}/_{2}\right)}{\sin\left(\theta - {}^{\varphi}/_{2}\right)} - \frac{h}{\tan\left(\theta - {}^{\varphi}/_{2}\right)} \quad \text{Eq. 19}$$

where φ is the total angular opening of the divergence slit. An expression for S_{2D} can be obtained with either trigonometric arguments or calculus (see the supplementary info for the derivation):

$$S_{2D} = d^2 sin^{-1}\left(\frac{s_{m1}}{d}\right) + s_{m1}\sqrt{d^2 - {s_{m1}}^2} + d^2 sin^{-1}\left(\frac{s_{m2}}{d}\right) + s_{m2}\sqrt{d^2 - {s_{m2}}^2}$$

Eq. 20

In this equation, d [mm] is the sample radius, s_{m1} [mm] is the minimum of s_1 and d, and s_{m2} [mm] is the minimum of s_2 and d. The reason for expressing the equation this way is so that the equation can be more easily expressed in Topas' programming language. See the supplementary information for the code used to update the beam spill approximation from a 1-D correction to a 2-D correction. Figure 1.9 (B) compares the 1D beam spill correction to the 2D beam spill correction and the 2D beam spill correction with an extensive height error. Accounting for the 2-dimensional curvature of the sample makes a large difference, especially if the sample diameter is small. Height error (sample displacement) has little effect on beam spill.

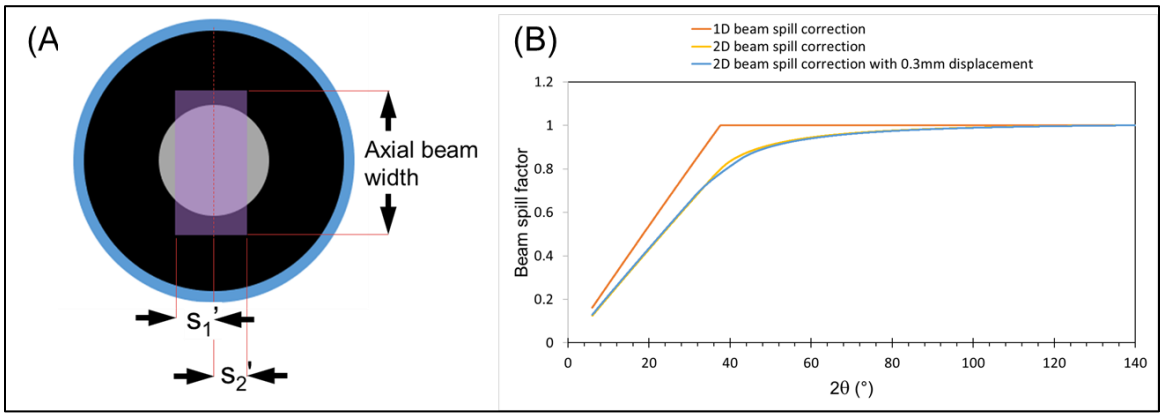

Figure 1.9. Beam spill correction. (A) X-ray beam in the plane of the sample, separated into the primary region bordered by s1 and the secondary region bordered by s2. (B) 1D and 2D correction factors for a sample diameter of 10.16 mm. Note that in this figure the 2D correction factors are normalized to their maximum value for better comparison with the linear correction.

Lorentz-Polarization

The Lorentz-polarization correction is an angle-dependent correction factor that accounts for two geometric effects (the Lorentz factor) as well as the polarization of the x-ray beam after scattering. It has been well documented, and for a detailed understanding of its physical bases this work will defer to the excellent discussions of other authors, such as Dinnebier, et al. [18] and Pecharsky and Zavalij [19]. The latter writes the correction factor for powder diffraction with no monochromator as

$$LP = \frac{1 + cos^2 2\theta}{cos\theta sin^2\theta} \qquad \text{Eq. 21}$$

Figure 1.10 (A) shows how significant the Lorentz-polarization factor is. Low angle peaks are greatly amplified with respect to the higher angle peaks. The default implementation of the correction factor in Topas scales each calculated peak by the LP value at the peak center. This may be fine for sharp peaks, but it can lead to significant errors with broad peaks. Figure 1.10 (B) shows the difference between a peak scaled only by its center value (orange) vs. a peak scaled point by point. The result of scaling point by point is an apparent peak shift to the left (an effect known as “peak pulling”). The extent of this shift depends on how much the LP factor changes between the left and right peak edges and can be over 1° 2θ. The apparent shift will be greater for peaks at low angles and less for peaks at high angles (up to around 100° 2 theta, where the LP correction reaches a minimum and begins to increase again – the corresponding peak pulling at angles > 100° 2 theta is to the right). The peak pulling effect of Lorentz-

Polarization explains why broad experimental peaks appear shifted to the left – a fact which if not accounted for properly can lead to false analyses claiming increased lattice constants. A similar apparent peak shift due to broad peaks being multiplied by an angle-dependent intensity factor is discussed in Gallezot, et al. [8], where the intensity factor is the angle-dependent atomic form factor (see *Limitations of the method*).

It is important to note that any angle-dependent intensity factor must also be accounted for on a point-by point basis. For example, scaling a peak for beam spill will shift peaks to the right (see Figure 1.9 B) while peaks scaled for finite thickness (Figure 1.7) will shift peaks to the left. See the supplementary info for a discussion on the code changes needed in Topas in order to implement the point-by-point scaling of intensities.

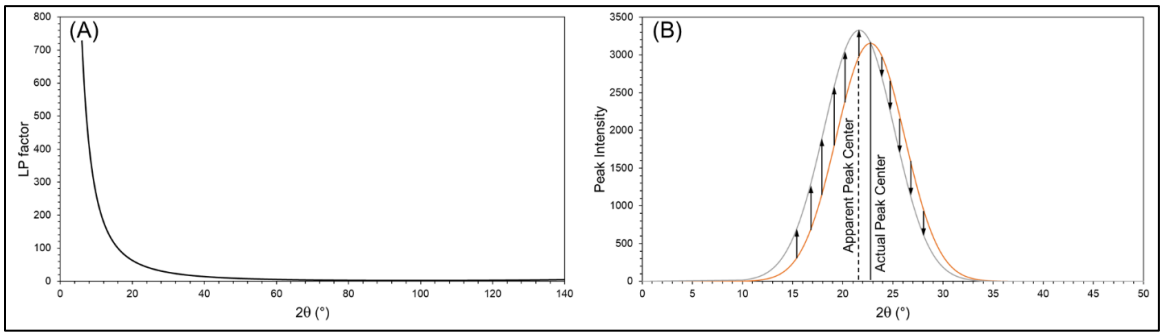

Figure 1.10. Lorentz polarization and peak pulling. (A) Lorentz polarization correction factor for unpolarized (no monochromator) radiation. (B) Scaling point-by-point (black) vs. scaling by peak center (orange) with Lorentz-Polarization: apparent peak shift for broad peaks (peak pulling). The featured peak corresponds to a crystallite size of 1.1nm

Microabsorption and Surface Roughness

Surface roughness – as the name suggests – comes from a sample surface that is not perfectly smooth. Figure 1.11 shows how the volume fraction of powder

samples increase from zero at the surface to the bulk volume fraction at a certain depth. A surface is smooth if the transition is sudden (as a function of depth). For a rough surface, the transition is more gradual. The observed effect of surface roughness is a decrease in intensity at low angles. The effect can be quite significant: Pitschke, et al. [20] demonstrate experimentally that a sample with a rough surface can have low-angle intensities less than a third of those from the same sample after smoothing the surface with a flat plate. Surface roughness is a component of microabsorption: the higher the amount of microabsorption, the greater the significance of a rough surface. It is helpful here to clearly differentiate between absorption and microabsorption. Absorption describes the attenuation of x-rays as they pass through a homogeneous sample and is represented by the left-hand term of Eq. 22 ($I = I_0/2\mu$), while microabsorption *P* is an additional term that accounts for heterogeneity in the sample (i.e., large grain sizes and/or differences in μ between individual phases and the bulk).

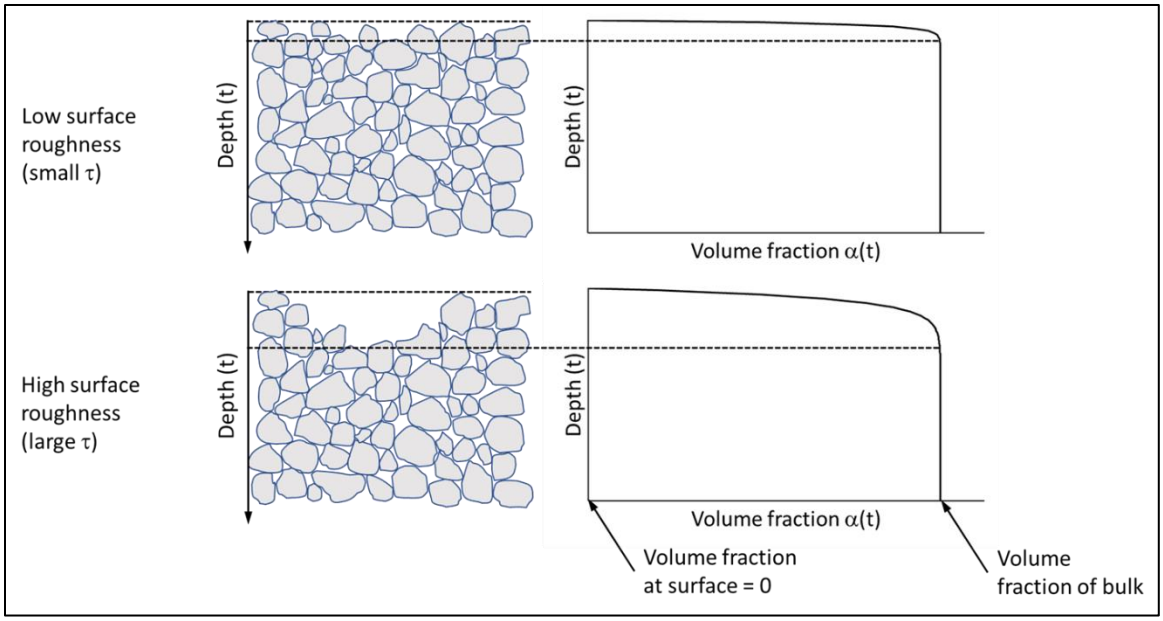

Figure 1.11. Surface roughness illustration, showing how the volume fraction of the sample changes with depth for a smooth vs. rough surface. The volume fraction vs. depth curves are described by the relation of Hermann and Ermrich [21], as stated in Pitschke, et al. [20]

Building upon the work of Harrison and Paskin [22] and Suortti [23], Hermann and Ermrich [21] present the reflected intensity (I) from a single phase sample with microabsorption *P* as

$$I' = I_0 \frac{1 - P}{2\mu} \qquad \text{Eq. 22}$$

where *P* is written as the sum of an angle independent bulk term P_0 and an angle dependent surface term P_s. P_0 and P_s are expressed as

$$P_0 = 2\mu\beta(1 - \alpha_0) \qquad \text{Eq. 23}$$

$$P_s = 2\mu\beta\alpha_0 \left(\frac{\tau}{sin\theta}\right)\left(1 - \frac{\tau}{sin\theta}\right) \qquad \text{Eq. 24}$$

where α_0 is the volume fraction of the bulk sample and β is related to the mean chord length $\bar{l}$ of the particles by

$$\bar{l} = \frac{-\beta}{ln\alpha_0} \qquad \text{Eq. 25}$$

The surface roughness parameter τ is defined as

$$\tau = \frac{t_0}{\beta} \qquad \text{Eq. 26}$$

where t_0 is defined by the expression for volume fraction α as a function of depth *t* into the sample

$$\alpha(t) = \alpha_0\left[1 - e^{-t/t_0}\right], t < 0 \qquad \text{Eq. 27}$$

As is shown in Figure 1.11, as t_0 increases, the change in volume fraction with depth becomes more gradual, corresponding to a rough surface. Pitschke, et al. [20] have rewritten the $1 - P$ microabsorption term of Eq. 22 in terms of Eq. 23 through Eq. 27. It is presented as an angle dependent correction factor S_r

$$S_r = 1 - P_0 - \frac{C\tau}{\sin\theta}\left(1 - \frac{\tau}{sin\theta}\right) \qquad \text{Eq. 28}$$

where S_r is the correction factor, and C is the collection of physical terms $2\mu\beta\alpha_0$. Pitschke, et al. [24] note that if the extent of microabsorption is small ($\mu\bar{l}$ <<1) and the surface is not too rough than P_0 and C are described exactly by their physical parameters.

TOPAS implements the correction factor shown in Eq. 28 as a normalized form with only two refineable parameters. The normalization is achieved by dividing the correction factor by its maximum value (which occurs when sinθ is equal to 1; i.e., θ is equal to 90°):

$$S_{Norm} = \frac{1 - P_0 - \frac{C\tau}{\sin\theta}\left(1 - \frac{\tau}{sin\theta}\right)}{1 - P_0 - C\tau(1-\tau)} \qquad \text{Eq. 29}$$

From here both numerator and denominator can be divided by $1 - P_0$ and terms collected to give the following form:

$$S_{Norm} = \frac{1 - \frac{C\tau}{1-P_0}\left(\frac{1}{sin\theta} - \frac{\tau}{sin^2\theta}\right)}{1 - \frac{C\tau}{1-P_0}(1-\tau)} \qquad \text{Eq. 30}$$

Topas implements this form with the refineable parameters A_1 and A_2, where

$$A_1 = \frac{C\tau}{1-P_0};\ \ A_2 = \tau \qquad \text{Eq. 31}$$

The final form of the correction factor in Topas is as follows:

$$S_{Norm} = \frac{1 - A_1\left(\frac{1}{sin\theta} - \frac{A_2}{sin^2\theta}\right)}{1 - A_1 + A_1A_2} \qquad \text{Eq. 32}$$

It is useful to have an idea of what maximum and minimum values are for the refined parameters A_1 and A_2 in Topas, which lose physical significance as microabsorption and surface roughness become too large. Topas' default maximum and minimum for both A_1 and A_2 are 0.0001 and 1. These minimum

values are reasonable, but the maximum values are not. Not only does allowing the surface roughness parameters access to the entire default solution space significantly increase computation time, but also fits with unreasonable parameters can be achieved. Figure 1.12 shows a proposed set of conditions for a sample fit between 20° and 100° 2θ. Note that as the diffraction angle decreases, the expression decreases to a minimum value and then increases again. As a first limitation for a physical sample, it is not reasonable for this minimum to occur in or near the region where the sample is fit. The location of this minimum value is entirely dependent upon the A_2 parameter and can be identified by taking the derivative of the correction factor with respect to θ and setting it equal to 0:

$$\frac{d}{d\theta}S_{Norm} = \frac{d}{d\theta}\left(\frac{1 - A_1\left(\frac{1}{sin\theta} - \frac{A_2}{sin^2\theta}\right)}{1 - A_1 + A_1A_2}\right) = \frac{d}{d\theta}\left(\frac{1}{sin\theta} - \frac{A_2}{sin^2\theta}\right)$$

$$= -csc\theta cot\theta - A_2(-2csc^2\theta cot\theta)$$

$$0 = -csc\theta cot\theta - A_2(-2csc^2\theta cot\theta)$$

Some manipulation leads to the expression

$$A_2 = \frac{sin\theta}{2} \qquad \text{Eq. 33}$$

With this expression, the value of A_2 that will give the minimum at a desired angle θ is easily obtained. For a fit starting at 20° 2θ, it seems reasonable to place the minimum at 10° 2θ, or θ = 5°. The corresponding A_2 value is 0.044. A potentially more accurate limitation of the value of A_2 could be obtained by identifying the inflection points of the correction factor by taking the second derivative of the

expression and setting it equal to 0. The resulting expression could be used to ensure that the inflection point on the high-angle side of the minimum stays outside the fit region.

A limitation can be placed on the maximum value of A_1 by assuming that the correction factor cannot be negative. The value for which this occurs can be found by setting the correction factor equal to zero and solving for A_1 (using the value of A_2 found above). The result for this example gives $A_1 = 0.17$.

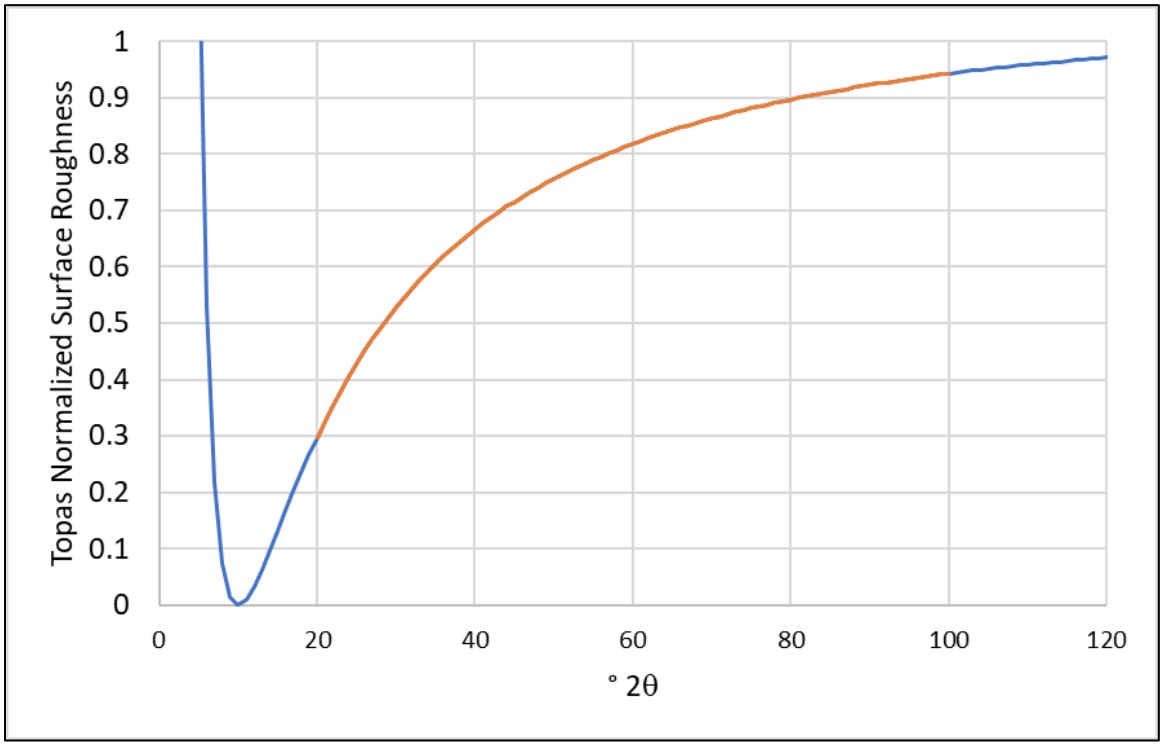

Figure 1.12. [20,] Pitschke, et al. [24] correction as implemented in TOPAS with A_1 = .1743 and A_2 = .043578

Modifying the standard XRD experiment

In light of the intensity effects discussed above and the requirements for their correction, we now compile the modifications needed for a benchtop XRD experiment designed to characterize ultra-small, supported nano-crystals.

1. All diffractograms need to be normalized to an external standard. This can be achieved by running the standard immediately before and after each diffractogram is measured.
2. Diffractograms will need to be measured for the empty sample holder, pure support, and a highly crystalline material with high $\bar{\mu}$. An additional diffractogram of a highly crystalline material with $\bar{\mu}$ equivalent to the nano-crystal sample may also be needed.
3. The mass of all samples must be recorded. Because some mass can be lost during sample preparation, recording the mass after the measurement is recommended. Ideally, the mass of the support phase should be equal between samples; measuring target masses into the sample holders can help achieve this.
4. All samples should be measured in the same sample holder.
5. The dimensions of the sample holder should be carefully measured and recorded.
6. Care should be taken to make sure that the surface of nanoparticle samples is flat and smooth. Samples should be ground prior to loading the sample holder. See the videos in the supplementary information for detailed instructions on preparing samples for the XRD.

Case Study: 4.8% Pt / amorphous silica

A 4.8 wt% Pt / amorphous silica sample prepared with the strong electrostatic adsorption method (Schreier and Regalbuto [25], Miller, et al. [26]) and aged under ambient conditions is presented as a case study demonstrating the

capabilities of benchtop x-ray diffraction when the methods presented in this work are applied. Full details of the experimental methods are provided in the supplemental information. The results are corroborated with STEM and XAS.

STEM

Figure 1.13 shows a representative STEM image and accompanying size distribution of the 4.8% Pt / A300 sample. Over 1700 particles were measured to produce the size histogram displayed in the inset. The results show a tight size distribution with no observed particles greater than 2.7nm. The resulting number-weighted average (D_N), surface-weighted average (D_S), and volume weighted average (D_V) are 1.1 nm, 1.2 nm, and 1.3 nm respectively. The volume weighted average corresponds to the XRD particle size (which is a volume-weighted technique). It is noted that because not all of the Pt nanoparticles are fully in focus in the images, these presented particle sizes (based on the projected area in the images) are an upper estimate of the particle size. The actual sizes of the measured particles in the electron beam are likely somewhat smaller (Xia, et al. [27]).

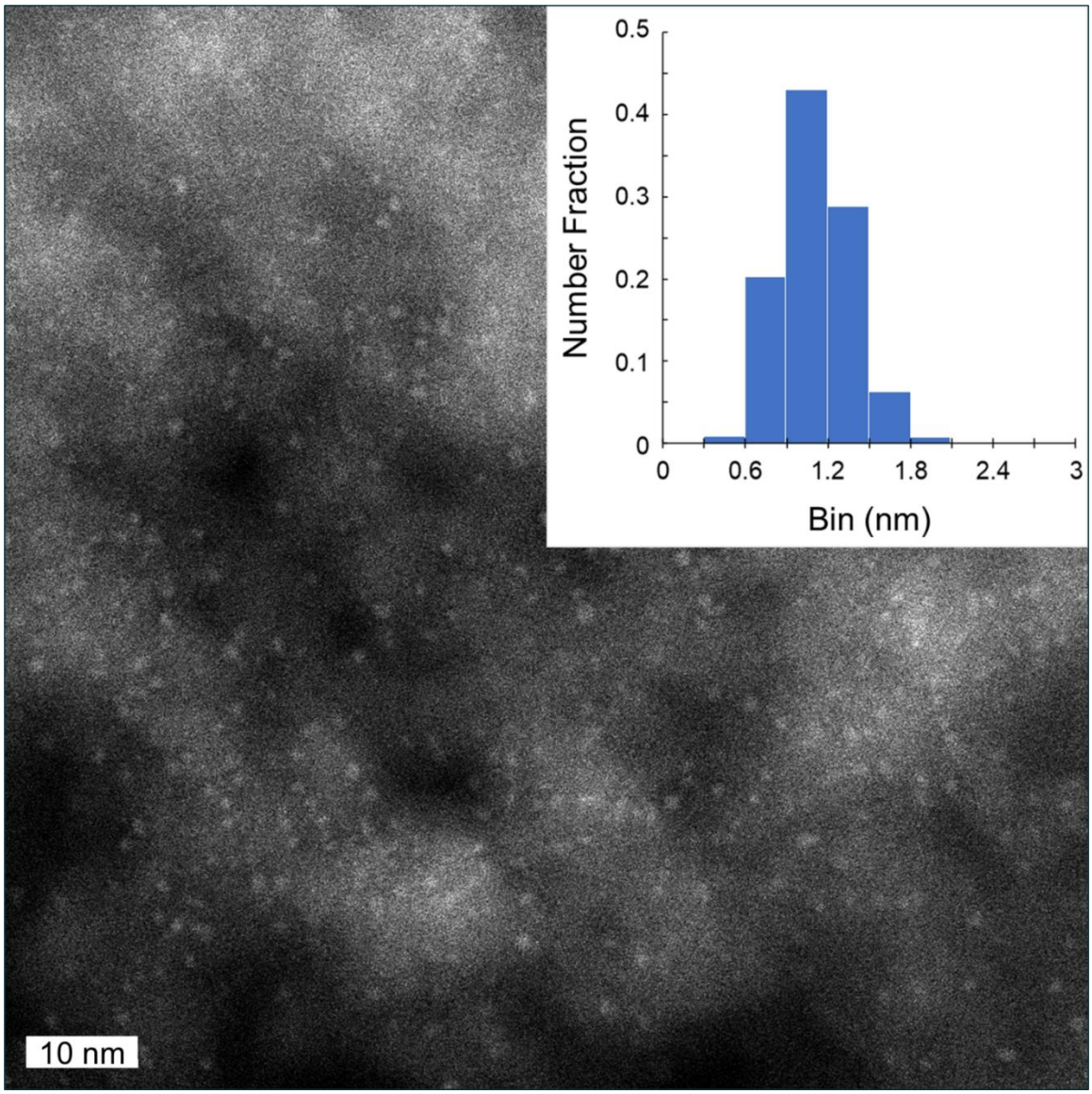

Figure 1.13. A representative STEM image of the 4.8% Pt / A300 sample. Over 1700 particles were measured to produce the included size distribution.

XRD

A detailed description of the experimental methods used for XRD is provided in the supplemental information. A brief description now follows. Figure 1.14 depicts the major steps in obtaining the sample and support diffractograms. First, the 4.8% Pt / silica sample, pure silica (treated with the same SEA, drying, and reduction treatment as the Pt sample), and empty sample holder were each

scanned six times against the NIST 1976c intensity standard. The results were corrected for intensity drift and averaged together. A spline was fit to the empty sample holder contribution using Fityk (Wojdyr [28]). Higher angles of the spline fit were estimated since the sample holder contribution from the empty sample holder does not fully describe the contribution when the sample holder cavity is filled with sample (A). Once the spline was subtracted from the Pt / silica sample and pure treated support (B) the support diffractogram was adjusted to match the absorption and finite thickness calculated for the Pt / silica sample (C). Finally, the estimated spline was added back to the adjusted diffractograms (D) for the analysis in Topas. Note that the Pt / silica diffractogram is unchanged by this process; only the support diffractogram is adjusted.

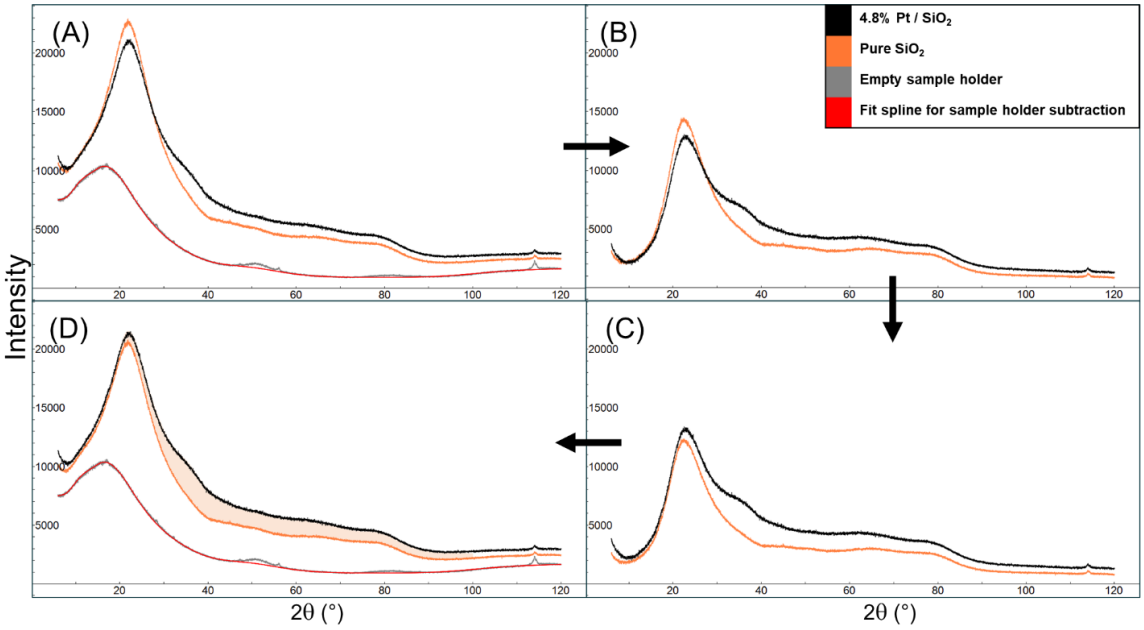

Figure 1.14. Background subtraction procedure for 4.8% Pt / SiO_2. (A) Data after adjusting for drift and averaging multiple runs. (B) Data after subtracting the estimated sample holder contribution (fit spline, shown in red). (C) Data after correcting for differences in absorption and finite thickness. (D) Data after adding back the estimated sample holder contribution (for analysis in Topas). The region

of the total calculated fit is shaded; see Figure 1.15 for the support subtracted Rietveld fit.

For the analysis in Topas, the macros for Lorentz-polarization, absorption, surface roughness, and beam spill were adjusted to scale peaks on a point-by-point basis (the Lorentz-polarization macro also had an error that was corrected; see the supplementary info for more information and for a complete list of modifications made to the Topas macros). The beam spill macro was also updated to include the 2D correction for circular sample holders. The updates to the code were made directly in the topas.inc file; this was found to be the most functional method of implementation. For the Rietveld analysis, the “background” was fixed by fitting the pure, corrected support with a high-order Chebyshev polynomial. The Pt diffractogram was then imported and twelve Pt and Pt oxide structure files (Table 1.2) were fit with only the overall scale factor and Gaussian size broadening allowed to refine for each phase. Once the most promising combinations of phases were identified, additional parameters (i.e. the Pt metal lattice parameter and two surface roughness terms) were allowed to refine.

Table 1.2. Pt / Pt oxide phases investigated with XRD

Phase	**Space Group**	**ICSD #**
Pt	225	52250
PtO	131	26599
PtO	225	105543
PtO_2	58	202407
PtO_2	136	647316
PtO_2	164	24922
PtO_2	186	24923
PtO_2	205	251568
PtO_2	224	77654
Pt_3O_4	223	30444

Pt_3O_4	229	27836
$Pt_{3.4}O_4$	223	200053

The best fit achieved with a combination of two phases is shown in Figure 1.15. The result suggests that the nano-crystallites consist of a combination of Pt and PtO_2, both with sub-nanometer crystallite sizes.

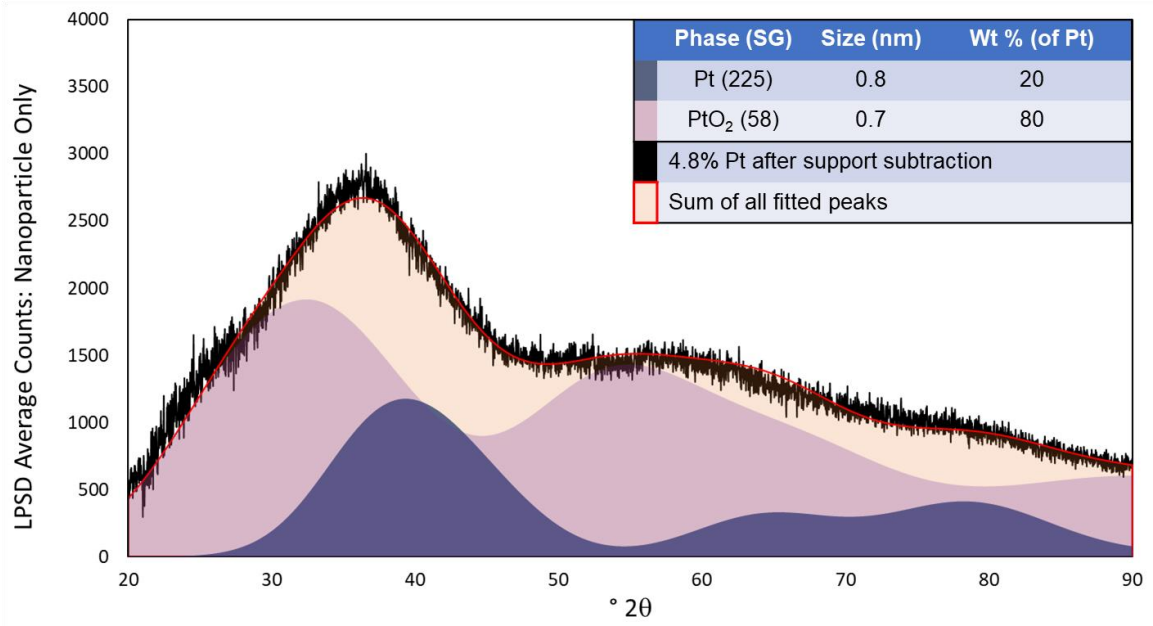

Figure 1.15. Aged 4.8% Pt sample in air, after background subtraction. In the shown fit, only seven terms were allowed to refine: the Gaussian size broadening and overall scale factor for each phase, the Pt metal lattice parameter, and two terms adjusting the intensity for surface roughness. All other terms were fixed, as described in the experimental methods in the supplementary information.

Surface oxide phase

There have been previous reports of small Pt nanoparticles oxidizing in air at room temperature, though the reports do not agree on the identity of the oxide. Bucher, et al. [29] used ^{195}Pt NMR on a 5.7% Pt / SiO_2 sample (consisting of slightly larger particles than our sample: D_S = 1.7 nm) to identify the oxide as PtO_2 (phase not specified). Gnutzmann and Vogel [10] used a Guinier XRD on a 6.3% Pt / SiO_2

sample (D_N = 1.3 nm, D_V = 1.6 nm) and identified the oxide as primarily PtO with <10% Pt_3O_4. Banerjee, et al. [30] used STEM, XPS, and a benchtop XRD with LPSD detector to investigate many Pt samples supported on carbon and silica supports. They tentatively attributed the oxide phase to Pt_3O_4, even though the phase's second strongest line at 22.5° 2θ was missing from the diffractograms. We also note that their STEM and XPS experiments took place in ultra-high vacuum – this is known to be a reducing environment and may have partially reduced the samples as compared to ambient conditions.

In this work, the background-subtracted 4.8% Pt / SiO_2 XRD (Figure 1.15) is fit well with two phases: a metallic Pt phase and ß-PtO_2 (orthorhombic, space group 58). This is in agreement with the extended x-ray absorption fine structure (EXAFS); it is noted that the EXAFS analysis also identified α-PtO_2 (trigonal, space group 164) as a possible fit. However, α-PtO_2 did not provide as good a fit for the XRD (Figure 1.30), giving unreasonable results for the metallic Pt particle size (0.3 nm) and wt% (~60%). While the identification of PtO_2 agrees with the results from Bucher, et al. [29], it does not seem to agree with the findings of Gnutzmann and Vogel [10] and Banerjee, et al. [30]. We now point out that the quality of the background subtraction can have a significant effect on phase identification. Gnutzmann and Vogel [10] adjust for differences in absorption between their sample and support, but close inspection of their results (figure 4 in [10]) reveals that the absorption correction was only applied to match the silica peaks at ~20° 2θ, rather than account for the full difference in absorption. Their resulting background subtraction falsely indicates that there is no diffraction signal on top of the silica peak, leading the

authors to choose PtO as the best fit to their patterns. Banerjee, et al. [30] did not account for absorption and other angle-dependent intensity factors, using instead a simple normalization to similarly match the silica peaks. The resulting background subtractions leave artifacts in the diffraction pattern; making it necessary to deconvolute the pattern on a peak-by-peak basis.

Lattice Parameter

A second factor affecting the oxide phase identification is whether the Pt lattice parameter is allowed to refine. Gnutzmann and Vogel [10], Banerjee, et al. [30], and this work all observe that the main Pt / SiO_2 nanoparticle sample diffraction peak is apparently centered between 36° and 38.5° 2θ, more than a full degree below the main (and lowest angle) peak of bulk Pt (39.8° 2θ). Neither Gnutzmann and Vogel [10] nor Banerjee, et al. [30] allowed the Pt lattice parameter to refine to fit this peak. Rather, Banerjee, et al. [30] attribute it to a Pt peak convoluted with a Pt_3O_4 (210) peak (space group 223) centered at 35.9°, while Gnutzmann and Vogel [10] fit the whole pattern to a majority of Pt and PtO, with minor amounts of Pt_3O_4. If we do not allow the Pt lattice parameter to refine, we similarly can achieve a good fit using small amounts of Pt_3O_4 (Figure 1.29) with Pt and PtO_2 (space group 136, which when size-broadened gives a nearly identical diffractogram to that of ß-PtO_2). However, the size of the apparent Pt_3O_4 crystallites (1.5nm) does not make sense in relation to their <10% contribution to the background subtracted Pt diffractogram. Perhaps the most unexpected result of this work is that an excellent fit of the entire pattern can be achieved with only Pt and ß-PtO2 by allowing the Pt lattice parameter to refine to larger values (corresponding to longer Pt-Pt bond

distance, i.e. a dilated Pt lattice). The resulting LP is 4.045 Å [d (111) = 2.335 Å, 38.52° 2θ], a 3.1% increase over the bulk value (3.9237 Å). In this case the peak centered around 36° is composed primarily of the Pt (111) peak and the ß-PtO_2 (011) peak (d = 2.580 Å, 34.74° 2θ). We postulate that the documentation of Pt_3O_4 by Banerjee, et al. [30] using fast Fourier transform (FFT) of atomically resolved STEM images may similarly result from an expanded metallic Pt lattice combined with the presence of PtO_2 – though the reducing environment of the UHV and electron beam may also play a role.

This lattice expansion (i.e. dilation) at first seems to contradict the general observation in literature that as nanoparticles decrease in size their lattice parameters contract (e.g. Miller, et al. [2], Lamber, et al. [31]). A closer look at the literature shows that there are several counter-examples documenting dilation instead. For example, Goyhenex, et al. [32] examined Pd nanoparticles epitaxially grown on an MgO (100) surface with surface electron energy-loss fine-structure spectroscopy under UHV conditions and observed lattice dilation with increasing particle size; the effect was attributed to polymorphism (i.e. epitaxy). Jacobs and Schryvers [33] examined Pd nanoparticles photodeposited onto a thin film of anatase TiO_2 with high resolution electron microscopy and observed lattice dilation up to 10% greater than bulk in the smaller nanoparticles; after heating in oxygen the maximum lattice dilation observed was up to 15% greater than the bulk. The authors attributed the lattice expansion to oxygen dissolved into the Pd lattice. Du, et al. [34] examined 2.5 to 5.0 nm Pt nanoparticles, both supported on carbon and unsupported with high-resolution transmission electron microscopy. The authors

documented Pt-Pt bond distance as a function of position inside a nanoparticle, and found that a surface oxide layer caused extensive lattice expansion near the surface of the nanoparticle which in turn caused the core lattice to expand beyond bulk values. Finally, Gallagher, et al. [3] examined Pt nanoparticles supported on alumina in-situ using synchrotron techniques including x-ray absorption spectroscopy (XAS), pair distribution function (PDF), and x-ray diffraction (XRD). They observed lattice contraction as a function of decreasing particle size for the fully reduced particles, but observed lattice expansion when the largest nanoparticles were measured in air with XRD (they were unable to examine the smaller nanoparticles in air with XRD due to difficulty in subtracting the background and in deconvoluting oxide phases from the metallic Pt). We summarize the literature in the following statement: as nanoparticle sizes become small their lattice parameters become more susceptible to influences that drive them away from bulk values. The smaller the nanoparticle, the less its lattice parameter/s can be assumed to match the values documented for its bulk counterpart. Whether the lattice parameter contracts or dilates or even changes phase depends on the outside influences on the particle. Because nanoparticle lattice parameters are so susceptible to change depending on the environment, it is important to be able to characterize these systems in-situ. It is challenging for instruments that require ultra-high vacuums such as electron microscopy and XPS to examine samples under ambient conditions; for systems where oxidation is suspected this is especially problematic since ultra-high vacuum is known to be a reducing environment. XRD does not share this limitation and can be used to directly

characterize samples under a multitude of environments – the simplest of which is ambient conditions.

An apparent contradiction that we note is that our EXAFS analysis indicates a small lattice parameter contraction (3.66 Å, -6.7%, see below) compared to the bulk (3.92 Å), rather than the expansion observed with XRD (4.05 Å, +3.3%). One possible explanation is that for XRD the “as received” sample was measured in air, while the EXAFS sample was measured after stabilizing in a flow of He, during which there is a slight change in the white line intensity. Interestingly, comparisons with the results of Gallagher, et al. [3] indicate a similar discrepancy between EXAFS and XRD for oxidized Pt: lattice expansion with XRD and lattice contraction with EXAFS – but in their case both methods measured the oxidized sample in air.

Size and extent of surface oxidation

The XRD fit with Pt and ß-PtO_2 (Figure 1.15) suggests roughly 20% Pt crystallites around 0.8 nm in size and 80% ß-PtO_2 crystallites around 0.7 nm in size. It is noted that the estimated size of each phase depends on the structure and parameters included in the fit; variations as much as 0.2nm were observed. It is interesting that the sum of these two dimensions approximates the STEM volume-weighted size of 1.3 nm (as also noted by Banerjee, et al. [30]) and the EXAFS-determined value of the fully reduced sample with an average particle size of ~1.3nm. In the following discussion we compare the combined Pt / Pt oxide structures in terms of the number of Pt atoms. We can estimate an upper limit for the number of atoms present in the average nanoparticle by assuming that in the STEM environment the nanoparticles are fully reduced (PtO_2 has approximately

half the amount of Pt atoms per unit volume). With this assumption, and making use of the Pt and ß-PtO_2 unit cell volumes and number of Pt atoms per unit cell (Pt: unit cell = 60.407 $Å^3$, 4 Pt atoms per cell; ß-PtO_2: unit cell = 63.818 $Å^3$, 2 Pt atoms per cell) the STEM result of 1.3 nm particles gives 76 atoms for a spherical particle (38 atoms for a hemisphere). If we assume a Pt core - Pt oxide shell model with the XRD dimension of 0.84 nm as the diameter of the core (0.84 nm, 21 atoms for a sphere), then 76 total Pt atoms is consistent with an oxide shell containing 55 atoms and around 0.4 nm thick. This is smaller than the XRD ß-PtO_2 size of 0.7 nm (0.66 nm); however, it is noted that the thickness of a shell presents the shortest possible distance that X-rays can travel through a spherical shell; the longest possible distance is along the chord tangent to the core (Figure 1.16). In this model the maximum distance would be 1.4 nm. The average distance x-rays travel through a shell material would therefore be somewhere in-between; this is consistent with our result. The mass percent of each phase can also be calculated from the core-shell model: a 21 Pt atom core and 55 Pt atom shell (with 110 corresponding oxygen atoms) results in 24 wt% Pt and 76 wt% PtO_2. This is consistent with the XRD and x-ray absorption near edge structure (XANES) results.

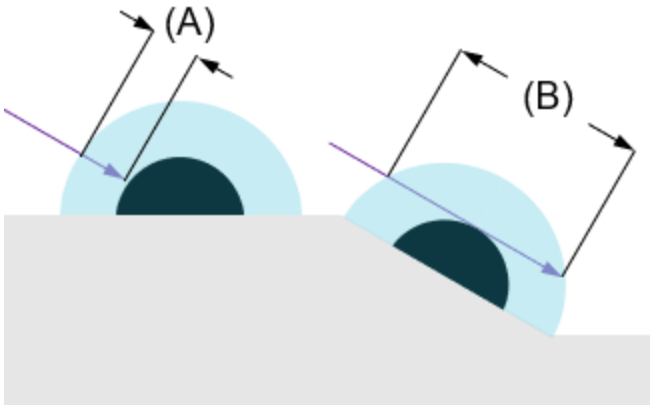

Figure 1.16. The distance an x-ray travels through a material in a shell depends on where it strikes. (A): minimum distance traveled. (B): maximum distance traveled.

XAS

An in-situ XAS (EXAFS, and XANES) experiment was conducted on the 4.8% Pt / SiO_2 sample to corroborate the XRD findings. Details on the experimental methods can be found in the supplemental information. The results are now discussed.

Pt L_3-edge XANES

To estimate the formal oxidation state of the Pt in the catalyst, the normalized Pt L_3-XANES spectra of the catalyst at three different steady state conditions were compared with those from metallic Pt and Pt(IV)standards, Figure 2.5. It is observed that in the as-prepared state the average oxidation state is slightly lower than the Pt^{4+} state of the bulk PtO_2 reference. Linear combination fitting, using bulk standards, suggests the as-prepared state consists of ~34% Pt metal and ~66% PtO_2. During the heat treatment in He there is a decrease in the white line intensity relative to the as prepared state. We postulate that the decrease in the white line intensity in this state is primarily due to the removal of adsorbed

species from the surface of as-prepared catalysts. In the reduced state the absorption edge resembles that of metallic Pt, suggesting a completely metallic state after reduction.

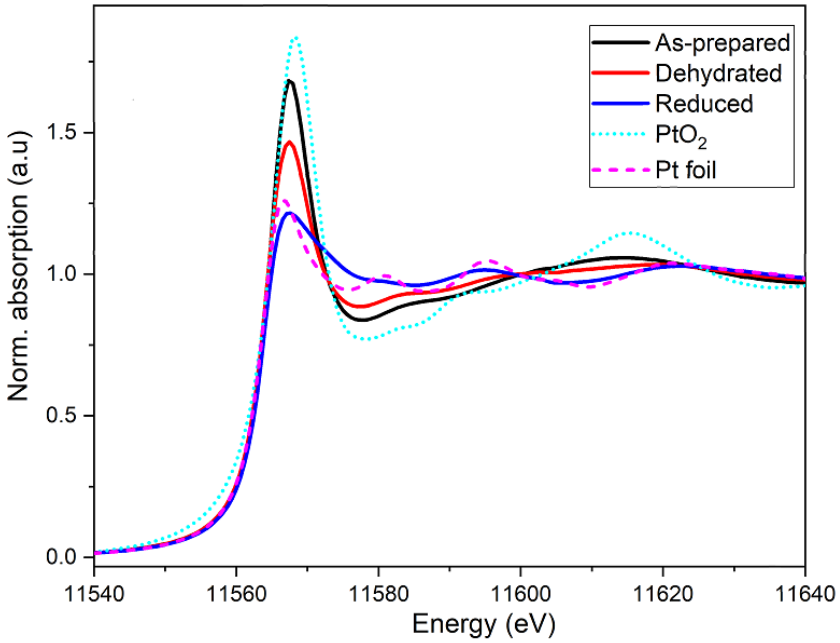

Figure 1.17. Normalized XANES spectra of the catalyst at three steady state conditions at room temperature compared with Pt foil and PtO_2 standards.

Pt L_3-edge EXAFS

The results of the as prepared and reduced catalysts are discussed here; the desorbed catalyst is shown in the SI. The experimental k^2 weighted $\chi(k)$ data and FT [k^2 weighted $\chi(k)$] or $\chi(R)$ data fitted with the described model of the as prepared and reduced catalysts are shown in Figure 1.18.

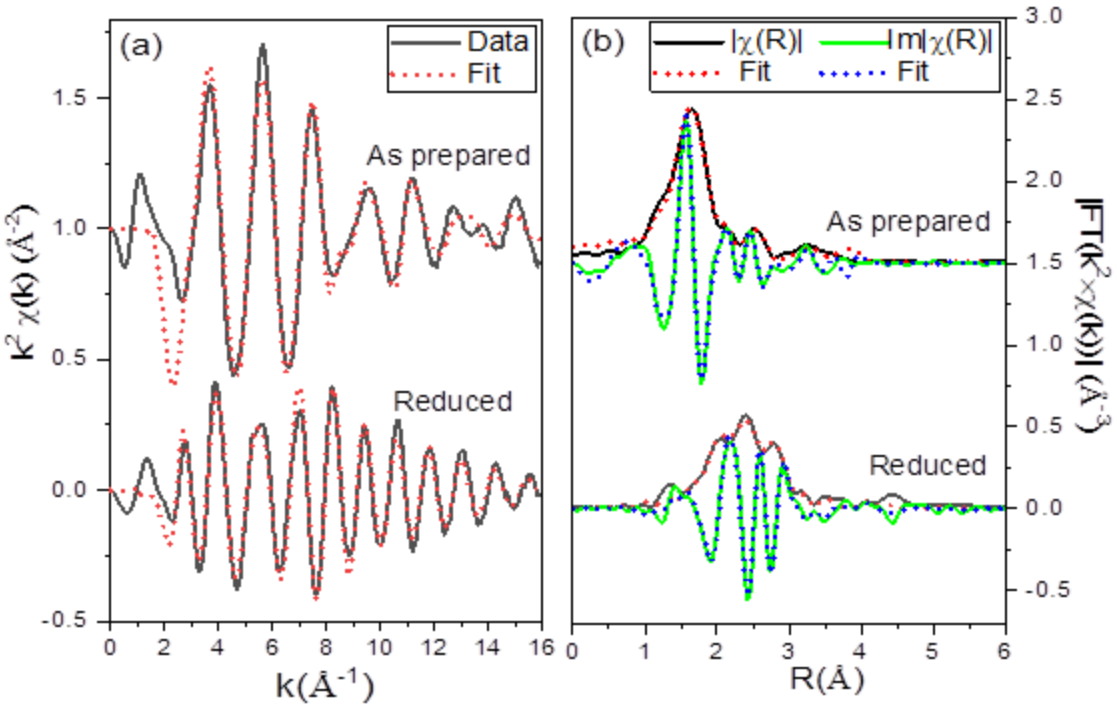

Figure 1.18. Experimental data fitted with theoretically generated (a) k^2 weighted χ(k) spectra and (b) Fourier transformed (k^2 weighted χ(k)) spectra of the as prepared and reduced catalyst. Fitted window range for the as prepared state is Δk = 3.0 – 12.4 $Å^{-1}$; ΔR = 1.0 – 3.8 Å and for the reduced state is Δk = 3.0 – 13.4 $Å^{-1}$, ΔR = 1.5 – 4.0 $Å^{-1}$.

The VESTA (Momma and Izumi [35]) generated structural representation of the orthorhombic PtO_2 structure is shown in the supplementary information (Figure 1.24). The corresponding available scattering paths are shown in Figure 1.25. The EXAFS best fitted results are summarized in Table 1.3. The scattering paths used for the fitting are shown in Figure 1.19. The obtained coordination numbers (C.N.) are plotted against their bond lengths in histogram stick plots displayed in Figure 1.20.

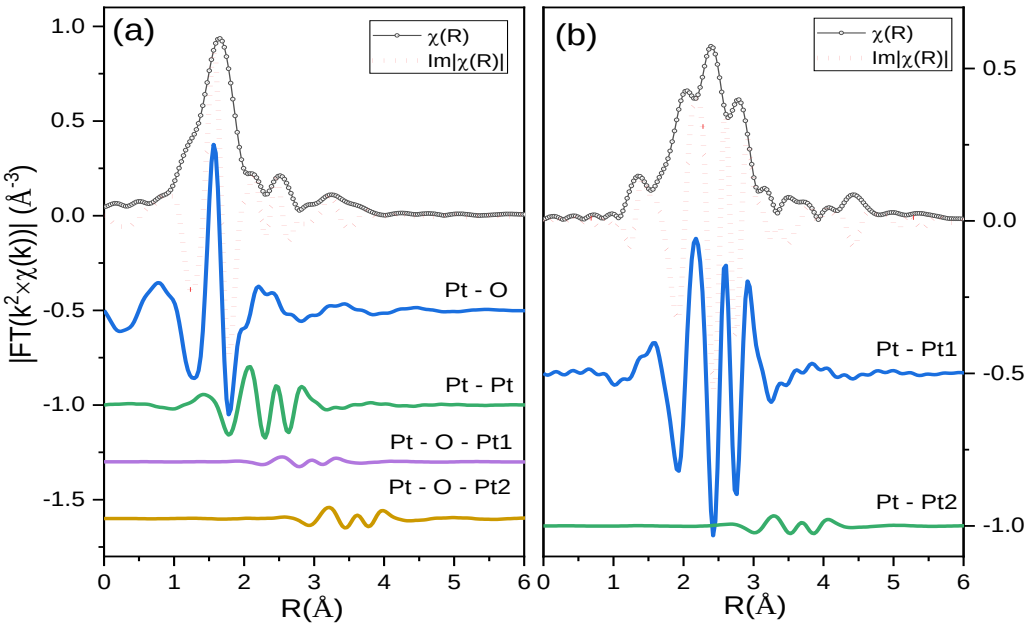

Figure 1.19. Imaginary part of the scattering paths used for fitting compared with the experimental χ(R) and Im|χ(R)| data for (a) as prepared, (b) reduced state of the catalyst.

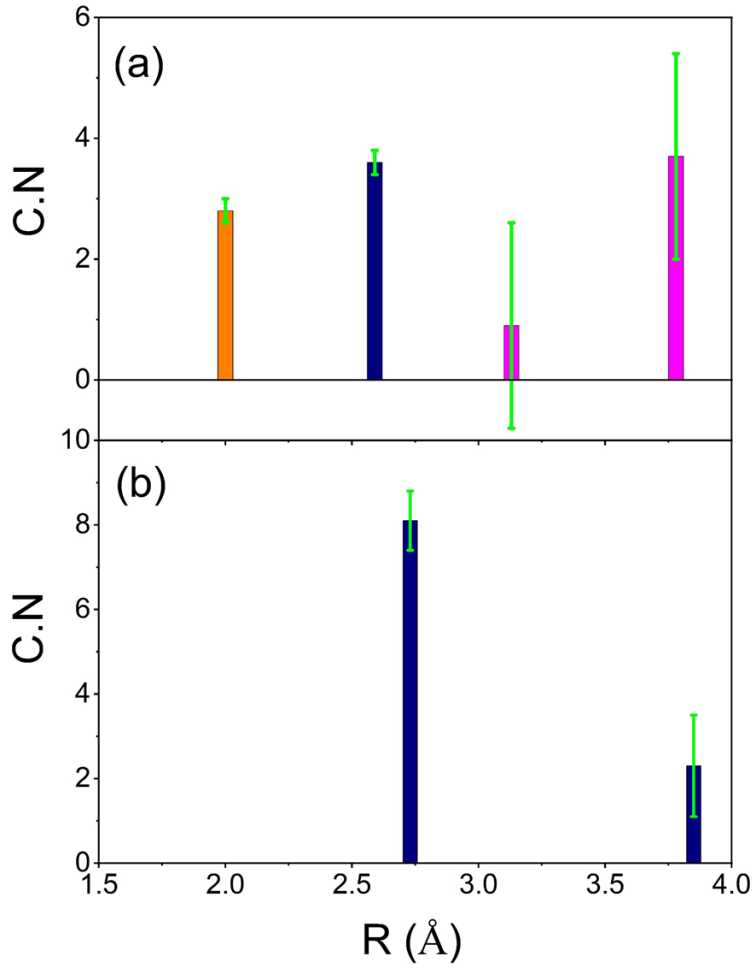

Figure 1.20. Histogram stick plots (C.N. vs R) of (a) as prepared state, (b) reduced state of the Pt/SiO_2 catalyst. The orange stick represents the Pt – O path, pink represents the Pt – Pt (oxide) scattering paths obtained from the ß-PtO2 structure, and dark blue represents the Pt – Pt metallic scattering path obtained from Pt metal. Green lines indicate the error bars.

The χ(R) vs R spectra of the as prepared catalyst (Figure 1.19 (a)) consists of three main peaks up to 3.8 Å where the 1st Pt – O path contributes to the first intense peak within 1.0 – 2.2 Å and the metallic Pt – Pt scattering path contributes to the next peak within 2.2 – 2.8 Å. The next broad peak extended up to 3.8 Å is an interference of two Pt – O scattering paths at 3.40 Å and 3.68 Å and two Pt – Pt (oxide) paths at 3.13 Å and 3.54 Å (see Figure 1.25). In the ß-PtO_2 structure the shorter Pt – Pt scattering path at 3.13 Å arrives from two edge shared [PtO_6]

octahedra and the longer Pt – Pt oxide path at 3.54 Å comes from two cornered shared [PtO_6] octahedra. However, the inclusion of the two longer Pt – O scattering paths having significantly lower amplitudes do not improve the fit to the experimental data. Since the higher Z scattering atom (Pt) has a greater effect on the Fourier transformation within this region the two Pt – O scattering paths were removed from the modeling. In the χ(R) vs R spectra of the reduced catalyst (Figure 1.19 (b)) the first peak that extends up to 3.1 Å is ascribed to be the dominant oscillation of the metallic Pt – Pt scattering path at an atomic bond distance 2.73 Å. The second Pt – Pt scattering path at 3.85 Å fits to the shoulder up to 4 Å.

The results shown in Table 1.3 carry key information about the distribution of the atomic bond distances with static bond disorders and their corresponding C.N.s resulting from the specific size and shape of the NPs. The results show that the metallic Pt scattering path has a C.N. of 3.6±0.2which is higher than the oxygen C.N. of 2.8±0.2 in the 1st co-ordination shell. This suggests the formation of a typically spherical Pt metallic core surrounded by Pt-oxide shell on the surface (Ahmadi, et al. [36]).

Table 1.3. EXAFS best fitted results of the as prepared and reduced states of 4.8wt% Pt/SiO_2 catalyst. The scattering paths Pt – Pt_O (or Pt – O – Pt bond) and Pt – Pt_M were generated from the ß-PtO_2 and Pt metal structures.

Sample name	Scattering Paths	C.N	R(Å)	σ^2(Å^2)	ΔE_0 (eV)	R-factor
As-prepared	Pt – O	2.8 ± 0.2	2.00 ± 0.02	0.003 ± 0.001	9.84 ± 0.69	0.014
	Pt – Pt_O	0.9 ± 1.7	3.13 ± 0.05	0.014 ± 0.010		
	Pt – Pt_O	3.7 ± 1.7	3.78 ± 0.04	0.013 ± 0.005		
	Pt – Pt_M	3.6 ± 0.2	2.59 ± 0.01	0.011 ± 0.003	0.35 ± 3.12	

Reduced	Pt – Pt_M	8.1 ± 0.7	2.73 ± 0.01	0.010 ± 0.001	4.28 ± 0.76	0.018
	Pt – Pt_M	2.3 ± 1.2	3.85 ± 0.04	0.015 ± 0.013		

In the as prepared state the EXAFS results show a lattice contraction in the Pt metallic core (2.59 Å) compared to Pt foil (2.77 Å) (Ankudinov, et al. [37]). Additionally, the abnormally large σ^2 value for Pt – Pt suggests a higher bond disorder present in the metallic core compared to the oxidized surface for such a nanoparticle (Frenkel, et al. [38]). The lower C.N. and shorter Pt – Pt bond in the nanoparticle also indicate a large fraction of Pt atoms remains on the surface of the metallic core (Daniel, et al. [39]) and adhere to the oxygen atoms to form an oxidized Pt shell (Jeong, et al. [40]). In the reduced state the Pt – Pt bond length is 2.73 Å and coordination number is 8.1± 0.7 which is close to the previously reported results for supported Pt NPs supported on SiO_2 (Ahmadi, et al. [36], Jeong, et al. [40], Chen, et al. [41]). The size of the metallic cluster can be obtained from the C.N. (Frenkel, et al. [42,] Jentys [43], Beale and Weckhuysen [44], Marinkovic, et al. [45]). Using the method of Jentys [43]we estimate the Pt cluster size to be ~1.3nm containing 76 atoms, which is in remarkable agreement with the STEM results. For the oxidized catalyst the C.N of 3.6 for Pt – Pt indicates a cluster of less than 10 atoms with an estimated size less than 1nm for the metallic core. To relate the mean coordination number to the particle size for the oxide shell we would need to know the oxygen atomic distribution on the particle surface – this is not obtainable with the EXAFS technique. Therefore, the average coordination number of the Pt – O shell cannot be used to estimate the size of oxidized surface.

Discussion

Applications of the method

- *Studies of simple nano systems*. In practice, characterizing ultra-small crystallites with x-ray diffraction is challenging – a fact that is echoed by the current state of the field. Gallagher, et al. [3] sought to determine the conditions under which 2.8 wt% Pt / Al_2O_3 nanoparticles (1-2nm) could be characterized with Bragg diffraction. They concluded that such particles could only be analyzed when reduced – the nanoparticles could not be detected under ambient conditions due to the oxidation of the nanoparticles. They also concluded that the increased signal to noise afforded by synchrotron radiation was required to investigate such systems (< 3nm), a point that was emphatically reiterated in later papers examining different bimetallic Pt-containing nanoparticles (2 to 3 nm) supported on silica (Wu, et al. [46], Ma, et al. [47], Wu, et al. [48]). This work demonstrates that - for simple nano systems - neither synchrotron radiation nor full reduction of the nanoparticles is required. We show that even sub-nanometer crystallites may be characterized with Bragg diffraction by benchtop equipment. We further demonstrate that characterization is possible when metal and oxide phases are present in the same sample. However, more challenging nanoscale systems, e.g., those with multiple elements / phases, may not be possible to deconvolute.

- *Independent estimation of weight loading*. For a single metal, the effect of x-ray absorption on the support may be used to give an independent estimate of the weight loading. If the methods presented in this work are applied, a sample of unknown weight loading might be estimated by determining the value of μ needed for the unknown sample so that the pure support (with known μ) can be corrected to match it. Once μ is known for the unknown sample, the corresponding weight loading can be determined. The feasibility of this would depend on the difference in μ between the support and unknown elements (the larger the difference, the more accurate the estimate). The feasibility would also depend on how well the unknown material could be separated from the support.
- Crystalline supports. The methods presented in this work also apply to crystalline supports. However, it must be noted that any change in the vertical displacement of the sample (i.e. height error or displacement error) will cause an angle-dependent shift of the Bragg peaks that must be corrected. Further details can be found in Dinnebier, et al. [18], page 24, and in Lipp [49]. Future work is planned to demonstrate XRD analyses with crystalline supports.

Limitations of the method

- *Limitations of Rietveld Refinement.* While the results obtained using the simple core-shell model are useful, the amount of information that can be obtained from the data using Rietveld refinement is limited. There are two types of coherent elastic scattering that occur in an XRD experiment:

Bragg diffraction and diffuse scattering (Dinnebier, et al. [18]). Rietveld refinement operates solely with Bragg diffraction. Diffuse scattering becomes more important as crystallite sizes decrease; Debye Function Analysis (DFA) includes both Bragg and diffuse scattering and is especially powerful in the atomic to nanometer size range and for characterizing a broad range of defects (Bertolotti, et al. [50]). One particular strength of DFA is the determination of probability distributions (e.g. size distributions). DFA can be performed on XRD data obtained with Bragg-Brentano geometry; one challenge is the proper subtraction of the background (Pakharukova, et al. [51]). The intensity correction methods presented in this work could similarly be applied before DFA analyses and therefore aid in their background subtractions. It is noted that the greater simplicity of Rietveld analysis gives it an advantage over DFA in terms of providing characterizations with quicker turn-around times (especially useful for commercial applications). Rietveld refinement may also serve as a companion to DFA: the simpler analysis quickly narrowing the scope of a system prior to the more detailed and complex method.

- *The "pure" support must be available as a separately measurable entity*. To accurately subtract the background, any non-nanocrystal part of the sample (designated with the term "support" in the following discussion) must be measurable in a separate XRD experiment. The presented method for background correction and subtraction assumes that the support is a separate entity from the nano crystallites, i.e., the nano

crystallites do not physically change the support in any significant way. If this is not true and / or a sample of the “pure” support (without nano crystals) is not available, then the background subtraction method may not be accurate. For the 4.8% Pt / SiO_2 case study presented in this work, it is reasonable to assume that the effect of the nanoparticles on the support is negligible. If each Pt atom directly affects a silicon atom, then only 0.7 wt% of the silica support will be affected.

- *The elemental composition of the sample must be known (weight loadings)*. Another limitation of the background subtraction method is that the quantitative elemental composition of the sample must be known to calculate the x-ray absorption and finite thickness effects. For unknown samples, the bulk elemental composition must first be measured, e.g., with an x-ray fluorescence (XRF) analysis or ICP-OES. Surface sensitive techniques such as x-ray photoelectron spectroscopy may not give an accurate representation of the elemental composition if the surface composition is different from the bulk.
- *Only pre-defined structures can be compared*. One of the strengths of Rietveld refinement for bulk materials (especially single crystals) is the possibility to determine the crystal structures of unknown phases. This is not applicable at the nanoscale since the peaks merge and other nano-effects become prominent. Only existing or hypothetical crystal phases can be fit to the data; the best fits are assumed to be the closest to the true structure. If the nano-crystallite consists of an unknown phase for

which the analyst has no matching structure, then characterization may not be possible.

- *The angle dependence of the atomic form factor is not corrected point-by-point*. There is an additional angle-dependent intensity factor that is not corrected for in this work: the atomic form factor. This intensity factor is highest at low angles and decreases with increasing θ, causing peak-pulling towards lower angles for broad peaks (Kaszkur [52]). For a Pt (111) peak with size broadening corresponding to a 0.87 nm domain size (the same conditions used to estimate the peak-pulling effects displayed in Table 1.1), the estimated peak pull is -0.1 ° - placing it among the least significant peak-pulling effects (a full order of magnitude lower than the Lorentz-Polarization effect). Topas does not allow for the form factor to be simply calculated on a point-by-point basis (as is the case for the other angle-dependent intensity effects); by default, in Topas the form-factor is calculated based on a peak's nominal center (d-spacing). The error introduced by not accounting for the peak-pull of this intensity effect is expected to be small; still, future work could be done to allow the form factor to be scaled on a point-by-point basis for increased accuracy.
- *Fluorescence*. Fluorescence adds another level of complexity to the analysis. The impact of fluorescence on a diffractogram is observed as an angle-independent vertical offset, as long as a constant sample volume is illuminated by the x-ray beam. The magnitude of the offset depends on the quantity and identity of the fluorescent element, and on the wavelength

used. The assumption of constant illuminated volume means that fluorescence is also impacted by beam spill and finite sample thickness, therefore corrections for fluorescence must account for these intensity effects. Whether or not an element fluoresces in the XRD depends directly on the wavelength of x-rays used. A rule of thumb for determining the possibility of fluorescence using the periodic table is as follows: for a given x-ray source element, the elements to the left of the source element in the periodic table will fluoresce (excluding the element directly next to the source element). For example, if a copper x-ray source is used, then cobalt will have the greatest amount of fluorescence, followed by iron, manganese, chromium, vanadium, titanium, and so on. In practice, if a monochromator is not used then the x-ray source element and the element immediately to the left of the source element (in this example, copper and nickel) will also exhibit fluorescence due to the Bremsstrahlung radiation given off by the source. The most accurate way to avoid fluorescence is to use an x-ray source that will not cause samples to fluoresce; this may not be possible for all researchers. Future work is needed to address the complexities of this issue, for more details see Lipp [49].

Conclusion

Bragg diffraction via benchtop XRD can be used to characterize sub-nm crystallites – much smaller than what is commonly reported in the literature. Characterization is possible even when multiple phases are present – i.e. the

particles do not need to be fully reduced. This increased ability of XRD is afforded by the careful accounting of intensity effects and is further enhanced by the enhanced signal-to-noise provided by solid state detectors. Using the methods presented in this work, it is shown that < 2nm Pt / SiO_2 nanoparticles spontaneously oxidize to form a metallic core with PtO_2 shell; XRD analysis suggests that the metallic Pt core undergoes lattice dilation. These results demonstrate the ability of Bragg diffraction via Rietveld refinement to provide useful information for the characterization of sub-nm crystallites.

Acknowledgements

Leandro (Andy) DeCastro for filming the sample prep method

Magnus J. Lipp, for helpful discussions, advice, mathematical insight, and proofreading

Funding from the National Science Foundation IGERT program (Award Number 1250052)

South Carolina Smart State Center of Catalysis for Renewable Fuels (CReF)

References

1. Wong, A.; Liu, Q.; Griffin, S.; Nicholls, A.; Regalbuto, J., Synthesis of ultrasmall, homogeneously alloyed, bimetallic nanoparticles on silica supports. *Science* **2017,** *358* (6369), 1427-1430.

2. Miller, J.; Kropf, A.; Zha, Y.; Regalbuto, J.; Delannoy, L.; Louis, C.; Bus, E.; van Bokhoven, J. A., The effect of gold particle size on AuAu bond length and reactivity toward oxygen in supported catalysts. *Journal of Catalysis* **2006,** *240* (2), 222-234.

3. Gallagher, J. R.; Li, T.; Zhao, H.; Liu, J.; Lei, Y.; Zhang, X.; Ren, Y.; Elam, J. W.; Meyer, R. J.; Winans, R. E., In situ diffraction of highly dispersed

supported platinum nanoparticles. *Catalysis Science & Technology* **2014,** *4* (9), 3053-3063.

4. O'Connell, K.; Regalbuto, J. R., High sensitivity silicon slit detectors for 1 nm powder XRD size detection limit. *Catalysis Letters* **2015,** *145* (3), 777-783.

5. Bazin, D.; Guczi, L.; Lynch, J., Anomalous wide angle X-ray scattering (AWAXS) and heterogeneous catalysts. *Applied Catalysis A: General* **2002,** *226* (1-2), 87-113.

6. Cromer, D. T.; Liberman, D., Relativistic calculation of anomalous scattering factors for X rays. *The Journal of Chemical Physics* **1970,** *53* (5), 1891-1898.

7. Cromer, D. T.; Liberman, D. A., Anomalous dispersion calculations near to and on the long-wavelength side of an absorption edge. *Acta Crystallographica Section A: Crystal Physics, Diffraction, Theoretical and General Crystallography* **1981,** *37* (2), 267-268.

8. Gallezot, P.; Avalos-Borja, M.; Poppa, H.; Heinemann, K., Structure and morphology characterization of nanometer-size metal aggregates by electron scattering patterns. *Langmuir* **1985,** *1* (3), 342-347.

9. Vogel, W.; Sachtler, W.; Zhang, Z., Formation of Metal Clusters in Zeolites Studied by Differential X-Ray Scattering. *Berichte der Bunsengesellschaft für physikalische Chemie* **1993,** *97* (3), 280-285.

10. Gnutzmann, V.; Vogel, W., Structural sensitivity of the standard platinum/silica catalyst EuroPt-1 to hydrogen and oxygen exposure by in situ X-ray diffraction. *Journal of Physical Chemistry* **1990,** *94* (12), 4991-4997.

11. Vogel, W.; Le Rhun, V.; Garnier, E.; Alonso-Vante, N., Ru clusters synthesized chemically from dissolved carbonyl: in situ study of a novel electrocatalyst in the gas phase and in electrochemical environment. *The Journal of Physical Chemistry B* **2001,** *105* (22), 5238-5243.

12. Vogel, W., Size contraction in Pt/C and PtRu/C commercial E-TEK electrocatalysts: An in situ X-ray diffraction study. *The Journal of Physical Chemistry C* **2008,** *112* (35), 13475-13482.

13. *TOPAS*, V.6.0; Bruker AXS: 2018.

14. Hubbel, J. H.; Seltzer, S. M., X-ray mass attenuation coefficients: NIST standard reference database 126. NIST: 2004.

15. Hermann, H.; Ermrich, M., Microabsorption correction of X-ray intensities diffracted by multiphase powder specimens. *Powder diffraction* **1989,** *4* (4), 189-195.

16. Zevin, L. S.; Kimmel, G.; Mureinik, I., Methodology of quantitative phase analysis. In *Quantitative X-Ray Diffractometry*, Springer: 1995; pp 100-225.

17. Brindley, G. W., XLV. The effect of grain or particle size on x-ray reflections from mixed powders and alloys, considered in relation to the

quantitative determination of crystalline substances by x-ray methods. *The London, Edinburgh, and Dublin Philosophical Magazine and Journal of Science* **1945,** *36* (256), 347-369.

18. Dinnebier, R. E.; Leineweber, A.; Evans, J. S. O., *Rietveld refinement: practical powder diffraction pattern analysis using Topas*. Walter de Gruyter GmbH: Berlin/Boston, 2019.

19. Pecharsky, V. K.; Zavalij, P. Y., *Fundamentals of Powder Diffraction and Structural Characterization of Materials*. 2nd ed.; Springer: 2009.

20. Pitschke, W.; Mattern, N.; Hermann, H., Incorporation of microabsorption corrections into Rietveid analysis. *Powder Diffraction* **1993,** *8* (4), 223-228.

21. Hermann, H.; Ermrich, M., Microabsorption of X-ray intensity in randomly packed powder specimens. *Acta Crystallographica Section A: Foundations of Crystallography* **1987,** *43* (3), 401-405.

22. Harrison, R. J.; Paskin, A., The effects of granularity on the diffracted intensity in powders. *Acta Crystallographica* **1964,** *17* (4), 325-331.

23. Suortti, P., Effects of porosity and surface roughness on the X-ray intensity reflected from a powder specimen. *Journal of Applied Crystallography* **1972,** *5* (5), 325-331.

24. Pitschke, W.; Hermann, H.; Mattern, N., The influence of surface roughness on diffracted X-ray intensities in Bragg–Brentano geometry and its effect on the structure determination by means of Rietveld analysis. *Powder Diffraction* **1993,** *8* (2), 74-83.

25. Schreier, M.; Regalbuto, J. R., A fundamental study of Pt tetraammine impregnation of silica: 1. The electrostatic nature of platinum adsorption. *Journal of Catalysis* **2004,** *225* (1), 190-202.

26. Miller, J. T.; Schreier, M.; Kropf, A. J.; Regalbuto, J. R., A fundamental study of platinum tetraammine impregnation of silica: 2. The effect of method of preparation, loading, and calcination temperature on (reduced) particle size. *Journal of Catalysis* **2004,** *225* (1), 203-212.

27. Xia, Y.; Harrison, P.; Ornelas, I.; Wang, H.; Li, Z., HAADF-STEM image analysis for size-selected platinum nanoclusters. *Journal of microscopy* **2020,** *279* (3), 229-233.

28. Wojdyr, M., Fityk: a general-purpose peak fitting program. *Journal of Applied Crystallography* **2010,** *43* (5-1), 1126-1128.

29. Bucher, J.; Buttet, J.; Van der Klink, J.; Graetzel, M., Electronic properties and local densities of states in clean and hydrogen covered Pt particles. *Surface Science* **1989,** *214* (3), 347-357.

30. Banerjee, R.; Liu, Q.; Tengco, J. M. M.; Regalbuto, J. R., Detection of Ambient Oxidation of Ultrasmall Supported Platinum Nanoparticles with Benchtop Powder X-Ray Diffraction. *Catalysis Letters* **2017,** *147* (7), 1754-1764.

31. Lamber, R.; Wetjen, S.; Jaeger, N. I., Size dependence of the lattice parameter of small palladium particles. *Physical Review B* **1995,** *51* (16), 10968.

32. Goyhenex, C.; Henry, C.; Urban, J., In-situ measurements of the lattice parameter of supported palladium clusters. *Philosophical Magazine A* **1994,** *69* (6), 1073-1084.

33. Jacobs, J.; Schryvers, D., A high-resolution electron microscopy study of photodeposited Pd particles on TiO2 and their oxidation in air. *Journal of Catalysis* **1987,** *103* (2), 436-449.

34. Du, K.; Ernst, F.; Pelsozy, M.; Barthel, J.; Tillmann, K., Expansion of interatomic distances in platinum catalyst nanoparticles. *Acta materialia* **2010,** *58* (3), 836-845.

35. Momma, K.; Izumi, F., VESTA 3 for three-dimensional visualization of crystal, volumetric and morphology data. *Journal of applied crystallography* **2011,** *44* (6), 1272-1276.

36. Ahmadi, M.; Timoshenko, J.; Behafarid, F.; Roldan Cuenya, B., Tuning the structure of Pt nanoparticles through support interactions: an in situ polarized X-ray absorption study coupled with atomistic simulations. *The Journal of Physical Chemistry C* **2019,** *123* (16), 10666-10676.

37. Ankudinov, A.; Rehr, J.; Low, J. J.; Bare, S. R., Sensitivity of Pt x-ray absorption near edge structure to the morphology of small Pt clusters. *The Journal of chemical physics* **2002,** *116* (5), 1911-1919.

38. Frenkel, A. I.; Hills, C. W.; Nuzzo, R. G., A view from the inside: complexity in the atomic scale ordering of supported metal nanoparticles. *The Journal of Physical Chemistry B* **2001,** *105* (51), 12689-12703.

39. Daniel, O. M.; DeLaRiva, A.; Kunkes, E. L.; Datye, A. K.; Dumesic, J. A.; Davis, R. J., X-ray Absorption Spectroscopy of Bimetallic Pt–Re Catalysts for Hydrogenolysis of Glycerol to Propanediols. *ChemCatChem* **2010,** *2* (9), 1107-1114.

40. Jeong, E.-S.; Park, C.-I.; Jin, Z.; Hwang, I.-H.; Son, J.-K.; Kim, M.-Y.; Choi, J.-S.; Han, S.-W., Temperature-Dependent Local Structural Properties of Redox Pt Nanoparticles on TiO 2 and ZrO 2 Supports. *Catalysis Letters* **2015,** *145* (3), 971-983.

41. Chen, J. Z.; Gao, J.; Probus, P. R.; Liu, W.; Wu, X.; Wegener, E. C.; Kropf, A. J.; Zemlyanov, D.; Zhang, G.; Yang, X., The effect of strong metal–support interaction (SMSI) on Pt–Ti/SiO 2 and Pt–Nb/SiO 2 catalysts for propane dehydrogenation. *Catalysis Science & Technology* **2020,** *10* (17), 5973-5982.

42. Frenkel, A. I.; Yevick, A.; Cooper, C.; Vasic, R., Modeling the structure and composition of nanoparticles by extended X-ray absorption fine-structure spectroscopy. *Annual Review of Analytical Chemistry* **2011,** *4*, 23-39.

43. Jentys, A., Estimation of mean size and shape of small metal particles by EXAFS. *Physical Chemistry Chemical Physics* **1999,** *1* (17), 4059-4063.

44. Beale, A. M.; Weckhuysen, B. M., EXAFS as a tool to interrogate the size and shape of mono and bimetallic catalyst nanoparticles. *Physical Chemistry Chemical Physics* **2010,** *12* (21), 5562-5574.

45. Marinkovic, N. S.; Sasaki, K.; Adzic, R. R., Determination of single-and multi-component nanoparticle sizes by X-ray absorption spectroscopy. *Journal of The Electrochemical Society* **2018,** *165* (15), J3222-J3230.

46. Wu, Z.; Wegener, E. C.; Tseng, H.-T.; Gallagher, J. R.; Harris, J. W.; Diaz, R. E.; Ren, Y.; Ribeiro, F. H.; Miller, J. T., Pd–In intermetallic alloy nanoparticles: highly selective ethane dehydrogenation catalysts. *Catalysis Science & Technology* **2016,** *6* (18), 6965-6976.

47. Ma, Z.; Wu, Z.; Miller, J. T., Effect of Cu content on the bimetallic Pt–Cu catalysts for propane dehydrogenation. *Catalysis, Structure & Reactivity* **2017,** *3* (1-2), 43-53.

48. Wu, Z.; Bukowski, B. C.; Li, Z.; Milligan, C.; Zhou, L.; Ma, T.; Wu, Y.; Ren, Y.; Ribeiro, F. H.; Delgass, W. N., Changes in catalytic and adsorptive properties of 2 nm Pt3Mn nanoparticles by subsurface atoms. *Journal of the American Chemical Society* **2018,** *140* (44), 14870-14877.

49. Lipp, J. W. Fine Points for Broad Bumps: the Extension of Rietveld Refinement for Benchtop Powder XRD Analysis of Ultra-small Supported Nanoparticles. University of South Carolina, 2021.

50. Bertolotti, F.; Moscheni, D.; Guagliardi, A.; Masciocchi, N., When Crystals Go Nano–The Role of Advanced X-ray Total Scattering Methods in Nanotechnology. *European Journal of Inorganic Chemistry* **2018,** *2018* (34), 3789-3803.

51. Pakharukova, V. P.; Yatsenko, D. A.; Gerasimov, E. Y.; Vlasova, E.; Bukhtiyarova, G. A.; Tsybulya, S. V., Total Scattering Debye Function Analysis: Effective Approach for Structural Studies of Supported MoS2-Based Hydrotreating Catalysts. *Industrial & Engineering Chemistry Research* **2020,** *59* (23), 10914-10922.

52. Kaszkur, Z. In *Test of applicability of some powder diffraction tools to nanocrystals*, Ninth European Powder Diffraction Conference, Oldenbourg Wissenschaftsverlag: 2015; pp 147-154.

53. Block, B.; Bailar Jr, J. C., The Reaction of Gold (III) with Some Bidentate Coördinating Groups1. *Journal of the American Chemical Society* **1951,** *73* (10), 4722-4725.

54. Noble, S. R.; Barnes, S. E.; Banerjee, R.; Miller, J.; Regalbuto, J. R., Supported nanoparticle synthesis with Au bis-Ethylenediamine: The mechanism of adsorption onto oxides and carbons. *Journal of Catalysis* **2021,** *393*, 344-356.

55. Mendenhall, M. H.; Henins, A.; Hudson, L. T.; Szabo, C. I.; Windover, D.; Cline, J. P., High-precision measurement of the x-ray Cu Kα spectrum. *Journal of Physics B: Atomic, Molecular and Optical Physics* **2017,** *50* (11), 115004.

56. Hoffman, A. S.; Singh, J. A.; Bent, S. F.; Bare, S. R., In situ observation of phase changes of a silica-supported cobalt catalyst for the Fischer–Tropsch process by the development of a synchrotron-compatible in situ/operando powder X-ray diffraction cell. *Journal of synchrotron radiation* **2018,** *25* (6), 1673-1682.

57. Asundi, A. S.; Hoffman, A. S.; Chi, M.; Nathan, S. S.; Boubnov, A.; Hong, J.; Bare, S. R.; Bent, S. F., Enhanced alcohol production over binary Mo/Co carbide catalysts in syngas conversion. *Journal of Catalysis* **2020,** *391*, 446-458.

58. Ravel, B.; Newville, M., ATHENA, ARTEMIS, HEPHAESTUS: data analysis for X-ray absorption spectroscopy using IFEFFIT. *Journal of synchrotron radiation* **2005,** *12* (4), 537-541.

59. Lytle, F., Report of the international workshop on standard and criteria in x-ray absorption spectoroscopy. *Physica* **1989,** *158*, 701-722.

60. rowlesmr; AlanCoelho, LP_Factor_X. In *Forum>Topas*, Topas Forum: 2019.

Supplementary Info

Choosing crystalline references

There are times when it is helpful or even necessary to use a crystalline reference to identify the baseline (e.g., when determining the sample holder contribution of a diffractogram). In these instances, it is important that the reference sample used is highly crystalline. Figure 1.21 compares two potential crystalline samples with their sample holder contribution (all intensities corrected to a NIST 1976c intensity standard). The potassium chloride sample makes a decent reference: it follows the empty sample holder at low angles and the areas between the peaks can be used to approximate the baseline. In contrast, the diamond sample (NanoAmor Diamond Nanopowder, synthesized, 98+%, 3-10nm) does not work well as a reference since its diffractogram contains a significant amount of amorphous scattering in addition to the crystalline peaks.

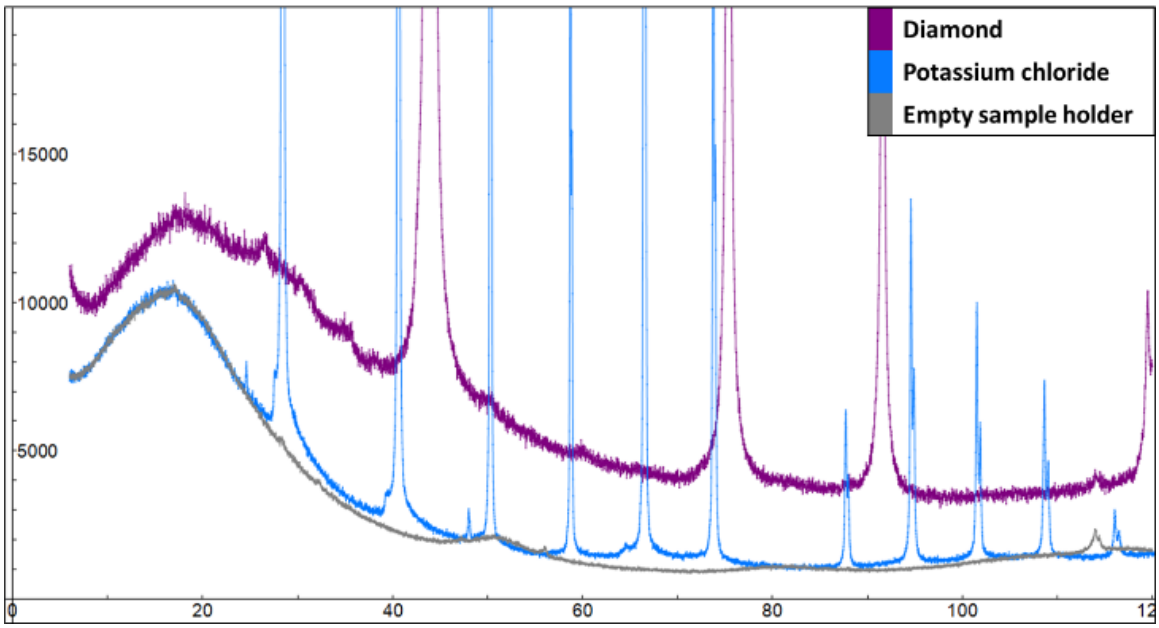

Figure 1.21. Comparing crystallinity of potential powder references.

For samples of mixed phases, there is a trade-off between the need for high crystallinity and the requirement to keep the particles of each individual phase small to reduce microabsorption. Recall that one observed effect of microabsorption appears when a sample of mixed phases is adjusted for absorption: in low absorbing phases ($\mu_i < \bar{\mu}$) the adjusted intensity will be amplified, while high absorbing phases ($\mu_i > \bar{\mu}$) will be diminished (Zevin, et al. [16]). While large crystallites with sharp peaks are desirable in a reference material for the ease of identifying the baseline, smaller crystallites reduce the errors introduced by microabsorption. Table 1.4 shows how mean particle size *B*, density ρ, and x-ray mass attenuation (μ / ρ) are related to the propensity for microabsorption. Recall that fine powders with minimal microabsorption are classified by Brindley [17] as having μB < 0.01, for multiple elements this corresponds to $\bar{\mu}B$ < 0.01. From Table 1.4 it is seen that the minimum mean size

required to achieve $\bar{\mu}B < 0.01$ depends on the elements present and their density; Au, with high μ and μ / ρ requires sizes less than 25nm to meet this requirement. For other lighter references such as NiO much higher particle sizes are allowed. The goal of choosing a reference is finding a good balance between crystallinity and microabsorption; we now suggest a minimum size for sufficiently sharp peaks to be 20-30 nm, and a maximum size for low microabsorption to be defined by $\bar{\mu}B < 0.01$.

Table 1.4. Size, density, and x-ray mass attenuation vs. propensity for microabsorption effects. Smaller μB values correspond to less microabsorption.

Powder	***B* (*μ*m)**	**ρ (g cm^{-3})**	**$\bar{\mu} / \rho$ (cm^2 g^{-1})**	**$\bar{\mu}B$ (dimensionless)**
W	1 to 5	19.3	169	0.3 to 1.6
Mo	2 to 4	10.3	155	0.3 to 0.6
Sn	10	7.27	247	1.8
Cu	2 to 3.5	8.96	52	0.1 to 0.2
Ag	0.6 to 2	10.49	214	0.1 to 0.4
NiO	< 0.05	6.67	41	< 0.0014
Co_3O_4	0.05 to 0.08	6.07	255	0.008 to 0.012
Co_3O_4 (10 nm)	0.01	6.07	255	0.002
Au (10 nm)	0.01	19.3	205	0.004

Experimental methods

Sample synthesis and preparation

Synthesis of Pt nanoparticles on silica support

Aerosil 300 (A300) silica obtained from Evonik was used as the support. The BET surface area, as determined from nitrogen adsorption-desorption isotherms with a Micromeritics 2020 ASAP instrument, was 330 m^2 / g and the Point of Zero Charge (PZC) was 3.9. Based on the PZC of the A300, the cationic precursor tetraammineplatinum (II) chloride ([PTA, $Pt(NH_3)_4]OH_2$, 99.999%) was

selected to adsorb the Pt complexes onto the silica support using Strong Electrostatic Adsorption (SEA). The silica was weighed out to obtain the desired 1000 m^2/L surface loading and the PTA solution at the required concentration was then contacted with the support for an hour at the optimal pH of 12. The catalyst slurry was then filtered, dried in ambient air overnight, and oven dried in static air at 120°C for 16 hrs. The dried support was reduced in a flowing 10% H_2 (balance He) for 1 hr at 200°C at a ramp rate of 2.5°C/min to obtain the Pt nanoparticles. The resulting weight loading for the Pt on A300 catalyst was 4.8%, as determined by ICP-OES. After STEM imaging and initial XRD characterization, the sample was aged in a glass sample vial with a screw-top for ~ 36 months. After this time period further XRD characterization revealed no significant change in the Pt sample; it was then analyzed with the methods presented in this work. A reference support was prepared by pH treating and heat treating pure A300 silica under similar conditions to the respective SEA sample, only with no precursor.

Synthesis of Au nanoparticles on silica support

Amorphous SiO_2 (Aerosil 300) was used directly from Evonik, the point of zero charge (PZC), surface area, and water accessible volume of which were 3.4, 304 m^2/g and 2.5 ml/g, respectively. For this low PZC material a cationic gold precursor, gold bis-ethylenediamine $[Au(en)_2Cl_3]$, was prepared according to the literature (Block and Bailar Jr [53]) using chloroauric acid, ethylenediamine, ethyl ether and anhydrous ethanol, all from Alfa Aesar. Supported gold catalysts were then prepared by the SEA and DI (dry impregnation, i.e. incipient wetness) methods described in the previous report (Noble, et al. [54]). The SEA protocol was

modified to prepare lower weight loading Au samples as follows: the freshly prepared $Au(en)_2Cl_3$ solution was diluted to concentrations of 40 ppm, 87 ppm, and 100 ppm; each concentration was adjusted by an NaOH solution to a pH of 11.7 to get the maximum uptake of $Au(en)_2Cl_3$. The required amount of support was then added to each solution to give a surface loading of 1000 m^2/L. Each solution was shaken for 1 h, vacuum filtered, and dried in a fume hood for 72h. Mass loadings of the Au SEA samples were determined by ICP-OES to be 0.84% Au, 2.2% Au, and 2.6% Au for the 40 ppm, 87 ppm, and 100 ppm solutions, respectively. SiO_2 supported Au nanoparticles by the DI method were synthesized at the same weight loading as the SEA samples and dried under the same conditions. Gold samples were reduced in a horizontal reduction furnace under 20% H_2 in N_2 with a total flow rate of 250 sccm at 400^0C for 1h with a ramp of 5°C/min. The samples were aged in a glass sample vial with a screw-top for > 5 months prior to the XRD shown in this work. Reference supports were prepared by pH treating and heat treating pure A300 silica under similar conditions to the SEA samples, only with no precursor.

Scanning Transmission Electron Microscopy

High and low magnification Z-contrast images of the 4.8% Pt / A300 catalyst were obtained with an aberration-corrected JEOL 2100F High Angle Annular Dark-Field scanning transmission electron microscope (STEM) equipped with a 200 kV field emission gun and a double tilt holder for tilting the sample across a range of angles (±20°). The microscope is attached to a Fischione Model 3000 HAADF detector with a camera length such that the inner cut-off angle of the detector is 50

mrad. Sample preparation involved suspending the catalyst in isopropanol and depositing a drop of the suspension onto a holey carbon film attached to a Cu TEM grid. Sample preparation involved ultrasonicating the sample in isopropanol and adding a drop to a copper TEM grid with a thin holey carbon coating. The images were recorded using Gatan Digital Micrograph software and particle size distributions were obtained by counting > 1700 particles on the sample. Particle size analysis was performed using Particule2 software (Comptage de particules version 2.0). Ellipses with the hemisphere model were used to fit the projected area of each nanoparticle and obtain a corresponding “diameter”.

XRD

Sample Preparation for XRD

The nanoparticle samples and treated supports were finely ground with an agate mortar and pestle prior to loading into the sample holder. The samples and supports were all measured in the same sample holder (a “Zero Diffraction Plate” from MTI corporation custom-mounted into an aluminum holder from Rigaku [MiniFlex II Base Unit # 2005H303]). The Zero Diffraction Plate consisted of a single crystal of P-type, B-doped silicon cut at a high index plane 24.6mm in diameter and 1.0 mm thick with a center cavity nominally 10 mm in diameter and 0.2 mm deep (measured in-house to be 10.2 mm in diameter and 0.29 mm deep). Prior to loading the samples into the holder, it was determined that approximately 8.0 mg of the sample/support would properly fill the center cavity; this was the mass targeted for both loadings (using an initial target mass minimizes the amount

of correction needed to adjust supports to their respective nanoparticle samples and thus reduces the overall error of the background subtraction). For each sample, the target mass was measured out and loaded into the sample holder as follows: once the target mass was deposited into the center cavity of the sample holder, an antistatic microspatula (VWR) was used to evenly distribute the sample across the cavity and then tuck in the sample about 1mm from the cavity edges (to minimize sample spilling from the cavity during smoothing). A strip of wax paper was placed against a glass slide and gently rotated back and forth across the surface of the sample to smooth it. Once smooth, the sample holder mirror around the sample was wiped down gently with a Kim wipe (wrapped around the tip of a microspatula for fine motor control). This cleaning typically left a small ring of sample on the surface of the mirror adjacent to the sample (Figure 1.22) since the entire sample would need to be re-prepared if the Kim wipe disturbed the surface. Such cleaning of the mirror was necessary to minimize errors in the beam spill correction, and to keep differences due to sample preparation between nanoparticle samples and their references to a minimum. The prepared sample was visually inspected to confirm a homogeneous, smooth surface. It is noted that if electrostatic cling is a problem, the sample holder, wax paper, and glass slide may all be pressed against a grounded metal plate to remove the extra charge before smoothing.

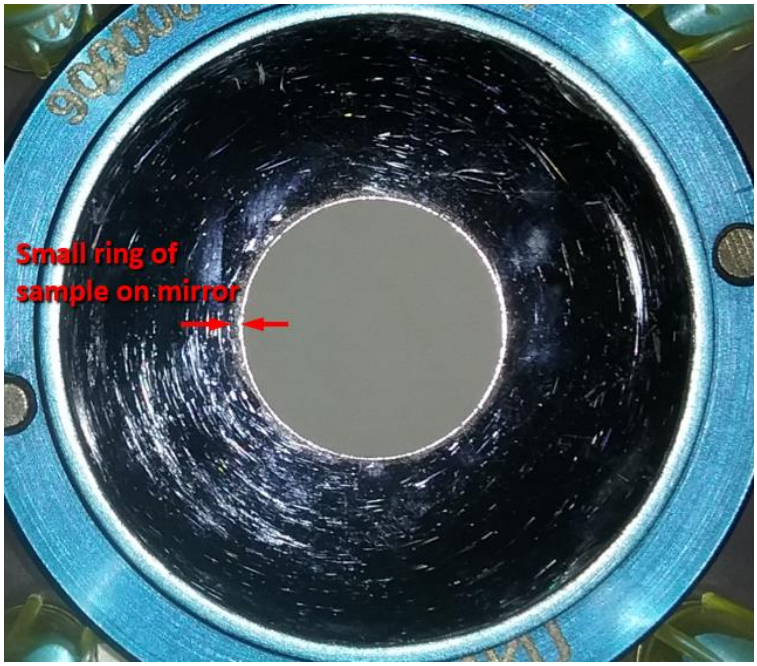

Figure 1.22. The amount of sample on the mirror should be minimized and consistent between samples.

XRD Measurement

The nanoparticle samples and pure treated supports were measured one at a time in a Rigaku MiniFlex II Powder X-ray diffractometer equipped with a silicon strip D/tex Ultra linear position sensitive detector (LPSD) and operating at 30kV and 15mA in Bragg-Brentano geometry with the following hardware parameters: goniometer radius = 150mm, primary and secondary Soller slits = 5° (2θ), divergence slit = 1.25° (2θ), antiscatter slit = 8 mm, no receiving slit, and LPSD angular range of 4.89° (2θ). Because the x-ray source flux showed significant variation over time (believed to be a result of using cooling water without temperature control), each sample was scanned six times from 6 to 120° 2θ with a sampling width of 0.02° (2θ) and scan rate of 5° min^{-1}. This rather high scan rate was used to minimize the amount of intensity drift during each scan. The (1 0 4)

reflection of a NIST 1976c intensity standard was measured before and after each scan from 34.8 to 35.6° 2θ at a scan rate of 2° min^{-1} and sampling width of 0.01° 2θ. This reflection was fit as a fundamental parameter peak in Topas V.6.0; the resulting scale factor was recorded and used to normalize all sample scans to a common x-ray source intensity using Microsoft Excel. The method for normalizing each sample scan was to assign every data point a scale factor obtained from linearly interpolating between the NIST 1976c scale factors taken directly before and after each scan based on the time at which each data point was measured. Once normalized, the six scans taken for each sample were averaged together to give a total scan rate equivalent to around 0.83° (2θ) min^{-1}. At the conclusion of each XRD measurement, the mass of the sample in the sample holder cavity was measured and recorded.

Correcting the support for sample effects

Intensity-corrected diffractograms were collected for the nanoparticle samples, pure supports, empty sample holder, and ceria powder (used in this work because it is highly crystalline and opaque to Cu K-α radiation: $\mu/\rho = 302.7\ cm^2\ g^{-1}$). As discussed in the Step 2: Accurately estimating the background section of this work (page 10), the ceria sample and empty sample holder were used to identify the sample independent and sample dependent contributions of the sample holder to the total nanoparticle diffraction pattern. When compared to the Pt and silica support contributions (Figure 1.3), it was determined that for our sample holder the sample dependent contribution is small compared to the contributions from the sample. It was therefore deemed unnecessary to estimate

the sample holder contribution more accurately. The reasoning for this is as follows: the corrections to the support are small in this case (due to low metal weight loadings and the use of a target mass to ensure similar masses between the samples and supports). Since the sample holder contribution to the diffractogram is subtracted before the support is corrected for sample effects and added back after, the error in determining the sample holder contribution will result in a small percent of a small correction. The overall error can therefore be considered negligible for this case. With this reasoning, the sample holder contribution to the diffractograms was estimated from the empty sample holder diffractogram (Figure 1.14-A) and subtracted from the support (Figure 1.14-B). Microsoft Office Excel was then used to correct the diffractogram of the silica support for differences in absorption and finite sample thickness, as described in the main body of this work. The x-ray mass attenuation coefficients (μ / ρ) were calculated from NIST elemental values (table 3 of Hubbel and Seltzer [14]); the x-ray linear absorption coefficients ($\bar{\mu}$) were then calculated for each sample using the sample mass recorded after the XRD experiment, the metal weight loading, and the sample holder dimensions. A user-friendly Microsoft Excel workbook was created to expedite the calculation of μ values, this workbook is included in the supplementary information. For the series of Au diffractograms shown in Figure 1.2, each diffractogram was corrected to a common mass and μ value in order to depict the precision afforded by the correction.

Analysis with Rietveld Refinement

Rietveld refinement was performed using Topas V.6 (Bruker AXS). An instrument profile was created using a coupled refinement on multiple scans of a NIST 1976c intensity standard (see the .pro file included in the supplementary information), though it is noted that for such small nanoparticles the scattering is dominated by the sample contributions (Bertolotti, et al. [50]). The emission profile used was obtained from Mendenhall, et al. [55] and consists of eight separate wavelengths. Hardware parameters such as goniometer radius, divergence slit angle, sample length, and sample thickness were fixed based on nominal and measured values. Equatorial convolutions were addressed using a point detector model with tube tails (the LPSD model was not used since it did not allow certain angle-dependent intensity effects to be scaled point-by-point). Axial convolutions were handled by a Full Axial model. Peak shift corrections (zero error and sample displacement) were fixed based on values refined for samples with sharp peaks. For angle-dependent intensity corrections (Lorentz-Polarization, absorption, beam spill, and surface roughness) the Topas macros were modified to work on a point-by-point basis. The beam spill macro was also updated to include the 2D correction for circular sample holders, and some other "bugs" were fixed (see the *Topas Code Changes* section for full documentation of the modifications).

For the Pt nanoparticle refinement, the corrected silica support (with background added back) was imported into Topas. The absorption value that the support had been corrected to (i.e. μ = 15.94 cm^{-1} for the 4.8% Pt / SiO_2 sample) was used for absorption correction in Topas. The desired fitting range was

selected, and the corrected support was then fit with a high order Chebyshev polynomial. Once fit, the coefficients of the Chebyshev polynomial were fixed, thus preserving the “background” (true background plus sample holder and support scattering) for the nanoparticle analysis. The Pt diffractogram was then imported into Topas. Twelve platinum and platinum oxide structures were identified and imported from the ICSD database (Table 1.2). These twelve phases were fit individually and in combinations of up to three phases. For the first fits, only the overall scale factor for each phase and gaussian size broadening were allowed to refine; all other parameters were fixed as described above. Once promising phase combinations were identified, the lattice parameter of the metallic Pt was allowed to refine, together with two terms for surface roughness that were constrained as discussed in the *Microabsorption and Surface Roughness* section of this work. The total number of independently refined terms during the final analyses for two phases was therefore seven.

XAS

Instrumental Setup

The XAS data were collected at Continuous XAS beamline 9-3 at SSRL. The beamline uses a 20 pole, 2-Tesla Wiggler insertion device placed within the 3 GeV storage ring with beam current ~500 mA. The harmonic rejection was done by detuning the mirror (M0) placed prior to the monochromator to reduce the flux at 500 eV above the Pt L3 absorption edge to nearly 40% of the maximum intensity. The beam size was 1 mm [v] × 4 mm [h]. The XAS data were collected in

transmission mode using two 15 cm long ionization chambers (IC) filled with argon gas. The angle of the monochromator was set to 90° and the energy was tuned from 11,365 to 12,537 eV for a complete absorption spectrum. A 7.5 μm thick Pt foil was placed in front of a 3rd IC to measure the absorption spectra of the foil simultaneously as a reference for energy calibration.

Approximately 40 mg of the undiluted 4.8 wt% Pt/SiO_2 sample was loaded as received in a Kapton tube with 3.0 mm outer diameter, 25μm wall thickness. A catalyst bed of 10 mm was filled to achieve total absorption of 2.5 above the edge with an estimated edge step $\Delta\mu$~0.62. The tube was fitted gas-tight using rubber O-ring and placed at the center of the custom build reactor cell (Hoffman, et al. [56]). The details of the in-situ cell connections and setup are explained elsewhere (Asundi, et al. [57]).

In-situ data collection procedure

The in-situ XAS data were collected in different stages of a temperature programmed reduction process. Before the in-situ experiment was started the pipelines and gas flow systems were purged with He gas to remove excess amounts of air and moisture inside. At the beginning one scan was collected at room temperature with flowing He gas (20 ml/min) through the reactor to see the signal to noise ratio; once the sample stabilized under the He flow 4 scans were collected on the as-received sample at room temperature. Next the sample was heated from room temperature to 100°C at a 5°C/min ramp rate and 30 minute dwell time until no change in the XANES spectra was observed. Following the desorption, the sample was cooled down to room temperature and steady state

scans were recorded at room temperature under He flow. The reduction process was started by introducing the H_2 gas into the reactor at a flow rate of 2 ml/min and reducing the He flow rate to 18 ml/min to keep the total flow rate constant at 20 ml/min. After the H_2 gas was observed in the product stream the sample was heated up to 200°C with a 5°C/min ramp rate and dwelled for 30 minutes until no further changes in the XANES spectra were observed and the absorption edge approximated the Pt foil reference. The steady state scans were taken at room temperature after cooling down the sample in the presence of pure He flow to avoid any hydride formation. It is to be noted that in every steady state condition, a total of 4 scans were collected and merged to increase the signal to noise ratio. These steady state scans measured under He at room temperature are defined as (i) as-prepared, (ii) desorbed, and (iii) reduced.

EXAFS data modeling

The experimentally obtained absorption spectra (μ(E) vs E) were processed using ATHENA software and analyzed with ARTEMIS software using FEFF6.0 code - a part of the Demeter (Ravel and Newville [58]) software package. The χ(k) data of the as-prepared catalyst was Fourier transformed within the k range of 3.1 – 12.4 $Å^{-1}$ and fitted in the R range of 1.0 – 3.6 Å. The Nyquist criteria for the number of independent parameters could be varied simultaneously $NI = (2\Delta k \Delta r)/\pi + 1$ (Lytle [59]) and indicated a maximum of 16 fitting parameters. The data for the reduced catalyst was Fourier transformed within the k range of 3.0 – 13.4 $Å^{-1}$ and fitted in the R range of 1.5 – 4.0 Å. The passive amplitude reduction factor (S02) was obtained as 0.84 ± 0.06 by fitting the Pt metal foil as shown in Figure 1.23.

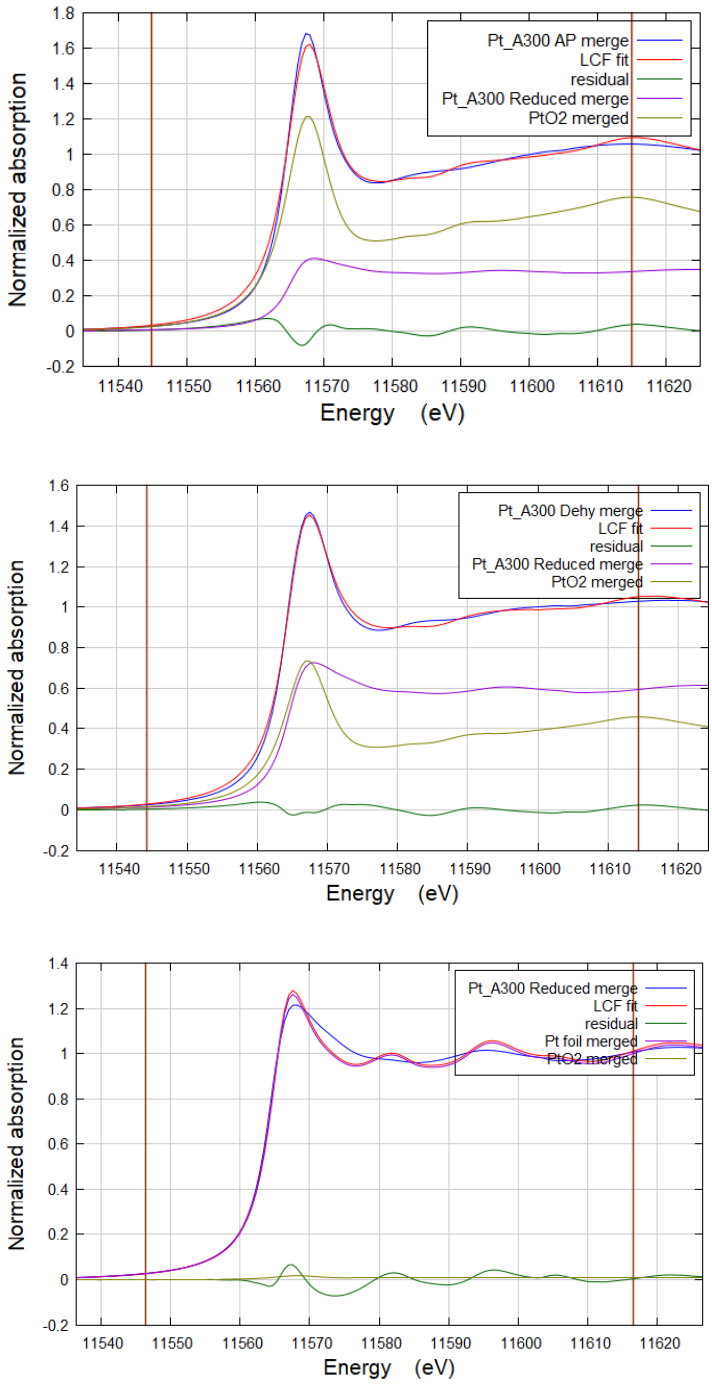

Figure 1.23. LCF fitting of steady states conditions. It is assumed that the catalyst is fully metallic in the reduced state and the difference in the post edge regions comes due to the nanoparticle size effect. Therefore, the reduced state spectrum was used as a standard to fit the other states instead of using Pt foil. The phase fractions are (top) as prepared state: 66.2% Pt NP/ reduced and 33.8% PtO2, (middle) desorbed state: 59.7% Pt NP/ reduced and 40.3% PtO2, and (bottom) 99.8% reduced state Pt foil and 0.02% PtO2. Fitting range E0 -30 to E0+ 50 eV (This is a guide to the EXAFS modelling.)

Based upon the XRD results, the individual scattering paths were generated from fcc Pt (ICSD-52250) and orthorhombic β-PtO2 (ICSD-202407) structures to fit the EXAFS data of the as prepared and desorbed states. Only the fcc Pt structure was used to fit the EXAFS data of the reduced state. The Pt – O and Pt – Pt (oxide) single scattering paths were generated from the mentioned PtO_2 structure and the Pt – Pt metallic scattering path was generated from the Pt metal. In the first coordination shell two degenerate Pt – O scattering paths were merged together to one path with a total degeneracy of 6. Next the change in the bond length (ΔR), static bond disorder (σ2) and the correction to the threshold energy (ΔE0) were varied independently. Different ΔE0 parameters were defined for metallic and oxide phases. Given that the samples were air exposed, it was assumed that the under coordinated Pt atoms on the particle surface or first few layers of surface atoms would be oxidized, giving a bonding path coordination number (C.N) between that of bulk oxide (Pt-O = 6) and bulk metal (Pt-Pt = 12). Therefore, a constrained model was used to parameterize the C.N of the scattering paths in the oxidized states. For the fitting of the as prepared catalyst, the atoms at bonding distances from absorbing Pt atoms were factorized by a free parameter ‘x’ and the Pt atoms at nonbonding distances or connected to a bridging oxygen atom were factorized by a parameter ‘y’. This means the degeneracy of Pt – O path at 1.99 Å was multiplied by ‘x’ and the degeneracy of Pt – Pt metallic scattering path at 2.77 Å was multiplied by (1-x), while the degeneracy of Pt – O – Pt single scattering paths were multiplied by ‘y’ imposing the fact that $y \leq x$. Thus the value of ‘x’ was first obtained by fitting the 1st coordination shell and then the

value of ‘y’ was restrained with a maximum value equal to ‘x’. After carefully investigating the response of the scattering paths, the two Pt – O scattering paths at 3.18Å and 3.65Å distances were excluded from the model as they do not give sensible and good fit to the data. Thus, the fitting of the as prepared catalyst was done using the multiple shell approach with Pt – O at 1.99Å, two Pt – Pt (oxide) at 3.15Å and 3.56Å from the orthorhombic PtO_2 structure and a Pt – Pt (metallic) at 2.77Å from the fcc Pt structure. The best fit of the reduced catalyst was performed considering two metallic Pt – Pt scattering paths at 2.77Å and 3.92Å distances.

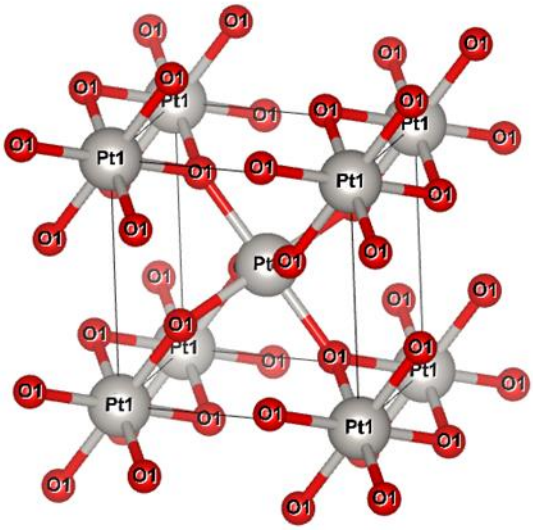

Figure 1.24. Vesta structure representation of ß-PtO_2 (space group 58).

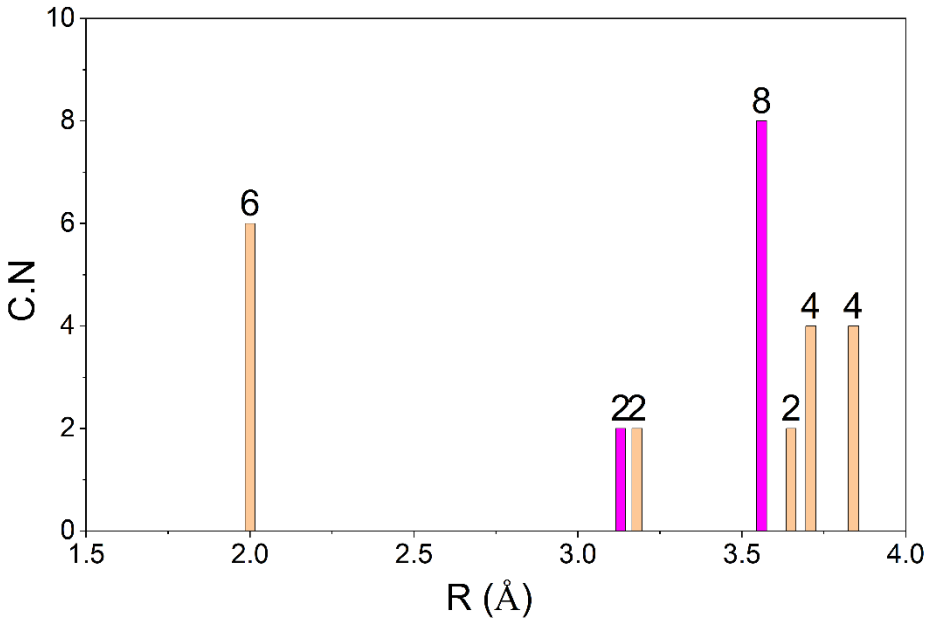

Figure 1.25. Histogram stick plots of the scattering paths with their corresponding degeneracy of the β-PtO2 phase (ICSD-202407). Orange bars represent the Pt – O and pink bars represent the Pt – Pt oxide single scattering paths.

Beam Spill derivations

Derivation of expressions for s_1 and s_2 (no displacement error)

An X-ray beam passing through a divergence slit of width ϕ will strike a perfectly aligned sample (i.e., no displacement error) as shown in Figure 1.26. In order to get an expression for s_1 and s_2 in terms of ϕ, the goniometer radius R, and incident angle θ we can use the following trigonometric relationships:

$$\gamma_1 + \theta + \frac{\varphi}{2} = 180° \rightarrow \gamma_1 = 180° - \theta - \frac{\varphi}{2} \quad \text{Eq. 34}$$

Similarly,

$$(180° - \theta) + \frac{\varphi}{2} + \gamma_2 = 180° \rightarrow \gamma_2 = \theta - \frac{\varphi}{2} \quad \text{Eq. 35}$$

The law of sines together with the relationship sin(180°-θ) = sin(θ) gives an expression for s_1:

$$\frac{s_1}{sin(\varphi/_2)} = \frac{R}{sin(\gamma_1)} \rightarrow s_1 = \frac{R \cdot sin(\varphi/_2)}{\sin(\theta + \varphi/_2} \quad \text{Eq. 36}$$

Similarly,

$$s_2 = \frac{R \cdot sin(\varphi/_2)}{\sin(\theta - \varphi/_2} \quad \text{Eq. 37}$$

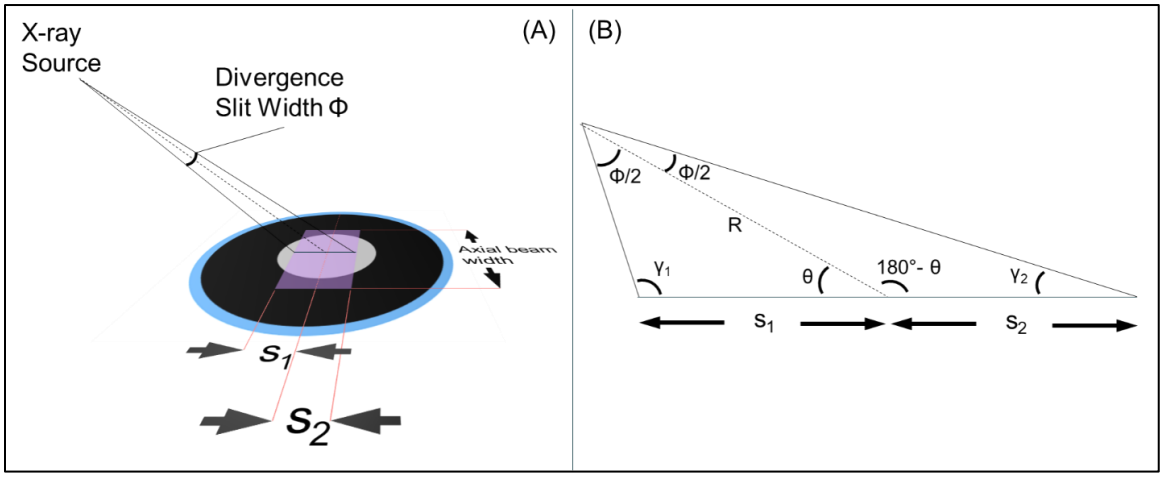

Figure 1.26. The trigonometry of beam spill. A) How the divergence angle ϕ is related to s_1 and s_2. B) Trigonometric relationships.

Derivation of expressions for s_1' and s_2' (with displacement error)

With a vertical sample displacement *h*, further adjustments to Eq. 36 and Eq. 37 are needed. Consider Figure 1.27, which depicts how the primary and secondary equatorial lengths s_1 and s_2 change with respect to the sample center

x_0 as a positive height displacement (corresponding to a negative displacement error in Topas) is induced. From the figure, it is apparent that the new primary irradiated equatorial length s_1' is longer:

$$s_1' = s_1 + |x_- - x_-'| \qquad \text{Eq. 38}$$

At the same time, the new irradiated equatorial length on the secondary side of the sample shortens:

$$s_2' = s_2 - |x_+ - x_+'| \qquad \text{Eq. 39}$$

From trigonometry,

$$|x_- - x_-'| = \frac{h}{tan\left(\theta + {}^{\varphi}/_{2}\right)} \qquad \text{Eq. 40}$$

$$|x_+ - x_+'| = \frac{h}{tan\left(\theta - {}^{\varphi}/_{2}\right)} \qquad \text{Eq. 41}$$

Combining these last four equations gives expressions for the vertically displaced primary and secondary irradiated lengths:

$$s_1' = s_1 + \frac{h}{\tan\left(\theta + {}^{\varphi}/_{2}\right)} \qquad \text{Eq. 42}$$

$$s_2' = s_2 - \frac{h}{\tan\left(\theta - {}^{\varphi}/_{2}\right)} \qquad \text{Eq. 43}$$

Substituting in the expressions for s_1 and s_2 given in Eq. 36 and Eq. 37 leads to Eq. 18 and Eq. 19 given in the main text.

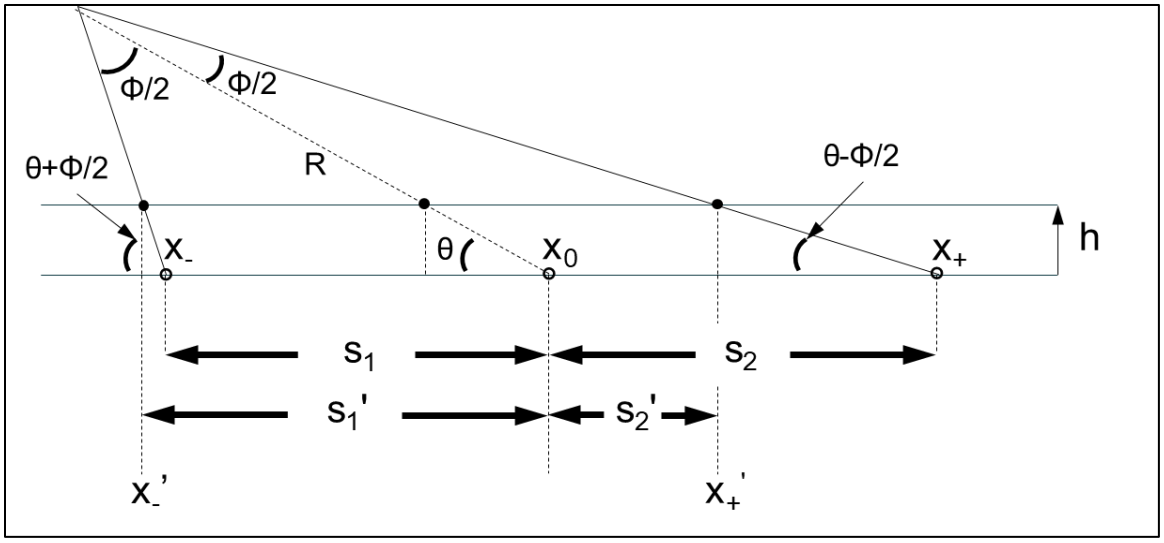

Figure 1.27. Trigonometric relationships of beam spill with a height displacement *h*.

Derivation of the irradiated sample area (without displacement error)

Figure 1.28 shows three separate cases of increasing θ for which the illuminated sample area must be calculated. In case 1, the illuminated sample area equals the entire sample area. In case 2, the illuminated sample area equals the entire sample area minus the area of the circular segment on the secondary side of the sample. In case 3, the illuminated sample area equals the entire sample area minus the areas of the circular segments on both the primary and secondary sides of the sample.

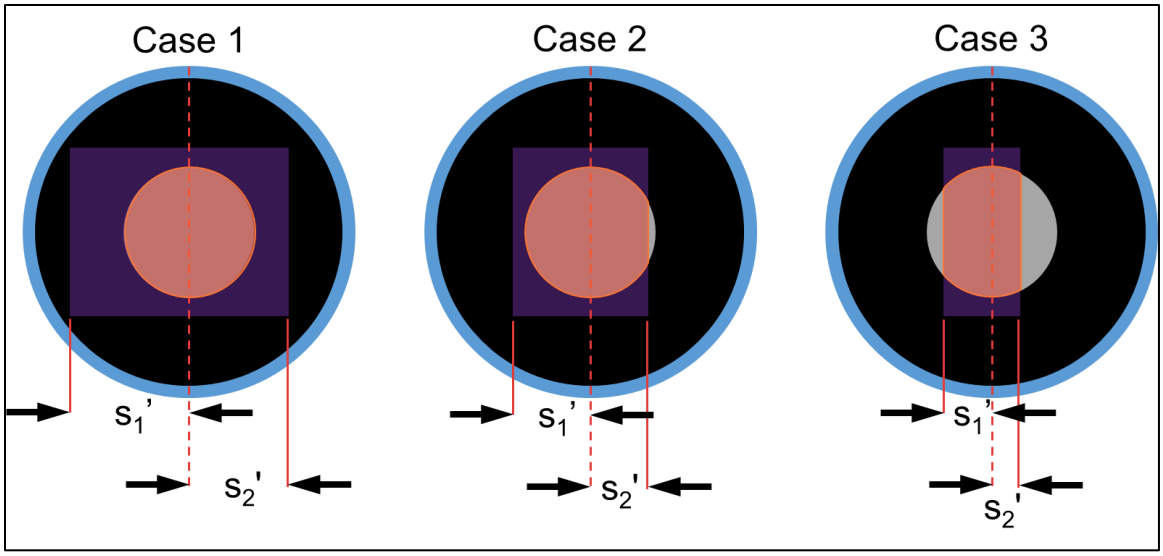

Figure 1.28. Illuminated sample area (orange) as a function of x-ray incident angle when a positive displacement error exists.

Trigonometric Derivation

The area of the primary circular segment can be expressed using the sample radius *d* and the displacement-dependent length s_1':

$$A_1 = d^2 cos^{-1}\left(\frac{s_1'}{d}\right) - s_1'\sqrt{d^2 - s_1'^2} \qquad \text{Eq. 44}$$

Similarly, the secondary circular segment is given by:

$$A_2 = d^2 cos^{-1}\left(\frac{s_2'}{d}\right) - s_2'\sqrt{d^2 - s_2'^2} \qquad \text{Eq. 45}$$

We may now examine each of the three cases individually. For case 1, the illuminated sample area is simply the total area of the sample:

$$S_{2D} = \pi d^2 \qquad \text{Eq. 46}$$

For case 2, the illuminated sample area is the total area of the sample minus A_2:

$$S_{2D} = \pi d^2 - d^2 cos^{-1}\left(\frac{{s_2}'}{d}\right) - {s_2}'\sqrt{d^2 - {s_2}'^2} \quad \text{Eq. 47}$$

For case 3, the irradiated sample area S_{2D} is equal to the total sample area minus A_1 and A_2:

$$S_{2D} = \pi d^2 - d^2 cos^{-1}\left(\frac{{s_1}'}{d}\right) + s_1'\sqrt{d^2 - {s_1}'^2} - d^2 cos^{-1}\left(\frac{{s_2}'}{d}\right) + {s_2}'\sqrt{d^2 - {s_2}'^2} \quad \text{Eq. 48}$$

Now, let s_1' and s_2' be replaced by d whenever d is the smaller value. For case 2, d is smaller than s_1':

$$S_{2D} = \pi d^2 - d^2 cos^{-1}\left(\frac{d}{d}\right) + s_1'\sqrt{d^2 - d^2} - d^2 cos^{-1}\left(\frac{{s_2}'}{d}\right) + {s_2}'\sqrt{d^2 - {s_2}'^2} \quad \text{Eq. 49}$$

Note that for this case, the second and third terms of Eq. 49 drop out and results in Eq. 47. Similarly, for case 3, d is smaller than both s_1' and s_2':

$$S_{2D} = \pi d^2 - d^2 cos^{-1}\left(\frac{d}{d}\right) + s_1'\sqrt{d^2 - d^2} - d^2 cos^{-1}\left(\frac{d}{d}\right) + {s_2}'\sqrt{d^2 - d^2} \quad \text{Eq. 50}$$

In this case only the first term is left, resulting in Eq. 46.

Eq. 48 can be simplified as follows:

$$S_{2D} = \frac{\pi d^2}{2} - d^2 cos^{-1}\left(\frac{{s_1}'}{d}\right) + s_1'\sqrt{d^2 - {s_1}'^2} + \frac{\pi d^2}{2} - d^2 cos^{-1}\left(\frac{{s_2}'}{d}\right) + {s_2}'\sqrt{d^2 - {s_2}'^2} \quad \text{Eq. 51}$$

$$S_{2D} = d^2\left(\frac{\pi}{2} - cos^{-1}\left(\frac{{s_1}'}{d}\right)\right) + s_1'\sqrt{d^2 - {s_1}'^2} + d^2\left(\frac{\pi}{2} - cos^{-1}\left(\frac{{s_2}'}{d}\right)\right) + {s_2}'\sqrt{d^2 - {s_2}'^2} \quad \text{Eq. 52}$$

We can now make use of the following identity:

$$sin^{-1}x + cos^{-1}x = \frac{\pi}{2} \rightarrow sin^{-1}x = \frac{\pi}{2} - cos^{-1} \quad \text{Eq. 53}$$

Eq. 52 becomes:

$$S_{2D} = d^2 sin^{-1}\left(\frac{{s_1}'}{d}\right) + s_1'\sqrt{d^2 - {s_1}'^2} + d^2 sin^{-1}\left(\frac{{s_2}'}{d}\right) + {s_2}'\sqrt{d^2 - {s_2}'^2} \quad \text{Eq. 54}$$

The final expression given in Eq. 20 is obtained by replacing s_1' with s_{m1} (the smaller of s_1' and d) and by replacing s_2' with s_{m2} (the smaller of s_2' and d). As discussed earlier, making this substitution allows the same expression to be used for all three of the cases depicted in Figure 1.28.

$$S_{2D} = d^2 sin^{-1}\left(\frac{s_{m1}}{d}\right) + s_{m1}\sqrt{d^2 - {s_{m1}}^2} + d^2 sin^{-1}\left(\frac{s_{m2}}{d}\right) + s_{m2}\sqrt{d^2 - {s_{m2}}^2} \quad \text{Eq. 55}$$

Topas Code Changes

Jeremiah Lipp, Spring 2020, FHI and UofSC

Absorption Edge Macro fix in GUI

Description: This bug is present in both TOPAS version 5 and version 6. When using the absorption edge macro available in the GUI (under the emission profile section), the bug will erase the value back to some default value every time the program is opened new. The code is fixed by changing a single word.

Original Code

```
macro Absorption_Edge_Correction(
  max_lam,
  cedge,      vedge,
  ca_white,   va_white,
  cb_white,   vb_white,
  ca_erf,     va_erf,
  cedge_extra, vedge_extra)
{
        absorption_edge Fix_If_Eqn(cedge, vedge)
                edge_max_lam max_lam
                a_white Fix_If_Eqn(ca_white, va_white)
                b_white Fix_If_Eqn(cb_white, vb_white)
                a_erf Fix_If_Eqn(ca_erf, va_erf)
                edge_extra Fix_If_Eqn(cedge_scale, vedge_extra)
}
```

Updated Code

```
macro Absorption_Edge_Correction(
  max_lam,
  cedge,      vedge,
  ca_white,   va_white,
  cb_white,   vb_white,
  ca_erf,     va_erf,
  cedge_extra, vedge_extra)
{
        absorption_edge Fix_If_Eqn(cedge, vedge)
                edge_max_lam max_lam
                a_white Fix_If_Eqn(ca_white, va_white)
                b_white Fix_If_Eqn(cb_white, vb_white)
```

```
                    a_erf Fix_If_Eqn(ca_erf, va_erf)
                    edge_extra Fix_If_Eqn(cedge_extra, vedge_extra)
}
```

LP_Factor_X Macro Bug

Description: This bug (present in both TOPAS version 5 and version 6) in the LP_Factor_X macro (used originally only in Launch mode to perform LP factor scaling point by point) was identified by a user. The bug and fix by Alan Coelho is discussed in rowlesmr and AlanCoelho [60]

Original Code

```
macro LP_Factor_X(v) { LP_Factor_X(,v) }
macro LP_Factor_X(c, v)
  {
    #m_argu c
    If_Prm_Eqn_Rpt(c, v, min .0001 max 90)
    local #m_unique th = X Pi / 360;
    scale_phase_X = (1 + Cos(c Deg)^2 Cos(2 th)^2) / (Sin(th) Cos(th));
    scale_pks = 1 / Sin(Th);
  }
```

Updated Code

```
macro LP_Factor_X(v) { LP_Factor_X(,v) }
macro LP_Factor_X(c, v)
  {
    #m_argu c
    If_Prm_Eqn_Rpt(c, v, min .0001 max 90)
    local #m_unique th = X Pi / 360;
    scale_phase_X = (1 + Cos(c Deg)^2 Cos(2 th)^2) / (Sin(th)^2 Cos(th));
  }
```

Point by point scaling of LP Factor in GUI

Description: with broad peaks, all intensity scaling should be done point by point. LP scaling in particular makes a large difference, and will shift the positions

of broad peaks significantly (depending on the peak position). At low angles the effect of this peak pulling can be over two degrees.

Original Code

```
macro LP_Factor(v) { LP_Factor(,v) }
macro LP_Factor(c, v)
  {
    #m_argu c
    If_Prm_Eqn_Rpt(c, v, min .0001 max 90)
    scale_pks = (1 + Cos(CeV(c,v) Deg)^2 Cos(2 Th)^2) / (Sin(Th)^2 Cos(Th));
  }
```

Updated Code

```
macro LP_Factor(v) { LP_Factor(,v) }
macro LP_Factor(c, v)
{
        #m_argu c
         If_Prm_Eqn_Rpt(c, v, min .0001 max 90)
        local #m_unique th = X Pi / 360; 'This line entered to convert th to X so that scale_phase_X can be
used
        scale_phase_X = (1 + Cos(c Deg)^2 Cos(2 th)^2) / (Sin(th)^2 Cos(th));
}
```

Point by point scaling of peaks due to absorption in GUI

Description: two macros are associated with scaling of peaks due to absorption. However, the first macro (macro Absorption_With_Sample_Thickness_mm_Intensity(u,uv,d,dv) does not seem to do anything. Still, we have changed it for thoroughness's sake.

Original Code

```
macro Absorption_With_Sample_Thickness_mm_Intensity(u, uv, d, dv)
  {
    #m_argu u
    #m_argu d
    #m_ifarg u ""
      #m_unique_not_refine u
```

```
    #m_endif
    scale_pks = (1 - Exp(-.2 CeV(u, uv) CeV(d, dv) / Sin(Th)));
  }
macro Absorption_With_Sample_Thickness_mm_Shape_Intensity(u, uv, d, dv)
  {
    #m_argu u
    #m_argu d
    #m_ifarg u ""
      #m_unique_not_refine u
    #m_endif
    Absorption_With_Sample_Thickness_mm_Shape(u, uv, d, dv)
    scale_pks = (1 - Exp(-.2 CeV(u, uv) CeV(d, dv) / Sin(Th)));
  }
```

Updated code

```
macro Absorption_With_Sample_Thickness_mm_Intensity(u, uv, d, dv)'Modified to allow point by point scaling of peaks for absorption
{
  #m_argu u
  #m_argu d
          #m_ifarg u ""
    #m_unique_not_refine u
  #m_endif
                    local #m_unique th = X Pi / 360;          'This line entered new to convert th to X so that scale_phase_X can be used, as for LP_Factor_X macro
                    scale_phase_X = (1 - Exp(-.2 CeV(u, uv) CeV(d, dv) / Sin(th)));          'This is the new code
'                   scale_pks = (1 - Exp(-.2 CeV(u, uv) CeV(d, dv) / Sin(Th)));    'This is the original line of code, commented out
}
macro Absorption_With_Sample_Thickness_mm_Shape_Intensity(u, uv, d, dv)    'This macro modified to allow point by point scaling of peaks for absorption
{
  #m_argu u
  #m_argu d
  #m_ifarg u ""
    #m_unique_not_refine u
  #m_endif
          Absorption_With_Sample_Thickness_mm_Shape(u, uv, d, dv)
                    local #m_unique th = X Pi / 360;          'This line entered new to convert th to X so that scale_phase_X can be used, as for LP_Factor_X macro
                    scale_phase_X = (1 - Exp(-.2 CeV(u, uv) CeV(d, dv) / Sin(th)));          'This is the new code
'           scale_pks = (1 - Exp(-.2 CeV(u, uv) CeV(d, dv) / Sin(Th)));    'This is the original line of code, commented out
```

```
}
```

2D approximation and point by point scaling of peaks due to beam spill in GUI

Description: this is the most extensively modified piece of code. Not only does it scale the beam spill macro point by point, but it also introduces a more thorough calculation to adjust the intensity for beam spill with our zero-background holders. It includes an adjustment for height error. However, the adjustment for height error requires that the value for height error be entered into the code by hand – the value will not refine.

Original code

```
macro Divergence_Sample_Length(c, v, slc, slv)
  {
    #m_argu c
    #m_argu slc
    If_Prm_Eqn_Rpt(c, v, min 0.0001 max = 2 Val + .1;, del = 0.01 Val + .001;)
    If_Prm_Eqn_Rpt(slc, slv, min 0.0001 max = 2 Val + 1;, del = 0.01 Val + .01;)
    one_on_x_conv = - Min(CeV(c,v), Rad Sin(Th) CeV(slc, slv)/Rs)^2  Deg_on_2 / Tan(Th);
    scale_pks = Min(CeV(c,v), Rad Sin(Th) CeV(slc, slv)/Rs) / CeV(c,v);
  }
```

Updated Code:

```
macro Divergence_Sample_Length(c, v, slc, slv)  'modified to scale peaks point by point when using "Point
detector" model for equatorial convolutions, further modified to do a more accurate beam spill approximation for
a negative sample displacement parameter only
{
        #m_argu c
        #m_argu slc
  If_Prm_Eqn_Rpt(c, v, min 0.0001 max = 2 Val + .1;, del = 0.01 Val + .001;)
  If_Prm_Eqn_Rpt(slc, slv, min 0.0001 max = 2 Val + 1;, del = 0.01 Val + .01;)
        one_on_x_conv = - Min(CeV(c,v), Rad Sin(Th) CeV(slc, slv)/Rs)^2  Deg_on_2 / Tan(Th);  'This is
original code - one_on_x_conv is a convolution for equatorial divergence. See page 170 of the technical
reference.
        local !th = X Pi / 360;                         'This line entered new to convert X to th so that
scale_phase_X can be used, as for LP_Factor_X macro
```

```
	local !h = 0.2;	'This line defines locally the displacement parameter (magnitude of the negative sample displacement parameter). For now, this parameter must be entered into the TOPAS.inc file here (the macro does not receive it from the GUI)

	local !soller = 5*Pi / 180;	'This line defines locally the soller slit width used for calculating the axial beam length on the sample. For now, this parameter must be entered here.

	local !phi = CV(c,v)/2;	'This line is to reduce code length and help overcome an error

	local !sa = Rs*Sin(phi) / Sin(th + phi) + h / Tan(th + phi);	'Defines s1 parameter: physically this is the equatorial length of the illuminated sample on the beam side of the sample

	local !sb = Rs*Sin(phi) / Sin(th - phi) - h / Tan(th - phi);	'Defines s2 parameter: physically this is the equatorial length of the illuminated sample on the detector side of the sample

	local !beam = 2*Rs*Tan(soller / 2)*(sa + sb);	'Calculates the total irradiated area of the beam on the plane containing the surface of the sample

	local !d = CeV(slc, slv)/2;	'Defines the sample radius as a local parameter

	local !samin = Min(d, sa);	'Choses the minimum of the sample radius or s1 parameter

	local !sbmin = Min(d, sb);	'Choses the minimum of the sample radius or s2 parameter

	local !sample = d^2*ArcSin(samin / d) + samin*Sqrt(d^2 - samin^2) + d^2*ArcSin(sbmin / d) + sbmin*Sqrt(d^2 - sbmin^2);	'Calculates the irradiated sample area. Note how the terms simplify to give the sample area if s1 and s2 are both larger than d.

	scale_phase_X = sample / beam;	'This final line of code scales all peaks point by point, using a scaling factor of the illuminated sample area divided by the total area of the beam in the sample plane

'	scale_phase_X = Min(CeV(c,v), Rad Sin(th) CeV(slc, slv)/Rs) / CeV(c,v); 'This is newer scaling code for the old scaling point by point, but commented out for the finer approximation

'	scale_pks = Min(CeV(c,v), Rad Sin(Th) CeV(slc, slv)/Rs) / CeV(c,v);	'This is the original code for scaling

}
```

Surface Roughness: point by point scaling in GUI:

Description: this is for the surface roughness macro by Pitschke et al. All intensity factors used should be scaled point by point.

Original Code:

```
macro Surface_Roughness_Pitschke_et_al(a1c, a1v, a2c, a2v)
  {
    #m_argu a1c
    #m_argu a2c
    If_Prm_Eqn_Rpt(a1c, a1v, min .0001 max 1)
    If_Prm_Eqn_Rpt(a2c, a2v, min .0001 max 1)
    scale_pks = (1 - CeV(a1c, a1v) (1 / Sin(Th) - CeV(a2c, a2v) / Sin(Th)^2)) / (1 - CeV(a1c, a1v) + CeV(a1c, a1v) CeV(a2c, a2v));
  }
```

Updated Code:

```
macro Surface_Roughness_Pitschke_et_al(a1c, a1v, a2c, a2v)
  {
    #m_argu a1c
    #m_argu a2c
    If_Prm_Eqn_Rpt(a1c, a1v, min .0001 max 1)
    If_Prm_Eqn_Rpt(a2c, a2v, min .0001 max 1)
    local #m_unique th = X Pi / 360; 'This line entered new to convert th to X so that scale_phase_X can be used, as for LP_Factor_X macro
    scale_phase_X = (1 - CeV(a1c, a1v) (1 / Sin(th) - CeV(a2c, a2v) / Sin(th)^2)) / (1 - CeV(a1c, a1v) + CeV(a1c, a1v) CeV(a2c, a2v)); 'This is the new code
    'scale_pks = (1 - CeV(a1c, a1v) (1 / Sin(Th) - CeV(a2c, a2v) / Sin(Th)^2)) / (1 - CeV(a1c, a1v) + CeV(a1c, a1v) CeV(a2c, a2v)); 'This is the original line of code, commented out
  }
```

Additional Figures

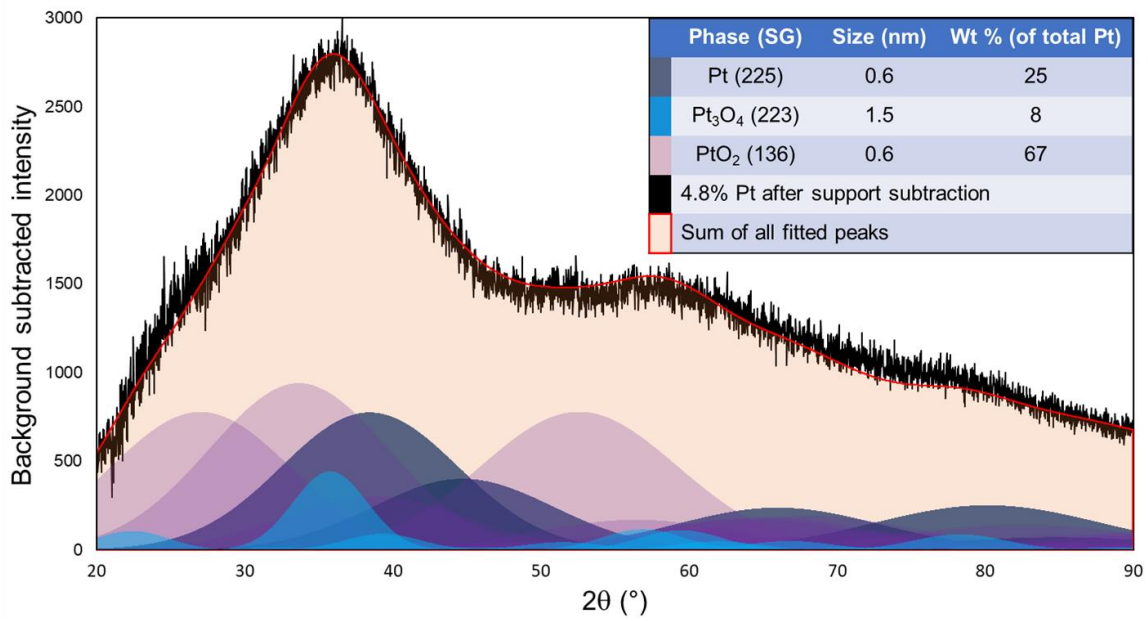

Figure 1.29. 4.8% Pt / SiO_2 deconvolution after analysis using Topas. The shown fit includes corrections for Lorentz-polarization, beam spill, absorption, and finite thickness. The only refined parameters in the shown fit are the crystallite Gaussian size and overall scale factor for each phase, as well as two surface roughness parameters.

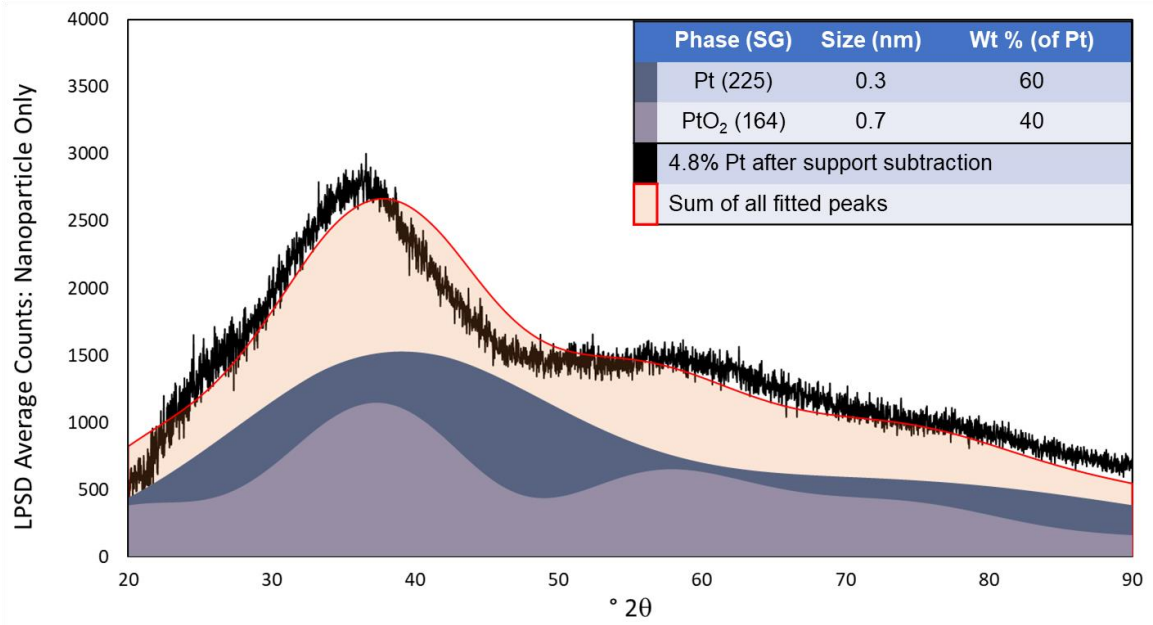

Figure 1.30. 4.8% Pt / SiO_2 fit with α-PtO_2. The shown fit includes corrections for Lorentz-polarization, beam spill, absorption, and finite thickness. There are seven refined parameters: scale and Gaussian size for each phase, Pt L.P (=3.775), and two terms for surface roughness.

CHAPTER 2

WHEN NOBLE METALS AREN'T SO NOBLE: AMBIENT OXIDATION OF ULTRASMALL NANOPARTICLES[2]

[2] Lipp, J., Banerjee, R., Patra, N., Patwary, M. D. F., Dong, A., Bare, S. R., and Regalbuto, J. R. To be submitted.

Abstract

In our previous work (Lipp, et al. [61]) we developed a method for characterizing supported crystalline nanoclusters with benchtop x-ray diffraction via Rietveld analysis. Now we apply this method to investigate a series of noble metals supported on an amorphous silica for room temperature oxidation. Pt, Pd, Ir, Rh, Ru, and Au with sizes < 2nm are all examined with benchtop x-ray diffraction under ambient conditions. It is found that Pt, Pd, Ir, and Rh are mostly oxidized, with the remaining metal exhibiting lattice parameter dilation as compared with the bulk. Ru appears to exist only as oxides, while Au does not show any evidence of oxidation and exhibits lattice parameter contraction. The results for Pt are corroborated with XAS and extended to examine oxidation rates in-situ.

Introduction

Since catalytic reactions depend on the physical and chemical properties of the catalysts, it is important to accurately characterize those properties for a given set of reaction conditions. This is particularly important for nanoparticle catalysts, since small particle sizes have been shown to dramatically affect properties such as lattice parameter and even physical state as compared to bulk values. The importance of characterizing small nanoparticles is paralleled by the difficulty in doing so. The affinity for nanoparticles to change properties depending on their environment dictates the use of in-situ techniques; characterization methods are needed that can probe nano-catalysts in their “home” environments (such as ambient and reaction conditions) with sufficient resolution to discern useful information.

Among the more difficult nanoparticle systems to characterize are mixed metal / metal oxides. Oxygen has a low contrast in electron microscopy, this makes characterization of whatever oxide phases are not reduced in the reducing environment of the high vacuum and electron beam difficult. In x-ray diffraction (XRD), oxide phases typically have lower symmetry, resulting in complicated diffraction patterns consisting of multiple peaks that are merged together by extensive broadening as crystallite sizes decrease below 3 nm. Beamline techniques such as x-ray absorption spectroscopy (XAS) can provide useful information; however, access to synchrotrons is limited and the analyses are greatly benefited by constraints identified independently by other methods.

These difficulties in characterization make it difficult to rigorously explore fundamental nanoparticle size-effects, such as the propensity for noble metals to oxidize under ambient conditions. This is a critically important factor for any chemical reactions that utilize catalysts containing “ultrasmall” crystallites, since traditional drying and/or storage of noble metal nanoparticles in air or even a brief transfer of the catalysts from reduction furnace to reactor can result in completely oxidized catalyst surfaces. Researchers who are unaware of the possible oxidation of their catalysts may inadvertently design ineffective reactions or misinterpret experimental results.

Because of the difficulty in characterizing ambient oxidation of ultra-small noble metal nanoparticles, documentation in the literature consists of mostly stand-alone observations, usually for a single metal (Table 2.1). A myriad of characterization methods has been used to document the oxidation: nuclear

magnetic resonance (NMR), XAS, XRD, surface-enhanced Raman spectroscopy (SERS), electron microscopy such as scanning transmission electron microscopy (STEM), and x-ray photoelectron spectroscopy (XPS). The latter two methods operate under an ultra-high vacuum which is known to be a reducing environment; samples characterized under these conditions may therefore not be oxidized to the same extent as under ambient conditions. Characterization methods employing ambient pressures have been employed to characterize the room temperature oxidation of Pt, Pd, Rh, Ru, and Au nanoparticles. To the best of our knowledge, there is no prior published work that examines room temperature oxidation of Ir nanoparticles with an ambient-pressure characterization method, though ambient pressure thin-film characterization has been made via SERS. Also to the best of our knowledge, Rh and Ru nanoparticles with volume-weighted sizes (D_V) less than 2nm have not yet been examined for room temperature oxidation; room temperature Pd with 1.7nm D_V has been ambiently characterized with x-ray absorption near edge structure (XANES), but not extended x-ray absorption fine structure (EXAFS) (which gives clues to atom bonding environments and lattice parameter). This is important, since oxidation of these metals has been shown to depend upon the particle size, temperature, and environment.

We present a systematic, comprehensive study of ultrasmall noble metal (Pt, Pd, Ir, Rh, Ru, and Au) nanoparticles using the same benchtop instrument at the same conditions. We have produced a consistent set of results suggesting oxide shell-metal core hemispheres (except Au, which did not appear to oxidize) with lattice expansion of metal cores caused by the oxide shell.

Literature Review: Room temperature oxidation of noble metals

It is useful to review instances of room temperature noble metal (Pt, Pd, Ir, Rh, Ru, Au) oxidation that have been documented throughout literature and compare the findings with particle sizes and the methods / environments used for the characterization (Table 2.1). The instances reviewed herein take place as early as the 1980s and will now be briefly summarized in chronological order.

1980s: While characterizing the ^{195}Pt NMR line shapes of 10% Pt / Al_2O_3 samples (1.6nm, estimated from STEM surface-weighted dispersion), Rhodes, et al. [62] noticed that samples exposed to air for long periods of time gave a different profile than when they were cleaned of adsorbates (reduced in H_2 at 300°C) and exposed to air in-situ. They concluded that the surface of the particles was reconstructing into $Pt(OH)_6$, since $H_2Pt(OH)_6$ gave the same ^{195}Pt NMR line position as the long-term air-exposed samples (1.089 kG / MHz). Martens, et al. [63] used EXAFS to examine the in-situ low-temperature oxidation of a 1.9% Rh / Al_2O_3 sample with an estimated particle size of around 2.5 nm. They concluded that an oxide shell (assumed to be Rh_2O_3) formed around the metallic core, with 25-35% oxidation at 100K, and around 60% oxidation at 300K. Bucher, et al. [29] observed - for a 5.7% Pt / SiO_2 sample that was passivated in O_2 immediately after preparation - the same NMR peak at 1.089 G / kHz as that reported in Rhodes, et al. [62]. The authors showed that 10μm particles of a PtO_2 reference give an NMR peak centered at 1.089 G / kHz; this suggests that the identification of the oxide phase as $Pt(OH)_6$ by Rhodes, et al. [62] might be attributed to PtO_2.

1990s: In a pioneering work with an in-situ laboratory transmission XRD, Gnutzmann and Vogel [10] examined the oxidation and reduction of a standard Pt catalyst (EuroPt-1, 6.3% Pt / SiO_2, 1.6nm D_V). They accounted for x-ray absorption in the support subtraction and used Debye Function Analysis (DFA) to deconvolute oxide peaks from the metal; however, their support subtraction appears to be flawed. Tong and van der Klink [64] performed a similar ^{195}Pt NMR study to that of Rhodes, et al. [62] on a 4.4% Pt / TiO2 catalyst (TEM surface-weighted particle size of 1.7nm), but with careful reduction prior to exposing the samples to varying pressures of O_2 for 120 hours. They concluded that no bulk oxides form, and cited the conclusion of Rhodes, et al. [62] that either H_2 or water must be involved for the formation of bulk peaks. Chan, et al. [65] used in-situ surface-enhanced Raman spectroscopy (SERS) to characterize the oxidation of Pt, Pd, Ir, Rh, and Ru thin films. They observed that air-exposed room temperature samples of Ir, Rh, and Ru exhibited oxide peaks, but fully reduced films exposed to dry O_2 did not oxidize until elevated temperatures. The authors concluded that water may facilitate the room temperature oxidation. Saliba, et al. [66] demonstrated that the bulk Pt(111) surface could be oxidized at room temperature under UHV conditions in the presence of ozone. At low surface coverages single oxygen atoms adsorbed onto the surface and at high surface coverages PtO_x particles formed. The authors noted that Au was the hardest of the noble metals to oxidize and suggested based on previous results (Saliba, et al. [67]) that even Au could be oxidized at room temperature in the presence of ozone.

2000-2005: In a follow up to the work by Chan, et al. [65], Luo, et al. [68] specifically investigated Pd, Ir, Rh, and Ru thin films for the effect of humidity on oxidation. They found that Ir, Rh, and Ru (and Pd to a lesser extent) would form oxides at room temperature only if the conditions were such that a water film could form on the surface. The authors gave evidence for an electrochemical mechanism driven by a change in surface potential caused by O_2 electroreduction. Le Rhun, et al. [69] used a Siemens D5005 laboratory diffractometer to characterize Ru nanoparticles. The authors noted that samples exposed to air only for a few hours showed signs of oxidation; air-exposure for forty days let to what appears to be near-complete oxidation. The authors were able to simply fit the XRD patterns with Ru and RuO_2 (rutile, i.e. space group 136), but Rietveld refinements failed and the authors called for a more rigorous analysis. In a follow-up study to Le Rhun, et al. [69], Vogel, et al. [11] used an in-situ laboratory XRD with DFA to confirm that the Ru nanoparticles fully oxidized after long-term storage in air; the exact oxidation / reduction properties depended on the synthesis method; xylitol-prepared nanoparticles could be roughly fit with rutile RuO_2, 1,2-dichlorobenzene-prepared nanoparticles were classified as amorphous Ru_xO_y. After reduction, the authors calcined the particles in-situ and found that the smaller particles (2nm) could be oxidized (at high T), but large particles (8nm) remained reduced. Yang, et al. [70] characterized 8% Pt / SBA-15 NPs with XAS, XRD, and TEM. The characterization showed NPs that were 2.0 nm (TEM) / 2.3nm (XRD) large; in-situ XAS showed oxidation after exposure to air, though more details were not provided.

2006-2010: Miller, et al. [2] prepared a multitude of supported Au catalysts and used EXAFS to correlate their Au-Au bond length to particle size (smaller reduced particles showed contracted Au-Au bond lengths). The authors noticed that the smallest particles showed signs of oxidation under flowing air, up to a maximum of 10% oxidation to Au^{III} oxide. Vogel [12] characterized Pt/C and Pt:Ru/C commercial catalysts with in-situ X-ray diffraction. Recognizing that, "A considerable amount of surface oxide is usually formed at [sic] highly dispersed metallic catalysts even after short storage in air", Vogel reduced the catalysts in-situ and estimated the pre-reduced oxide quantity to be around 12% for the Pt/C catalyst and 25% for the PtRu/C catalyst. Rzeszotarski and Kaszkur [71] examined 10% Pt / SiO_2 nanoparticles with an in-situ XRD setup under cycling H_2, He, O_2, He, … environments and observed the corresponding contractions/expansions of the "apparent [Pt] lattice parameter." Though the particles were larger (3.1 nm) than those of other studies, and though the authors only claim chemisorbed oxygen, the apparent expansion of the lattice parameter under room temperature O_2 could be indicative of oxide formation, and the overall results provide interesting evidence of environmentally induced changes in bond length. Ingham, et al. [72] use in-situ synchrotron XRD and x-ray absorption near edge structure (XANES) to examine a series of Pd / SiN catalysts with varying particle sizes. The authors confirm with XANES that the air-exposed nanoparticles are partly oxidized and use XRD to correlate the oxidation with an expanded lattice parameter that is a function of decreasing particle size.

2011-2015: Herd, et al. [73] give clues to possible mechanisms for room temperature Ru oxidation by showing that a bulk single crystal surface of Ru(0001) forms Ru-O surface clusters at room temperature in the presence of atomic oxygen. The authors are unable to identify the exact stoichiometry of the Ru-O clusters and believe that the visible clusters (typical height 0.5 nm and typical width 4 nm) are made up of aggregates of smaller Ru-O precursors. Gallagher, et al. [3] investigated a series of three supported Pt catalysts with synchrotron techniques and found that the extent of room temperature air oxidation increased with decreasing particle size. The authors documented a size-dependent Pt lattice parameter contraction for reduced particles and noted via XRD an apparent lattice expansion for the oxidized sample with the largest particles (they were unable to analyze the smaller air-oxidized samples with XRD). The authors also observed with XRD that the smallest air-oxidized particles could be reduced at room temperature after just two minutes of exposure to H_2. Bhattacharya, et al. [74] claimed with TEM and XPS that a suspension of dendrimer encapsulated Ru nanoparticles in DI water oxidized to RuO_2 during brief exposure of the suspension to air. Based on the ability of Ru nanoparticles to oxidize in UHV by Bavand, et al. [75] and the increased propensity of Ru to oxidize with a water film (Chan, et al. [65], Luo, et al. [68]), we hypothesize that the oxidation observed by Bhattacharya, et al. [74] may have occurred as the nanoparticles were dried in a low O_2 environment (<0.2ppm O_2).

2016-2021: Banerjee, et al. [30] synthesized a series of Pt catalysts on carbon and silica supports using the strong electrostatic adsorption (SEA) method to make

particles with tight size distributions and characterized the samples using a benchtop XRD equipped with a high sensitivity silicon strip linear position sensitive detector (LPSD). The authors were able to observe room temperature oxidation on all the catalysts - tentatively identifying the oxide phase as Pt_3O_4, though they admitted the background subtraction method was flawed and the second strongest line of the Pt_3O_4 structure was missing from their diffractograms. A corroboration with fast Fourier transform (FFT) analysis on 70 of the particles yielded a quantifiable statement as to the particle size effect on ambient oxidation (for an activated carbon support): “below 1.5 nm, nanoparticles exist only in the oxide phase; in the range of 1.6 to 2.7 nm, they exist as a combination of metal and oxide, and above 2.8 nm, are all metallic.” Qin, et al. [76] prepared Ir catalysts on a carbon support and ceria / carbon hybrid support using the ethylene glycol method; the authors observed oxide on the catalysts using XPS and claim air exposure as the cause. We note that their synthesis involves washing the catalysts with DI water before drying in air, which may help facilitate the formation of oxides. In a following study to Banerjee, et al. [30], Banerjee, et al. [77] prepared a series of Pt nanoparticles on carbon supports to investigate the effect of carbon pore size on Pt particle size and resistance to oxidation. They found that the resistance of nanoparticles to ambient oxidation was strictly a function of particle size, again documenting that the extent of oxidation was a particle size effect. Ye, et al. [78] used the difference between the surface oxidation and reduced core of Pt and Pd to separate the structures of the two using EXAFS scans of ambiently oxidized vs. reduced particles.

Table 2.1. Review of literature documenting noble metal oxidation at room temperature. XRD methods are differentiated by x-ray source. All particle sizes were measured by electron microscopy unless noted otherwise; particle sizes are presented as the number-weighted average (D_N) followed by the volume-weighted average (D_V) unless noted otherwise; D_S = surface-weighted average; NR = not reported. SLS = synchrotron light source, vac = vacuum, C = carbon, CX = carbon xerogel.

Reference	Year	% Metal / Support	Size [nm] D_N , D_V	Oxidative Environment	Characterization Method / Environment	Oxide Phase
Rhodes, et al. [62]	1982	10% Pt / Al_2O_3	NR, 1.6 (D_S)	Air, lab	NMR / air or vac	$Pt(OH)_6$*
Martens, et al. [63]	1989	1.9% Rh / Al_2O_3	NR, 2.5 (EXAFS)	O_2, 0.1atm	In-situ EXAFS / O_2, 100 K, 300K	Rh_2O_3
Bucher, et al. [29]	1989	5.7% Pt / SiO_2	NR, 1.7 (D_S)	Air, lab	NMR / NR / 20K	PtO_2
Gnutzmann and Vogel [10]	1990	6.3% Pt / SiO_2	1.3, 1.6 (XRD)	Air, transport	In-situ **XRD (lab)** / 10^{-3} mbar	PtO, Pt_3O_4
Tong and van der Klink [64]	1995	4.4% Pt / TiO_2	NR, 1.7 (D_S)	O_2 dosing	NMR / He (400 Torr), 80K	No bulk oxide
Chan, et al. [65]	1999	Ir / Au foil Rh / Au foil Ru / Au foil	1nm film	Wet, in air	In-situ SERS	NR
Saliba, et al. [66]	1999	Pt(111)	Bulk	Ozone, UHV	TPD / UHV AES / UHV LEED / UHV	PtO_x
Luo, et al. [68]	2000	Pd / Au foil Rh / Au foil Ru / Au foil Ir / Au foil	1 nm film	Wet, in air; $H_2O+O_2+N_2$	In-situ SERS	PdO** Rh_2O_3 RuO_2 NR
Le Rhun, et al. [69]	2000	100% Ru	NR, NR	Air, lab	**XRD (lab)** / Air	RuO_2 (136)
Vogel, et al. [11]	2001	100% Ru	NR, ~2 (XRD)	Air, lab, O_2	In-situ **XRD (lab)** air / 100% O_2, 200°C	RuO_2 (136) / amorphous Ru_xO_y
Yang, et al. [70]	2003	8% Pt / SBA-15	2.0, NR (TEM) NR, 2.3 (XRD)	Air, lab	In-situ XAS / air	NR
Miller, et al. [2]	2006	0.9% Au / Al_2O_3 0.6% Au / Al_2O_3 1.3% Au / Al_2O_3 2.9% Au / TiO_2	NR, 4 (D_S, EXAFS) NR, 1 (D_S, EXAFS) NR, 1 (D_S, EXAFS) NR, 3 (D_S, EXAFS)	Flowing air	In-situ XAS / air	Au^{III} oxide
Vogel [12]	2008	20% Pt / C 20% Pt-Ru / C	2.3, 3.1 (XRD) NR, 2.7 (XRD)	Air, lab	In-situ **XRD(lab)** / Air	PtO_x amorphous RuO_x

Ingham, et al. [72]	2010	Pd / SiN	NR, 6.1 (XRD) NR, 3.0 (XRD) NR, 1.7 (XRD)	Air, transport & lab	In-situ **XRD(SLS)** / UHV In-situ XAS / Air	PdO
Herd, et al. [73]	2013	Ru (0001) surface	Bulk	Atomic oxygen, 300 K	STM / UHV XPS / UHV	Ru-O, unknown stoichiometry
Gallagher, et al. [3]	2014	2.8% Pt / Al_2O_3 15.1% Pt / CNT 9.8% Pt / Al_2O_3	1.2, 1.5(SAXS***) 1.5, 1.7(SAXS***) 1.9, 2.4(SAXS***)	Air, lab	XAS / Air In-situ **XRD(SLS)** / Air	PtO****
Bhattacharya, et al. [74]	2014	Ru / Dendrimer	2.1, NR	Aqueous in air; drying in N_2	TEM / UHV XPS / UHV	RuO_2
Banerjee, et al. [30]	2017	2.7% Pt / C 2.4% Pt / C 10% Pt / C 6.9% Pt / CX 17.3% Pt / CX 20% Pt / C 5.4%Pt/SBA-15 5% Pt / SiO2 5.5%Pt/SBA-15 10%Pt/SBA-15	NR, 1.5 NR, 1.6 NR, 2.2 NR, 1.5 NR, 3.9 NR, 4.3 NR, 1.2 NR, 1.6 NR, 1.1 NR, 1.5	Air, lab	**XRD(lab)** / Air XPS / UHV STEM / UHV	Pt_3O_4 (223)**
Qin, et al. [76]	2017	7.3% Ir / CeO2-C 8.5% Ir / C	1.1, NR 1.5, NR	Dried in air	XPS / UHV	IrO_2
Banerjee, et al. [77]	2018	2.7% Pt / C 2.4% Pt / C 10% Pt / C 6% Pt / CX 6.4% Pt / CX 10% Pt / CX 12.8% Pt / CX 17.3% Pt / CX 6.5% Pt / CX 6.5% Pt / CX 10.3% Pt / CX 16.4% Pt / CX	NR, 1.5 NR, 1.6 NR, 2.2 NR, 1.4 NR, 1.5 NR, 1.7 NR, 1.9 NR, 3.9 NR, 1.5 NR, 1.4 NR, 1.8 NR, 2.8	Air, O_2	XRD / Air XPS / UHV	Pt_3O_4 (223)
Ye, et al. [78]	2021	2% Pt / SiO_2 2% Pd / SiO_2	2.2, NR 2.8, NR	Air, lab	In-situ XAS / air	NR

* NMR peak position was shown later by Bucher, et al. [29] and Tong and van der Klink [64] to also correspond to PtO_2.
** Authors state they are not sure of the exact oxide. *** Authors use STEM for the number-weighted average, and SAXS for the volume-weighted average. ****Authors used a fully oxidized nanoparticle sample as the reference for PtO

Experimental

Synthesis

Synthesis of Pt, Pd, Ir, Rh, and Ru nanoparticles on silica support

Aerosil 300 obtained from Evonik was used as the silica support. The BET surface area was determined from nitrogen adsorption-desorption isotherms with a Micromeritics 2020 ASAP instrument as 330 m^2/gm. The point of zero charge (PZC) was determined by measuring the initial and final pH of a series of thick slurries at high surface loadings and determined as 3.9. Strong Electrostatic Adsorption (SEA) method was adopted to impregnate the A300 silica with Pd, Pt, Ir, Rh and Ru. SEA relies on the PZC of the support for the selection of the precursor which was determined to be cationic for all the metals based on the low PZC of the A300 silica. The precursors used were Tetraammineplatinum (II) chloride ($Pt(NH_3)_4Cl_2$), Tetraamminepalladium (II) chloride ($Pd(NH_3)_4Cl_2$), Hexaammineruthenium (III) chloride ($Ru(NH_3)_6Cl_3$), Pentaamminechloroiridium (III) chloride (IrPA,$[Ir(NH_3)_5Cl]Cl_2$, Tris(ethylenediamine)rhodium (III) Chloride Trihydrate, ($C_6H_{30}Cl_3N_6O_3Rh$) for platinum, palladium, ruthenium, iridium and rhodium respectively. The as-prepared samples were reduced in 10% hydrogen for one hour at a ramp rate of 2.5℃/min. The resultant metal loadings and reduction temperatures for each of the precursors are listed in Table 2.2, along with references used in choosing the reduction temperatures.

TPR was conducted using a Micromeritics Autochem II 2920 Analyzer. The 4.3% Rh / SiO_2 sample was pre-dried under 50 SCCM Ar for 1 hr at 120°C and a

ramp of 10°C min^{-1}. The sample was then cooled to 40°C and the gas flow was switched to 50 SCCM of H_2 (balance Ar). After waiting 10 minutes beyond the time when the baseline was deemed stable, the sample was ramped to 800°C at 5° min^{-1}.

Table 2.2. Reduction temperatures and corresponding references for the non-Au samples.

Catalyst	Reduction Temperature (°C)	References
4.8% Pt / SiO_2	200	Wong, et al. [79]
4.2% Pd / SiO_2	180	Wong, et al. [79]
4.1% Ir / SiO_2	350	*Keels, et al. [80]
5.4% Ru / SiO_2	350	Liu, et al. [81]
4.3% Rh / SiO_2	300	TPR: Figure 2.8

* This reference uses a different (anionic K_2IrCl_6) precursor on an alumina support, and suggests reduction takes place by 150°C.

Synthesis of Au nanoparticles on silica support

Amorphous SiO_2 (Aerosil 300) was used directly from Evonik, the point of zero charge (PZC), surface area, and water accessible volume of which were 3.4, 304 m^2/g and 2.5 ml/g, respectively. For this low PZC material a cationic gold precursor, gold bis-ethylenediamine $[Au(en)_2Cl_3]$, was prepared according to the literature Block and Bailar Jr [53] using chloroauric acid, ethylenediamine, ethyl ether and anhydrous ethanol, all from Alfa Aesar. Supported gold catalysts were then prepared by the SEA method described in the previous report Noble, et al. [54]. The SEA protocol was modified to prepare a lower weight loading Au sample as follows: the freshly prepared $Au(en)_2Cl_3$ solution was diluted to a concentration of 40 ppm; the pH was adjusted by a NaOH solution to 11.7 to get the maximum uptake of $Au(en)_2Cl_3$. The required amount of support was then added to give a

surface loading of 1000 m^2/L. The solution was shaken for 1 h, vacuum filtered, and dried in a fume hood for 72h. The mass loading of the Au SEA sample was determined by ICP-OES to be 0.84% Au. The gold sample was reduced in a horizontal reduction furnace under 20% H_2 in N_2 with a total flow rate of 250 sccm at 400^0C for 1h with a ramp of 5°C/min. A reference support was prepared by pH treating and heat treating pure A300 silica under similar conditions to the respective SEA sample, only with no precursor.

Synthesis of reference supports

For increased accuracy in the XRD background subtraction, a reference support was prepared for each metal by pH treating and heat treating pure Aerosil 300 silica under similar conditions to the respective SEA sample, only with no precursor.

Scanning Transmission Electron Microscopy (STEM)

High and low magnification Z-contrast images of all the catalysts were obtained with an aberration-corrected JEOL 2100F High Angle Annular Dark-Field scanning transmission electron microscope (STEM) equipped with a 200 kV field emission gun and a double tilt holder for tilting the sample across a range of angles (±20°). The microscope is attached to a Fischione Model 3000 HAADF detector with a camera length such that the inner cut-off angle of the detector is 50 mrad. Sample preparation involved griding the sample using a mortar and dispersing it on a copper TEM grid with a thin holey carbon coating. The images were recorded using Gatan Digital Micrograph software and particle size distributions were obtained by measuring >1000 particles on the sample (with the exception of Ru,

for which only 200 particles could be counted due to low contrast). Particle size analysis was performed using Particule2 software (Robiche [82]).

XRD

Sample preparation

Samples and supports were finely ground with an agate mortar and pestle prior to loading into the sample holder. All samples were measured in the same sample holder, which consisted of a “Zero Diffraction Plate” from MTI corporation custom-mounted into an aluminum holder from Rigaku (MiniFlex II Base Unit # 2005H303). The Zero Diffraction Plate consisted of a single crystal of P-type, B-doped silicon cut at a high index plane 24.6mm in diameter and 1.0 mm thick with a center cavity nominally 10 mm in diameter and 0.2 mm deep (measured in-house to be 10.2 mm in diameter and 0.29 mm deep). Prior to loading the samples into the holder, it was determined that approximately 8.0 mg of the sample/support would properly fill the center cavity; this was the mass targeted for all loadings (using an initial target mass minimizes the amount of correction needed to adjust supports to their respective nanoparticle samples and thus reduces the overall error of the background subtraction). For each sample, the target mass was measured out and loaded into the sample holder using the method detailed in our previous work (citation). In brief: once the target mass was deposited into the center cavity, an antistatic microspatula (VWR) was used to evenly distribute the sample across the cavity and then tuck in the sample about 1mm from the cavity edges (to minimize sample spilling from the cavity during smoothing). Finally, a

strip of wax paper was placed against a glass slide and gently rotated back and forth across the surface of the sample to smooth it.

XRD measurement

The nanocluster samples and corresponding supports were measured one at a time in a Rigaku MiniFlex II Powder X-ray diffractometer equipped with a silicon strip D/tex Ultra linear position sensitive detector (LPSD) and operating at 30kV and 15mA in Bragg-Brentano geometry with the following hardware parameters: goniometer radius = 150mm, primary and secondary Soller slits = 5° (2θ), divergence slit = 1.25° (2θ), antiscatter slit = 8 mm, no receiving slit, and LPSD angular range of 4.89° (2θ). Because the x-ray source flux showed significant variation over time (believed to be a result of using cooling water without temperature control), each sample was scanned six times from 6 to 120° 2θ with a sampling width of 0.02° (2θ) and scan rate of 5° min^{-1}. The (1 0 4) reflection of a NIST 1976c intensity standard was measured before and after each scan from 34.8 to 35.6° 2θ at a scan rate of 2° min^{-1} and sampling width of 0.01° 2θ. This reflection was fit as a fundamental parameter peak in Topas V.6.0; the resulting scale factor was recorded and used to normalize all sample scans to a common x-ray source intensity using Microsoft Excel. The method for normalizing each sample scan was to assign every data point a scale factor obtained from linearly interpolating between the NIST 1976c scale factors taken directly before and after each scan based on the time at which each data point was measured. Once normalized, the six scans taken for each sample were averaged together to give a total scan rate equivalent to around 0.83° (2θ) min^{-1}. At the conclusion of each

XRD measurement, the mass of the sample in the sample holder cavity was measured and recorded.

Background subtraction and support correction

To identify the background, the empty sample holder was measured under regular sample conditions and corrected for the varying x-ray intensity. By comparing with a ceria sample (with x-ray absorption sufficiently high to completely block x-rays from reaching the bottom of the sample cavity) it was determined that the sample-dependent signal of the sample holder reaching the detector was small in comparison to the sample-independent signal (Lipp, et al. [61]). The diffractogram of the empty sample holder was therefore used as an approximation of the background, with small adjustments made where the empty sample holder diffractogram showed broad peaks (Figure 2.1A).

The method detailed previously (Lipp, et al. [61]) was used to determine the support contribution in each nanocluster sample. Briefly, the x-ray absorption coefficient μ/ρ [cm^2 g^{-1}] of each nanocluster sample and pure support was calculated using the absorption coefficients reported in Hubbel and Seltzer [14]. Packing densities ρ [$g\ cm^{-3}$] were calculated from the sample cavity dimensions and mass of each sample; the x-ray absorption μ [cm^{-1}] of each sample was then determined for each nanocluster sample and its reference. The estimated background was subtracted from each pure treated support using Fityk software (Wojdyr [28]) (Figure 2.1B). Microsoft Excel was used to correct each background subtracted pure treated support for differences in x-ray absorption and finite thickness between it and its corresponding nanocluster sample (Figure 2.1C). The

estimated background was finally added back to the corrected support to be used as the total background during analysis in Topas (Figure 2.1D).

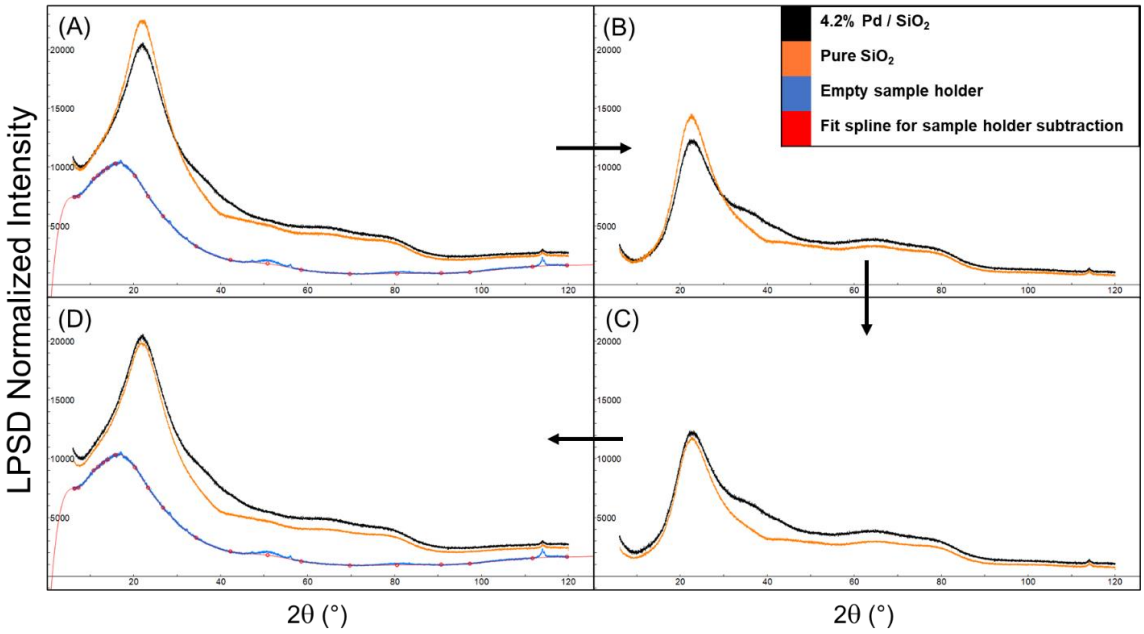

Figure 2.1. Background subtraction method as applied to the 4.2% Pd / SiO_2 sample and reference.

Analysis

The nanocluster samples were analyzed using Rietveld refinement with Topas V.6.0 according to the method detailed in (Lipp, et al. [61]). In short, the Topas macros were modified prior to analysis to perform intensity corrections on a point-by-point basis (to properly account for any angle dependent intensity effects such as “peak-pulling.” The Topas macro for beam spill was also updated to give a more accurate 2-D correction. For each nanocluster sample, the corrected support was first imported into Topas and the background was fit against it with a high-order Chebychev polynomial. The fitting range for all cases except Rh was kept between 20° and 100° (2θ); for Rh the minimum range was limited to 28° (2θ) due to

observed discrepancies between the support and metal sample at low angles (possibly due to differences in surface roughness between the samples). The background polynomial coefficients were then fixed, and the scan data was replaced with the averaged nanocluster diffractogram. For each metal, the respective phases listed in Table 2.3 were investigated (an expanded table showing the corresponding Inorganic Crystal Structure Database [ICSD] numbers is provided in the supplementary information, Table 2.5). For the first analysis, only the overall scale factor and gaussian size were allowed to refine for each phase, all other parameters were fixed to measured or calculated values. Peaks were calculated from ICSD structure files using the fundamental parameter model. Once reasonable fits were identified, the lattice parameter of the reduced metal only was refined. Surface roughness according to the model by [20,] Pitschke, et al. [24] was also allowed to refine up to the maximum values of A_1=0.174 and A_2=0.0436 (Lipp, et al. [61]).

Table 2.3. Metal and metal oxide phases investigated in this study. The numbers inside parenthesis indicate the space group.

Au	**Pt**	**Pd**	**Ir**	**Rh**	**Ru**
Au (225)	Pt (225)	Pd (164)	Ir (225)	Rh (191)	Ru (194)
Au_2O_3 (43)	PtO (131)	Pd (225)	IrO_2 (136)	Rh (225)	RuO_2 (58)
	PtO (225)	Pd_2O (224)	IrO_2 (205)	Rh_2O_3 (60)	RuO_2 (136)
	PtO_2 (58)	PdO (123)		Rh_2O_3 (61)	RuO_2 (205)
	PtO_2 (136)	PdO (131)		Rh_2O_3 (167)	RuO_4 (15)
	PtO_2 (164)	PdO (139)		RhO_2 (136)	RuO_4 (218)
	PtO_2 (186)	PdO (225)		RhO_2 (205)	
	PtO_2 (205)	PdO_2 (136)			
	PtO_2 (224)	$Pd_{0.5}(Pd_3O_4)$ (223)			
	Pt_3O_4 (223)				
	Pt_3O_4 (229)				

XAS

Instrumental Setup

The XAS data were collected at Continuous XAS beamline 9-3 at SSRL. The beamline uses a 20 pole, 2-Tesla Wiggler insertion device placed within the 3 GeV storage ring with beam current ~500 mA. The harmonic rejection was done by detuning the mirror (M0) placed prior to the monochromator to reduce the flux at 500 eV above the Pt L3 absorption edge to nearly 40% of the maximum intensity. The beam size was 1 mm [v] × 4 mm [h]. The XAS data were collected in transmission mode using two 15 cm long ionization chambers (IC) filled with argon gas. The angle of the monochromator was set to 90° and the energy was tuned from 11,365 to 12,537 eV for a complete absorption spectrum. A 7.5 μm thick Pt foil was placed in front of a 3rd IC to measure the absorption spectra of the foil simultaneously as a reference for energy calibration.

Approximately 40 mg of the undiluted 4.8 wt% Pt/SiO_2 sample was loaded as received in a Kapton tube with 3.0 mm outer diameter, 25μm wall thickness. A catalyst bed of 10 mm was filled to achieve total absorption of 2.5 above the edge with an estimated edge step $\Delta\mu$~0.62. The tube was fitted gas-tight using rubber O-ring and placed at the center of the custom build reactor cell (Hoffman, et al. [56]). The details of the in-situ cell connections and setup are explained elsewhere (Asundi, et al. [57]).

In-situ data collection procedure

The in-situ XAS data were collected in different stages of a temperature programmed reduction process. Before the in-situ experiment was started the pipelines and gas flow systems were purged with He gas to remove excess amounts of air and moisture inside. At the beginning one scan was collected at room temperature with flowing He gas (20 ml min^{-1}) through the reactor to see the signal to noise ratio; once the sample stabilized under the He flow 4 scans were collected on the as-received sample at room temperature. Next the sample was heated from room temperature to 100°C at a 5°C min^{-1} ramp rate and 30-minute dwell time until no change in the XANES spectra was observed. Following the desorption, the sample was cooled down to room temperature and steady state scans were recorded at room temperature under He flow. The reduction process was started by introducing the H_2 gas into the reactor at a flow rate of 2 ml/min and reducing the He flow rate to 18 ml/min to keep the total flow rate constant at 20 ml/min. After the H_2 gas was observed in the product stream the sample was heated up to 200°C with a 5°C/min ramp rate and dwelled for 30 minutes until no further changes in the XANES spectra were observed and the absorption edge approximated the Pt foil reference. The steady state scans were taken at room temperature after cooling down the sample in the presence of pure He flow to avoid any hydride formation. The oxidation of the reduced catalyst was done by exposing the catalyst to 20% of O_2 balanced with He gas at room temperature and left over for a long time. Finally when the catalyst was potentially oxidized the steady state scans were collected. It is to be noted that in every steady state condition, a total

4 scans were collected and merged to increase the signal to noise ratio. These steady state scans measured under He at room temperature are defined as (i) as-prepared, (ii) desorbed, (iii) reduced, and (iv) oxidized.

Results

STEM

STEM images and the corresponding size distributions of each metal sample are presented in Figure 2.2. In all cases the number weighted average particle size is around 1 nm; each volume weighted particle size (directly comparable to the XRD particle sizes) is less than 2 nm. It is noted that for the Au sample a few larger particles (at least one on the order of 8.0 nm) were observed in the electron microscope. The presence of these larger particles is attributed to the sample sintering over time, possibly due to light or humidity exposure, but the overall percentage is very low, as is evidenced by XRD (see below).

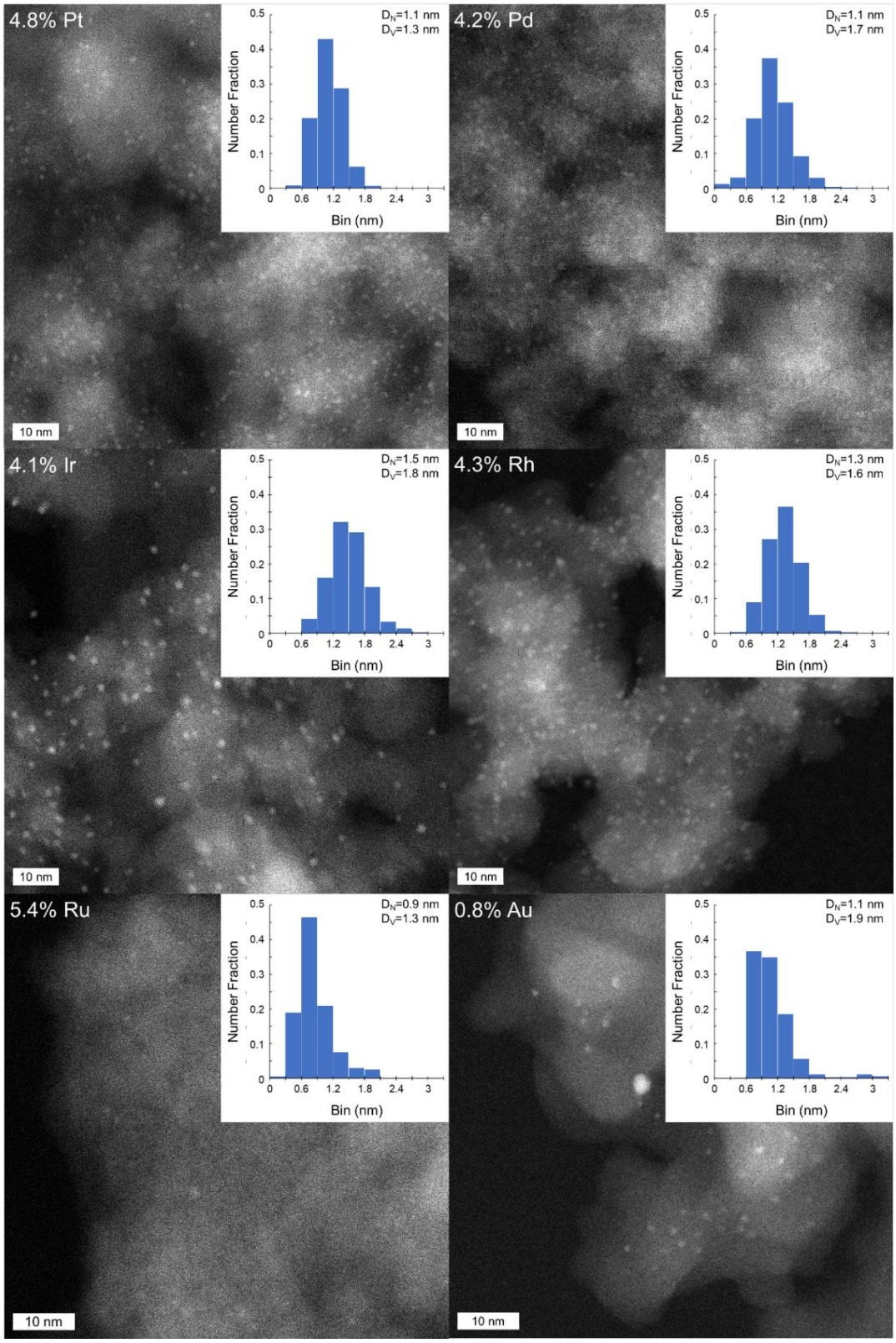

Figure 2.2. Representative STEM images and particle size histograms.

XRD

Figure 2.3 shows the nanocluster samples overlaid with their pure supports after normalizing all diffractograms to a common x-ray source intensity based on external measurements of a NIST 1976c intensity standard. In each case, the silica in the pure support shows more intensely than the silica in the nanocluster samples; this is especially visible at the top of the silica peak centered around 22° 2θ. This is a direct consequence of the higher x-ray absorption in the nanocluster samples. Notice that the effect is least noticeable for the lowest weight loading sample, 0.84% Au. For this sample the difference in x-ray absorption between the metal-containing sample and pure support is small but still noticeable.

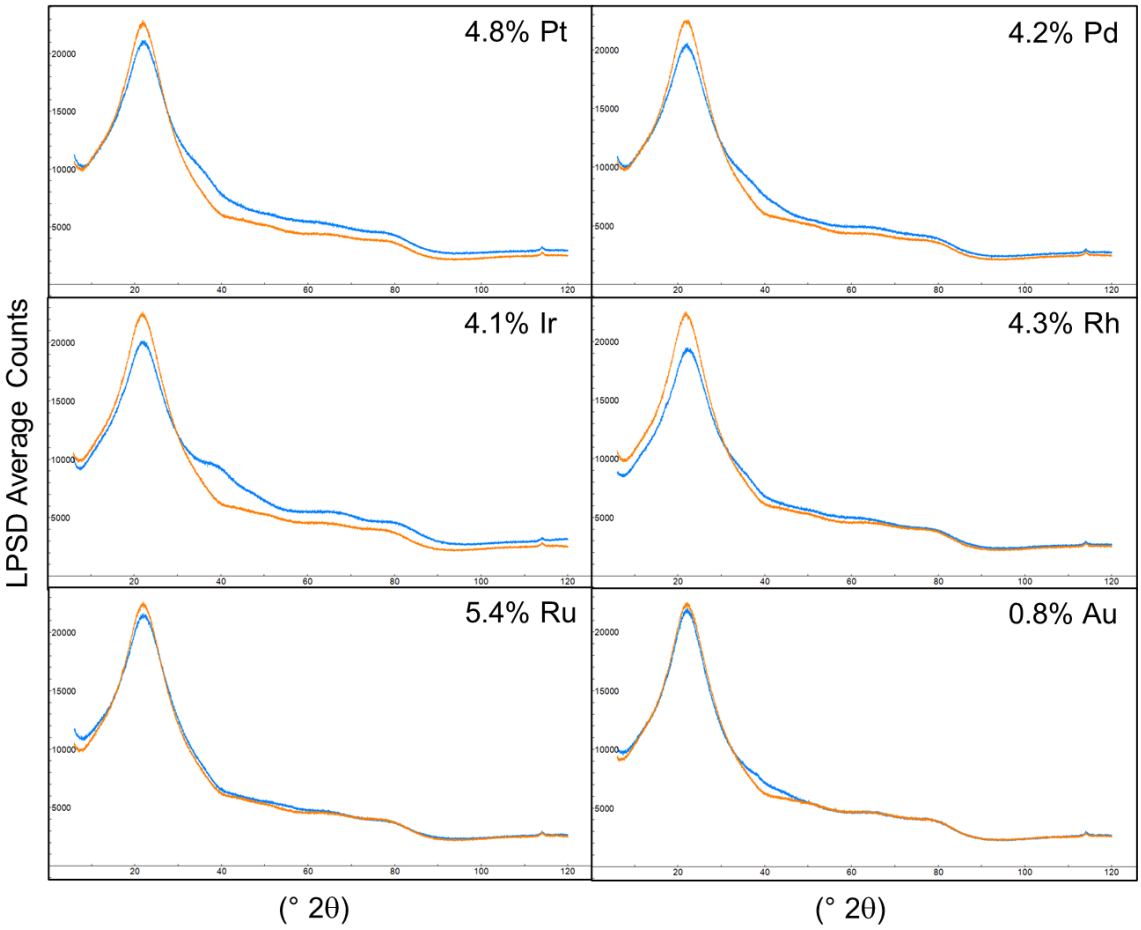

Figure 2.3. X-ray diffraction images after correcting for differences in x-ray flux with a NIST 1976c intensity standard. For each figure, blue shows the nanoparticle sample while orange shows the pure support.

The background and support subtracted XRD diffractograms are displayed along with their calculated fits in Figure 2.4. The Pt, Pd, and Rh samples are all fit with a minor metallic phase and a majority oxide phase; Ir is fit with approximately equal amounts of Ir^0 and Ir oxide. Overall, the amount of oxide trends with total particle size; smaller particle sizes correspond to a greater extent of oxidation. This trend is more easily seen in Table 2.4, which compares the STEM and XRD results.

Interestingly, in all cases the oxide phase showing the best fit corresponds to the stoichiometric relation MO_2, where M is either Pt, Pd, Ir, or Rh. Also of

interest is that for each of these samples the best fitting oxide phase is either tetragonal (space group 136) or orthorhombic (space group 58); these two structures broaden to give similar diffraction patterns. Figure 2.7 compares fits of the 4.8% Pt / SiO_2 sample using the separate space groups; the results are nearly indistinguishable.

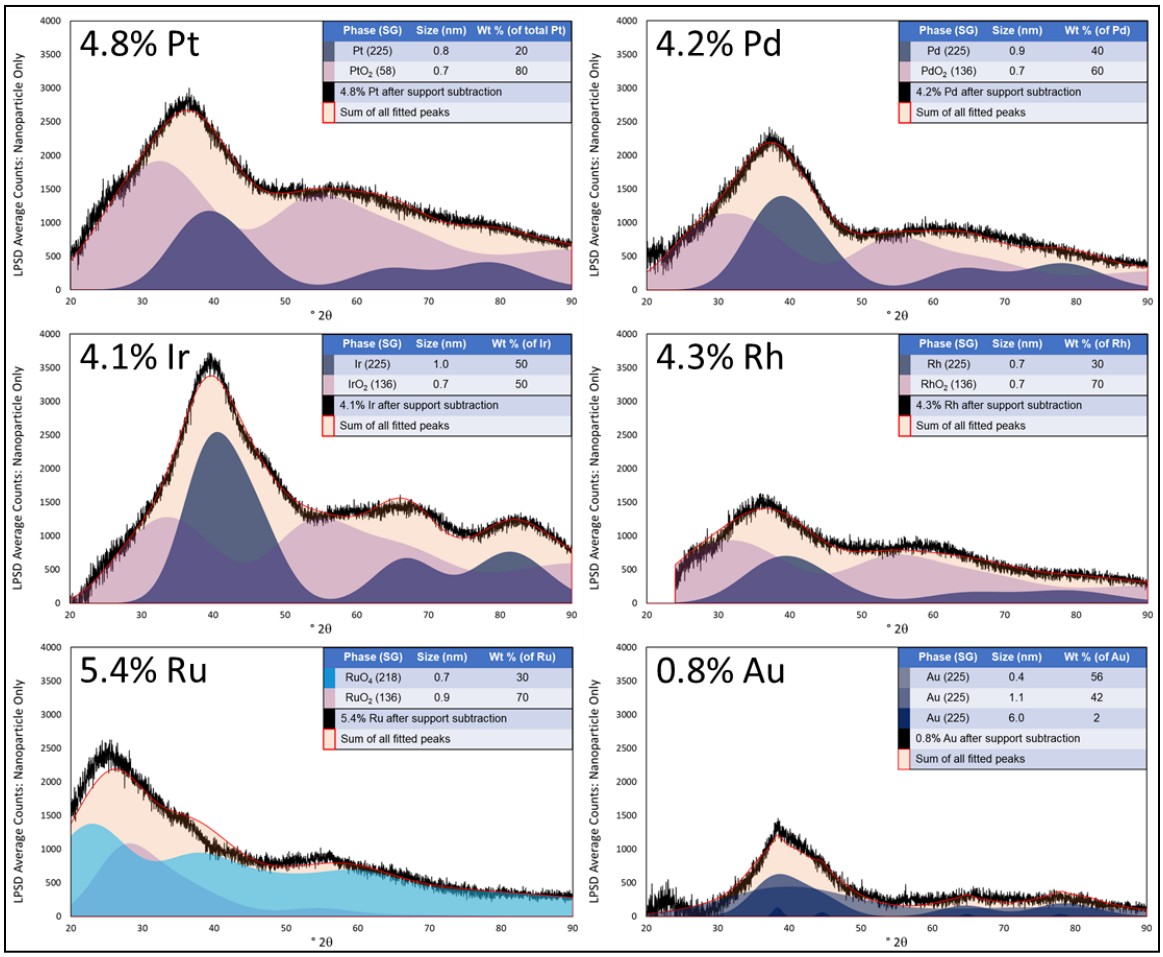

Figure 2.4. XRD Rietveld fits, after background subtraction. In the shown fit, only a few terms were allowed to refine: the Gaussian size broadening and overall scale factor for each phase, the metal lattice parameter, and two terms adjusting the intensity for surface roughness. All other terms were fixed.

Table 2.4. STEM and XRD results.

Metal	STEM D_V [nm]	XRD phase	XRD D_V [nm]	Wt% of metal	Fit L.P. [Å]	Bulk L.P. [Å]	L.P. % change
4.8% Pt	1.3	Pt (225)	0.8	20	4.045	3.9237	+3.1

		PtO_2 (58)	0.7	80	N/A	N/A	
4.2% Pd	1.7	Pd (225) PdO_2 (136)	0.9 0.7	40 60	4.06 N/A	3.8902 N/A	+4.4
4.1% Ir	1.8	Ir (225) IrO_2 (136)	1.0 0.7	50 50	3.934 N/A	3.8394 N/A	+2.5
4.3% Rh	1.6	Rh (225) RhO_2 (136)	0.7 0.7	30 70	4.019 N/A	3.8034 N/A	+5.7
5.4% Ru	1.3	RuO_4 (218) RuO_2 (136)	0.7 0.9	30 70	N/A N/A	N/A N/A	
0.8% Au	1.9	Au (225) Au (225) Au (225)	0.4 1.1 6.0	56 42 2	3.789 4.053 4.066	4.0781 4.0781 4.0781	-7.1 -0.6 -0.3

XAS

Pt L3-edge XANES

To estimate the formal oxidation state of the Pt in the catalyst, the normalized Pt L_3-XANES spectra of the catalyst at four different steady state conditions were compared with those from metallic Pt and Pt(IV)standards, Figure 2.5. It is observed that in the as-prepared state the average oxidation state is slightly lower than the Pt^{4+} state of the bulk PtO_2 reference. Linear combination fitting, using bulk standards, suggests the as-prepared state consists of ~34% Pt metal and ~66% PtO_2, the dehydrated / desorbed state 60% metal, the reduced state 100% metal, and the final oxidized state 34% metal. We postulate that the decrease in the white line intensity in the dehydrated state is primarily due to the removal of adsorbed oxygenates from the surface of as-prepared catalysts. In the reduced state the absorption edge resembles that of metallic Pt, suggesting a completely metallic state after reduction. Interestingly, the XANES spectrum after re-oxidation is almost identical to that of the as-received sample.

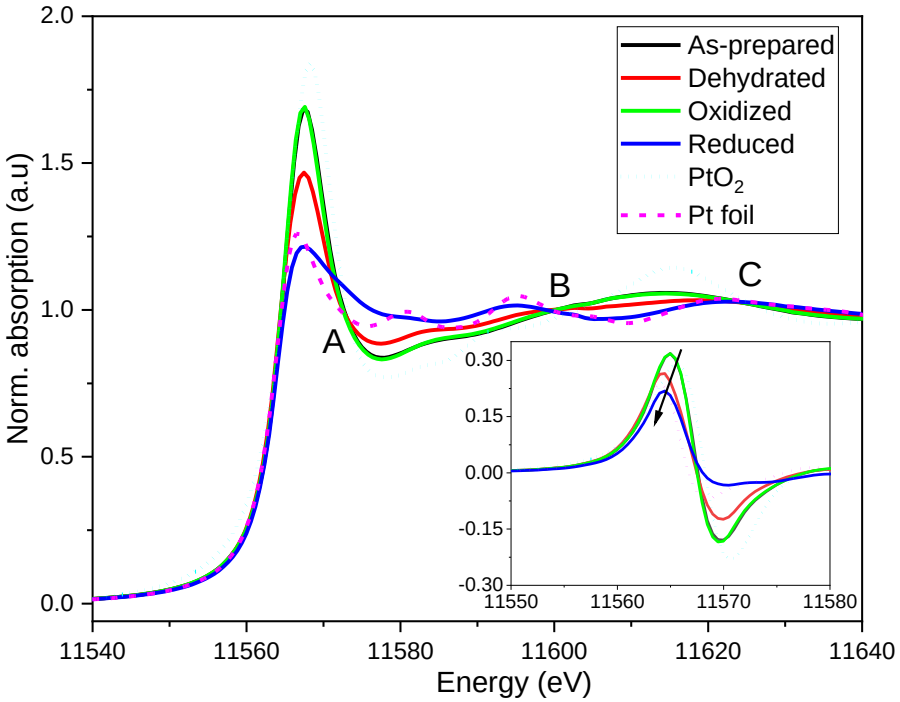

Figure 2.5. Normalized XANES spectra of the catalyst at four steady-state room temperature conditions compared with Pt foil and PtO_2 standards. The inset to the figure shows the first order derivative of the normalized XANES spectra. The arrow represents the shift in the absorption edges.

Reduction and Oxidation kinetics

The linear combination fitting results for the Pt sample during drying, reduction, and oxidation are shown in Figure 2.6. During the pre-drying step (Figure 2.6 a) the percent of Pt oxide is observed to decrease. This is attributed to de-adsorbing oxygenates. The following reduction takes place very quickly (Figure 2.6 b). Finally, re-oxidation occurs in dry O_2 at room temperature and reaches steady state after around 20 minutes (Figure 2.6 c).

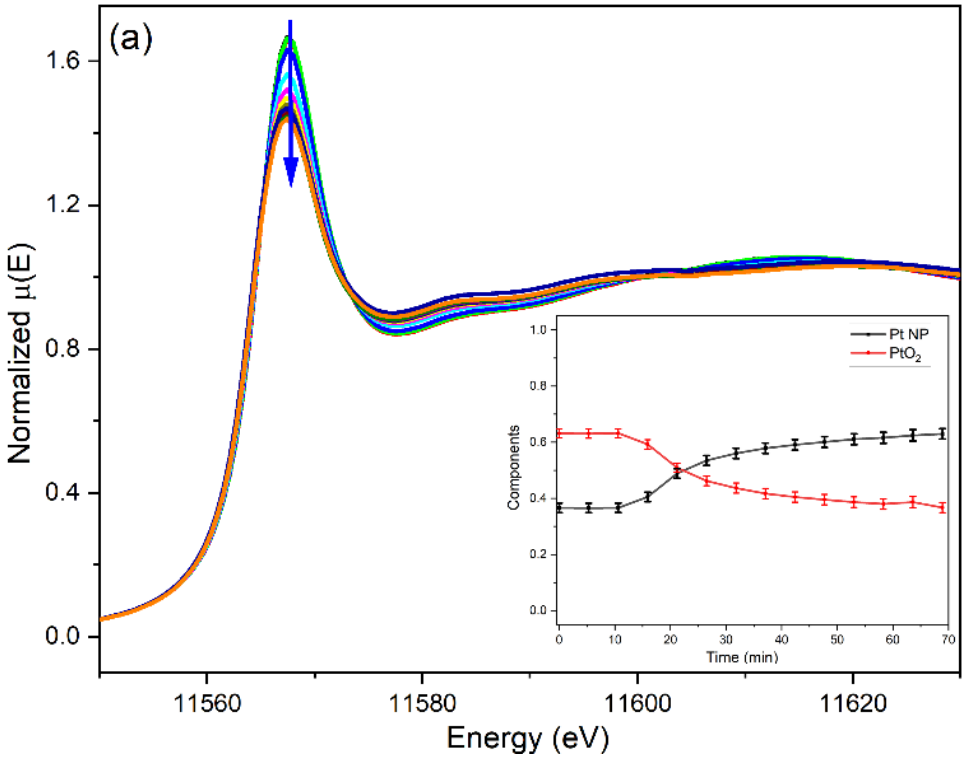
(a)
Normalized μ(E)
Energy (eV)
Components
Time (min)
Pt NP
PtO2

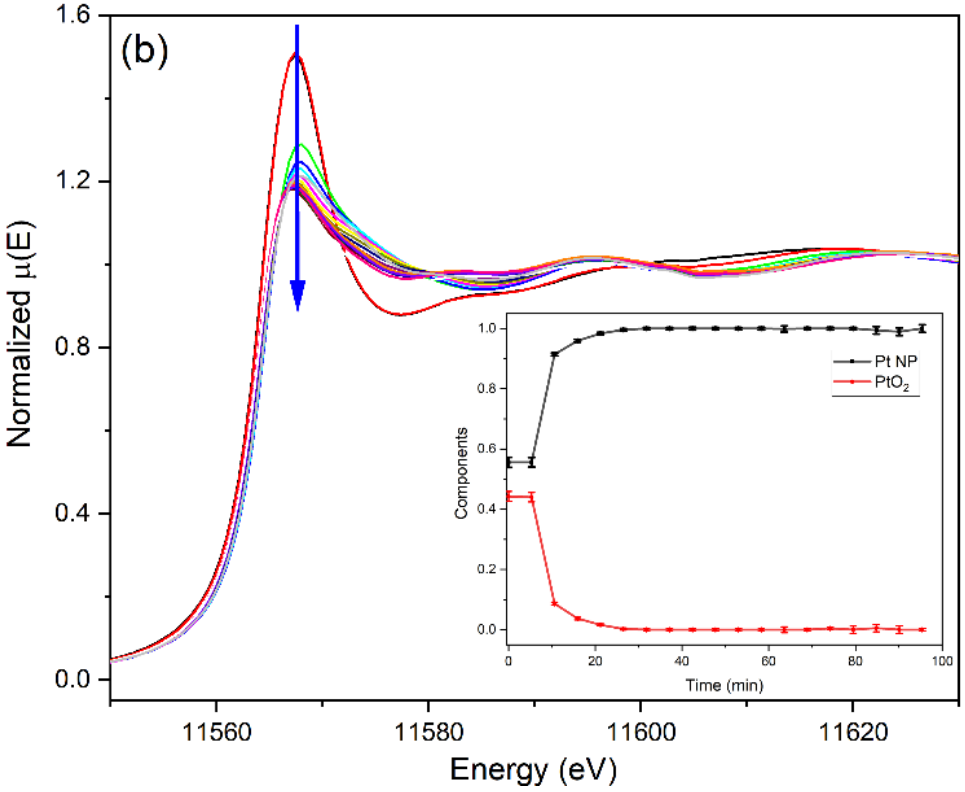
(b)
Normalized μ(E)
Energy (eV)
Components
Time (min)
Pt NP
PtO2

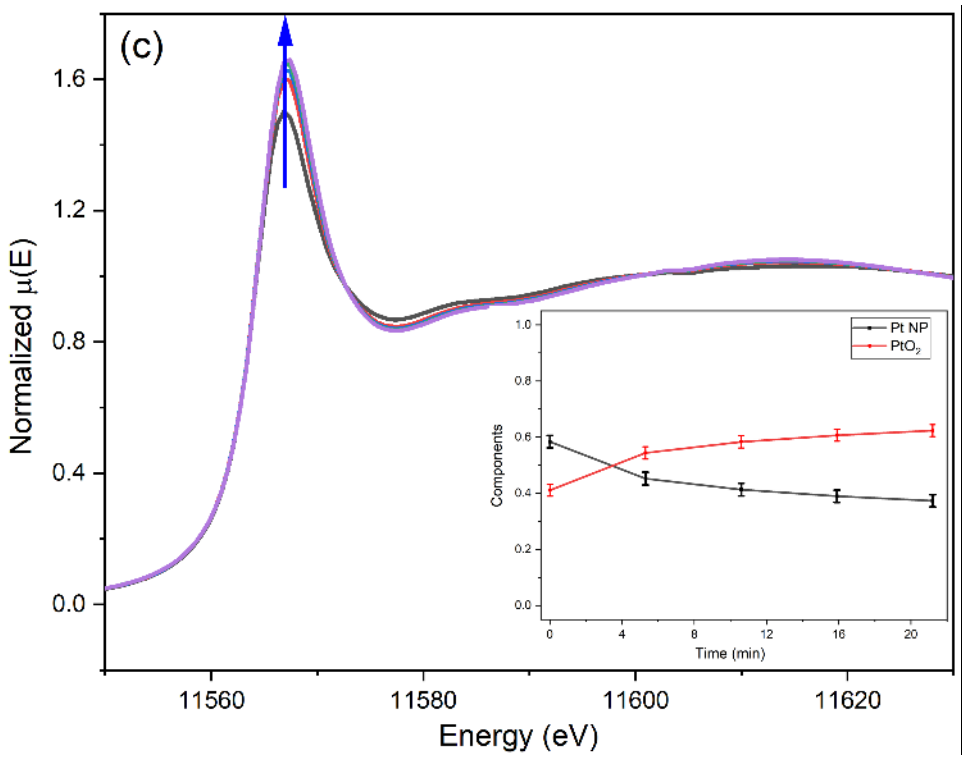

Figure 2.6. Normalized XANES spectra during the (a) He ramp, (b) H_2 ramp, (c) O_2 flow. Insets to the figure shows the LCF results fitted with the Pt reduced/NP and PtO2 standard.

Discussion

Size dependence of oxidation

A key concept of this work is that the temperature of oxide formation is a size effect. Noble metals are so named because of their stability in many environments, yet their stability is a bulk property. As noble metal crystallites become smaller, oxidation becomes easier. As one example, Blomberg, et al. [83] observed with high pressure XPS that 21 nm Rh / SiO_2 particles showed a greater extent of oxidation than bulk Rh(100) at 140°C and under 0.1 torr of O_2. The size effect becomes even more pronounced for smaller nanoparticles where at room temperature particle size dictates whether oxide is formed or not. This is thoroughly established in the literature (Gallagher, et al. [3], Vogel, et al. [11], Ingham, et al. [72],

Miller, et al. [2], Banerjee, et al. [30] and Banerjee, et al. [77]). Our results confirm that small noble metal nanoparticles form significant amounts of oxide, with gold the one exception. This is not unexpected, since Miller, et al. [2] noted that Au was quite resistant to oxidation, with only the smallest nanoparticles forming a maximum of 10-15wt% oxide. We used a low weight loading of Au (0.8wt%) in this work to keep particle sizes small; a 15% oxide formation on this sample would almost certainly be below the detection limit of the XRD. However, we also note that the Au sample follows the expected peak shift toward higher 2θ, indicating lattice contraction rather than expansion. If the oxide surface was oxidized, then we might expect to see a peak shift to lower 2θ even if the oxide is undetectable (see below).

Metallic core, oxide shell

Almost universally throughout literature the authors show partial oxidation only – usually attributed to surface oxidation around a metallic core (Rhodes, et al. [62], Martens, et al. [63], Gnutzmann and Vogel [10], Yang, et al. [70], Miller, et al. [2], Vogel [12], Ingham, et al. [72], Ye, et al. [78]). Gallagher, et al. [3]. Banerjee, et al. [30] and Banerjee, et al. [77] expand on this model by combining it with the particle size effect: they suggest that the smallest particles are completely oxidized while the largest particles are fully metallic; only intermediate particles contain metallic core – oxide shell particles. Since most samples have a size distribution that contains particles in all three ranges, each sample will have a combination of the three types of particles – the percentage of each corresponding to the overall amount of oxide observed in the sample.

Our results show that for the four partially reduced samples (Pt, Pd, Ir, Rh) the STEM volume-weighted average particle diameter is approximately equal to the sum of the XRD metal and metal oxide dimensions (Table 2.4). This, together with the lower quantity of the metal as compared to the metal oxide, is consistent with a metallic core in direct contact with the support and surrounded by an oxide shell, as was reported for Pt in Banerjee, et al. [30] and discussed in our previous work[61]. Our results for Ru are similarly consistent with a partially oxidized core and a fully oxidized shell.

Surface oxide phase

In the literature, conflicting results are provided for the identification of the oxide phase for each ambiently oxidized metal (Table 2.1). Our results reveal that the oxide phase of Pt, Pd, Ir, and Rh are all best fit with a dioxide, either tetragonal (space group 136) or orthorhombic (space group 58), though preliminary results suggest that different environments (e.g. high humidity) may result in the formation of different oxide phases. Also of interest is that under these conditions, the XRD determined size for each of these four metals is 0.7 nm. This may suggest similar oxide shell dimensions.

Lattice parameter expansion

In our previous work[61], we noted that the lattice parameter of the metallic Pt core appeared in the XRD to be expanded beyond the bulk (+ 3.1%), as evidenced by a shift of the peaks to lower-angles. This was in contrast to the size contraction commonly reported in the literature for small nanoparticles (Miller, et al. [2], Lamber, et al. [31]), and was suggested to be caused by the oxide shell (Du, et al. [34]). We

now expand upon those results by showing a similar lattice expansion for the Pd (+4.4%), Ir (+2.5%), and Rh (+5.7%) metallic cores (Table 2.4). This lattice expansion is not a result of peak pulling, as we have accounted for the relevant angle-dependent effects on a point-by-point basis. Similar XRD peak shifts to lower angles for partially oxidized ultra-small nanoparticles are reported throughout the literature (Le Rhun, et al. [69],Vogel, et al. [11], Ingham, et al. [72],Gallagher, et al. [3]), the latter of these then documents lattice contraction with XRD after the nanoparticles are reduced in-situ.

Oxidation / reduction kinetics

The in-situ XANES experiment reveals that the room temperature oxidation / reduction kinetics of the Pt sample are quick. Quick room temperature reduction (on the order of minutes) of partly oxidized Pt nanoparticles has been observed before (Gnutzmann and Vogel [10], Vogel [12], Gallagher, et al. [3]). Room temperature oxidation kinetics of noble metal nanoparticles have not been studied as carefully, to the best of our knowledge these are the first reported in-situ kinetic oxidation data for such a system under ambient conditions. While not studied in this work, the remaining noble metals (Au exempt) are expected to oxidize even more readily based on the relative propensity for bulk systems to oxidize (Chan, et al. [65], Saliba, et al. [67], Luo, et al. [68]).

Conclusion

Benchtop XRD has been used to characterize the oxidation of noble metals (Pt, Pd, Ir, Rh, Ru) under ambient conditions. Au was not observed to oxidize, though this could be due to the low weight loading (0.8%) resulting in any oxide

being below the detection limit. The room temperature oxidation of these metals is a function of particle size; oxidation begins at the surface and tends to form an oxide shell around a metallic core unless the entire particle is oxidized – as is the case with Ru. Surface oxidation appears to expand the lattice parameter of the metallic core in core-shell particles; lattice contraction is observed for the Au sample, consistent with reduced nanoparticles. In-situ XANES reveals that the room temperature oxidation / reduction kinetics of these systems are quick, on the order of minutes. Future work is needed to examine the oxidation mechanism, including the role that water may play (Chan, et al. [65], Luo, et al. [68], Tong and van der Klink [64], Rhodes, et al. [62]).

Acknowledgements

Doug Blom, for STEM imaging of the 0.84% Au / SiO_2 sample.

Funding from the National Science Foundation IGERT program (Award Number 1250052)

South Carolina Smart State Center of Catalysis for Renewable Fuels (CReF)

References

1. Lipp, J.; Banerjee, R.; Patwary, M. D. F.; Patra, N.; Dong, A.; Girgsdies, F.; Bare, S. R.; Regalbuto, J. R., The extension of Rietveld refinement for benchtop powder XRD analysis of ultra-small supported nanoparticles *Chemistry of Materials* **In Preparation**.

2. Rhodes, H. E.; Wang, P.-K.; Stokes, H. T.; Slichter, C. P.; Sinfelt, J., NMR of platinum catalysts. I. Line shapes. *Physical Review B* **1982,** *26* (7), 3559.

3. Martens, J.; Prins, R.; Koningsberger, D., Controlled oxygen chemisorption on an alumina supported rhodium catalyst. The formation of a new metal-metal oxide interface determined with EXAFS. *The Journal of Physical Chemistry* **1989,** *93* (8), 3179-3185.

4. Bucher, J.; Buttet, J.; Van der Klink, J.; Graetzel, M., Electronic properties and local densities of states in clean and hydrogen covered Pt particles. *Surface Science* **1989,** *214* (3), 347-357.

5. Gnutzmann, V.; Vogel, W., Structural sensitivity of the standard platinum/silica catalyst EuroPt-1 to hydrogen and oxygen exposure by in situ X-ray diffraction. *Journal of Physical Chemistry* **1990,** *94* (12), 4991-4997.

6. Tong, Y.; van der Klink, J., Local metal to non-metal transition on oxygen-covered platinum particles from 195Pt nuclear magnetic resonance. *Journal of Physics: Condensed Matter* **1995,** *7* (12), 2447.

7. Chan, H. Y. H.; Zou, S.; Weaver, M. J., Mechanistic differences between electrochemical and gas-phase thermal oxidation of platinum-group transition metals as discerned by surface-enhanced Raman spectroscopy. *The Journal of Physical Chemistry B* **1999,** *103* (50), 11141-11151.

8. Saliba, N.; Tsai, Y.-L.; Panja, C.; Koel, B. E., Oxidation of Pt (111) by ozone (O3) under UHV conditions. *Surface science* **1999,** *419* (2-3), 79-88.

9. Saliba, N.; Parker, D.; Koel, B. E., Adsorption of oxygen on Au (111) by exposure to ozone. *Surface science* **1998,** *410* (2-3), 270-282.

10. Luo, H.; Park, S.; Chan, H. Y. H.; Weaver, M. J., Surface oxidation of platinum-group transition metals in ambient gaseous environments: role of electrochemical versus chemical pathways. *The Journal of Physical Chemistry B* **2000,** *104* (34), 8250-8258.

11. Le Rhun, V.; Garnier, E.; Pronier, S.; Alonso-Vante, N., Electrocatalysis on nanoscale ruthenium-based material manufactured by carbonyl decomposition. *Electrochemistry communications* **2000,** *2* (7), 475-479.

12. Vogel, W.; Le Rhun, V.; Garnier, E.; Alonso-Vante, N., Ru clusters synthesized chemically from dissolved carbonyl: in situ study of a novel electrocatalyst in the gas phase and in electrochemical environment. *The Journal of Physical Chemistry B* **2001,** *105* (22), 5238-5243.

13. Yang, C.-m.; Liu, P.-h.; Ho, Y.-f.; Chiu, C.-y.; Chao, K.-j., Highly dispersed metal nanoparticles in functionalized SBA-15. *Chemistry of Materials* **2003,** *15* (1), 275-280.

14. Miller, J.; Kropf, A.; Zha, Y.; Regalbuto, J.; Delannoy, L.; Louis, C.; Bus, E.; van Bokhoven, J. A., The effect of gold particle size on AuAu bond length and reactivity toward oxygen in supported catalysts. *Journal of Catalysis* **2006,** *240* (2), 222-234.

15. Vogel, W., Size contraction in Pt/C and PtRu/C commercial E-TEK electrocatalysts: An in situ X-ray diffraction study. *The Journal of Physical Chemistry C* **2008,** *112* (35), 13475-13482.

16. Rzeszotarski, P.; Kaszkur, Z., Surface reconstruction of Pt nanocrystals interacting with gas atmosphere. Bridging the pressure gap with in situ diffraction. *Physical Chemistry Chemical Physics* **2009,** *11* (26), 5416-5421.

17. Ingham, B.; Hendy, S.; Fong, D.; Fuoss, P.; Eastman, J.; Lassesson, A.; Tee, K.; Convers, P.; Brown, S.; Ryan, M., Synchrotron x-ray diffraction measurements of strain in metallic nanoparticles with oxide shells. *Journal of Physics D: Applied Physics* **2010,** *43* (7), 075301.

18. Herd, B.; Goritzka, J. C.; Over, H., Room temperature oxidation of ruthenium. *The Journal of Physical Chemistry C* **2013,** *117* (29), 15148-15154.

19. Gallagher, J. R.; Li, T.; Zhao, H.; Liu, J.; Lei, Y.; Zhang, X.; Ren, Y.; Elam, J. W.; Meyer, R. J.; Winans, R. E., In situ diffraction of highly dispersed supported platinum nanoparticles. *Catalysis Science & Technology* **2014,** *4* (9), 3053-3063.

20. Bhattacharya, P.; Nasybulin, E. N.; Engelhard, M. H.; Kovarik, L.; Bowden, M. E.; Li, X. S.; Gaspar, D. J.; Xu, W.; Zhang, J. G., Dendrimer-encapsulated ruthenium oxide nanoparticles as catalysts in lithium-oxygen batteries. *Advanced Functional Materials* **2014,** *24* (47), 7510-7519.

21. Bavand, R.; Yelon, A.; Sacher, E., X-ray photoelectron spectroscopic and morphologic studies of Ru nanoparticles deposited onto highly oriented pyrolytic graphite. *Applied Surface Science* **2015,** *355*, 279-289.

22. Banerjee, R.; Liu, Q.; Tengco, J. M. M.; Regalbuto, J. R., Detection of Ambient Oxidation of Ultrasmall Supported Platinum Nanoparticles with Benchtop Powder X-Ray Diffraction. *Catalysis Letters* **2017,** *147* (7), 1754-1764.

23. Qin, B.; Yu, H.; Chi, J.; Jia, J.; Gao, X.; Yao, D.; Yi, B.; Shao, Z., A novel Ir/CeO 2–C nanoparticle electrocatalyst for the hydrogen oxidation reaction of alkaline anion exchange membrane fuel cells. *RSC advances* **2017,** *7* (50), 31574-31581.

24. Banerjee, R.; Chen, D. A.; Karakalos, S.; Piedboeuf, M.-L. C.; Job, N.; Regalbuto, J. R., Ambient oxidation of ultrasmall platinum nanoparticles on microporous carbon catalyst supports. *ACS Applied Nano Materials* **2018,** *1* (10), 5876-5884.

25. Ye, C.; Peng, M.; Cui, T.; Tang, X.; Wang, D.; Jiao, M.; Miller, J. T.; Li, Y., Revealing the surface atomic arrangement of noble metal alkane dehydrogenation catalysts by a stepwise reduction-oxidation approach. *Nano Research* **2021**, 1-7.

26. Wong, A. P.; Kyriakidou, E. A.; Toops, T. J.; Regalbuto, J. R., The catalytic behavior of precisely synthesized Pt–Pd bimetallic catalysts for use as diesel oxidation catalysts. *Catalysis Today* **2016,** *267*, 145-156.

27. Keels, J. M.; Chen, X.; Karakalos, S.; Liang, C.; Monnier, J. R.; Regalbuto, J. R., Aqueous-Phase Hydrogenation of Succinic Acid Using Bimetallic Ir–Re/C Catalysts Prepared by Strong Electrostatic Adsorption. *ACS Catalysis* **2018,** *8* (7), 6486-6494.

28. Liu, Q.; Joshi, U. A.; Über, K.; Regalbuto, J. R., The control of Pt and Ru nanoparticle size on high surface area supports. *Physical Chemistry Chemical Physics* **2014,** *16* (48), 26431-26435.

29. Block, B.; Bailar Jr, J. C., The Reaction of Gold (III) with Some Bidentate Coördinating Groups1. *Journal of the American Chemical Society* **1951,** *73* (10), 4722-4725.

30. Noble, S. R.; Barnes, S. E.; Banerjee, R.; Miller, J.; Regalbuto, J. R., Supported nanoparticle synthesis with Au bis-Ethylenediamine: The mechanism of adsorption onto oxides and carbons. *Journal of Catalysis* **2021,** *393*, 344-356.

31. Robiche, N. *Comptage de particules*, 2.0; Laboratoire de Réactivité de Surface: Pierre and Marie Curie University.

32. Hubbel, J. H.; Seltzer, S. M., X-ray mass attenuation coefficients: NIST standard reference database 126. NIST: 2004.

33. Wojdyr, M., Fityk: a general-purpose peak fitting program. *Journal of Applied Crystallography* **2010,** *43* (5-1), 1126-1128.

34. Pitschke, W.; Hermann, H.; Mattern, N., The influence of surface roughness on diffracted X-ray intensities in Bragg–Brentano geometry and its effect on the structure determination by means of Rietveld analysis. *Powder Diffraction* **1993,** *8* (2), 74-83.

35. Pitschke, W.; Mattern, N.; Hermann, H., Incorporation of microabsorption corrections into Rietveid analysis. *Powder Diffraction* **1993,** *8* (4), 223-228.

36. Hoffman, A. S.; Singh, J. A.; Bent, S. F.; Bare, S. R., In situ observation of phase changes of a silica-supported cobalt catalyst for the Fischer–Tropsch process by the development of a synchrotron-compatible in situ/operando powder X-ray diffraction cell. *Journal of synchrotron radiation* **2018,** *25* (6), 1673-1682.

37. Asundi, A. S.; Hoffman, A. S.; Chi, M.; Nathan, S. S.; Boubnov, A.; Hong, J.; Bare, S. R.; Bent, S. F., Enhanced alcohol production over binary Mo/Co carbide catalysts in syngas conversion. *Journal of Catalysis* **2020,** *391*, 446-458.

38. Blomberg, S.; Westerström, R.; Martin, N.; Lundgren, E.; Andersen, J. N.; Messing, M.; Gustafson, J., A high pressure X-ray photoelectron spectroscopy study of oxidation and reduction of Rh (100) and Rh nanoparticles. *Surface science* **2014,** *628*, 153-158.

39. Lamber, R.; Wetjen, S.; Jaeger, N. I., Size dependence of the lattice parameter of small palladium particles. *Physical Review B* **1995,** *51* (16), 10968.

40. Du, K.; Ernst, F.; Pelsozy, M.; Barthel, J.; Tillmann, K., Expansion of interatomic distances in platinum catalyst nanoparticles. *Acta materialia* **2010,** *58* (3), 836-845.

Supplementary Information

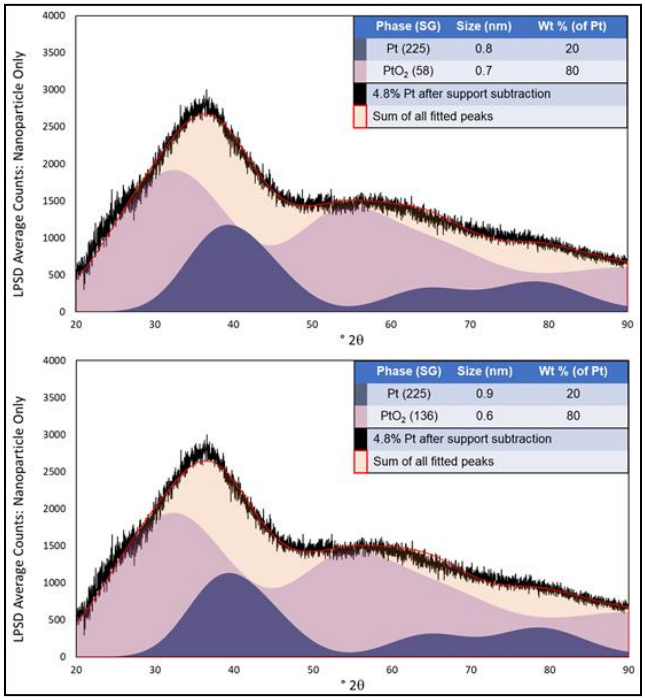

Figure 2.7. Comparing the Rietveld fits for PtO_2 (space group 58 vs. 136).

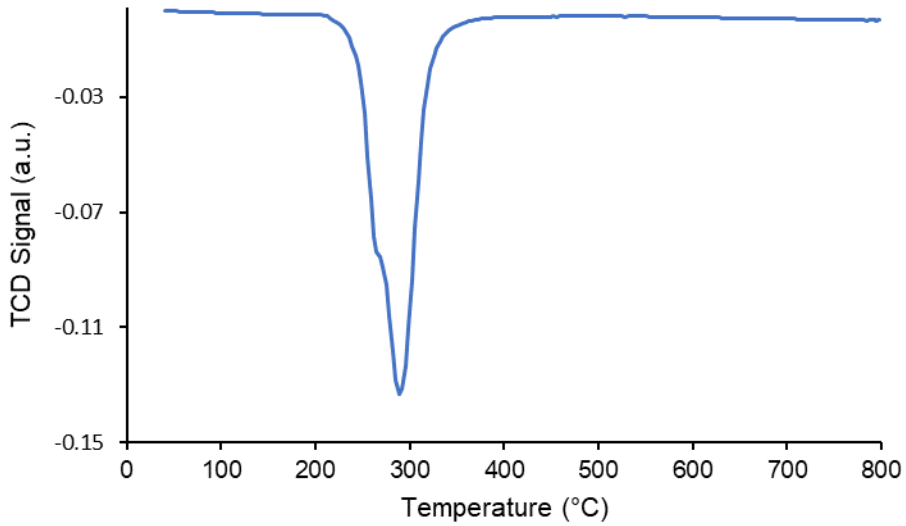

Figure 2.8. TPR profile of SEA-adsorbed Tris(ethylenediamine)rhodium (III) Chloride Trihydrate on Aerosil 300.

Table 2.5. Metal and metal oxide phases investigated for the Rietveld analysis. ICSD numbers are shown in bold.

Au	Pt	Pd	Ir	Rh	Ru
Au (225) **ICSD 52249**	Pt (225) **ICSD 52250**	Pd (164) **ICSD 40804**	Ir (225) **ICSD 64992**	Rh (191) **ICSD 259819**	Ru (194) **ICSD 52261**
Au_2O_3 (43) **ICSD 8014**	PtO (131) **ICSD 26599**	Pd (225) **ICSD 52251**	IrO_2 (136) **ICSD 84577**	Rh (225) **ICSD 52252**	RuO_2 (58) **ICSD 84619**
	PtO (225) **ICSD 105543**	Pd_2O (224) **ICSD 77651**	IrO_2 (205) **ICSD 251567**	Rh_2O_3 (60) **ICSD 41534**	RuO_2 (136) **ICSD 15071**
	PtO_2 (58) **ICSD 202407**	PdO (123) **ICSD 28837**		Rh_2O_3 (61) **ICSD 9206**	RuO_2 (205) **ICSD 66939**
	PtO_2 (136) **ICSD 647316**	PdO (131) **ICSD 24692**		Rh_2O_3 (167) **ICSD 33645**	RuO_4 (15) **ICSD 415306**
	PtO_2 (164) **ICSD 24922**	PdO (139) **ICSD 41617**		Rh_2O_3 (167) **ICSD 108941**	RuO_4 (218) **ICSD 415303**
	PtO_2 (186) **ICSD 24923**	PdO (225) **ICSD 77650**		Rh_2O_3 (167) **ICSD 647369**	
	PtO_2 (205) **ICSD 251568**	PdO_2 (136) **ICSD 647283**		RhO_2 (136) **ICSD 28498**	
	PtO_2 (224) **ICSD 77654**	$Pd_{0.5}(Pd_3O_4)$ (223) **ICSD 14033**		RhO_2 (205) **ICSD 251565**	
	Pt_3O_4 (223) **ICSD 30444**				
	Pt_3O_4 (229) **ICSD 27836**				

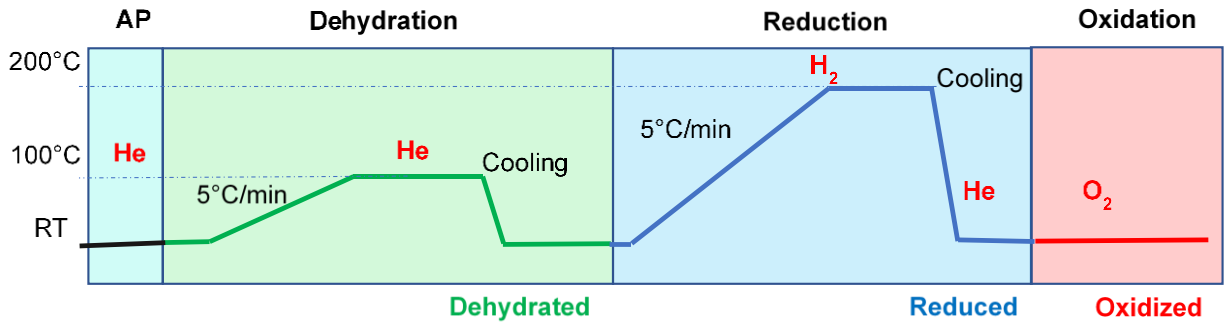

Figure 2.9. In-Situ XAS experiment.

CHAPTER 3

FUTURE WORK

Crystalline Supports

The XRD methods presented in Lipp, et al. [61] are also applicable to crystalline supports, however, some additional processing may be necessary. Figure 3.1 depicts the methods applied to a low weight-loading Pd sample (0.33% Pd) supported on Al_2O_3. Prior to subtracting the sample holder scattering and correcting for intensity effects, the Pd peaks are completely hidden behind the Al_2O_3 peaks (Figure 3.1 A,B). However, once the corrections have been made (Figure 3.1 C), the Pd peaks appear and can be analyzed (Figure 3.1 E). For the particular sample shown in Figure 3.1, pure Pd nanoparticles with an estimated size of 12 nm are fit to the data. We make two further observations for this sample: first, the absorption correction calculated from the sample mass and composition had to be manually adjusted (from $\bar{\mu}$ = 28.8 cm^{-1} to $\bar{\mu}$ = 30.5 cm^{-1}) in order to expose the Pd peaks. Second, even after manually adjusting the absorption correction the alumina peaks from the pure sample are overestimated at low angles and underestimated at high angles. The reason for these observations could be related to differences in surface roughness between the nanoparticle sample and its pure support, though further work is needed to confirm this.

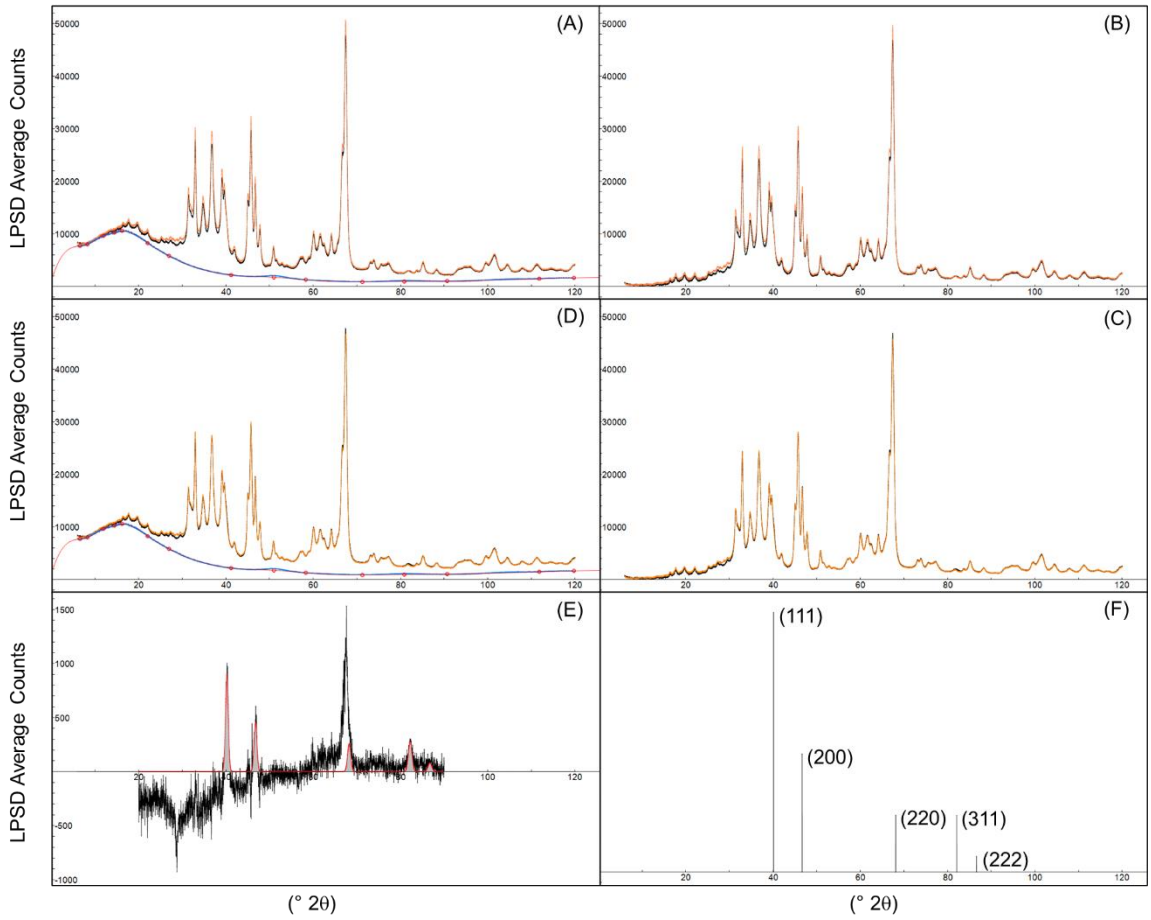

Figure 3.1 Background subtraction for 0.33% Pd / Al_2O_3. Black = 0.33% Pd / Al_2O_3, orange = pure Al_2O_3, blue = empty sample holder, red = estimated scattering from the sample holder, shaded grey = fit Pd. (A) Data after normalizing incident intensity to NIST 1976c standard and averaging six measurements (each 5° min^{-1}). (B) After subtracting the estimated scattering from the sample holder. (C) After adjusting for x-ray absorption and finite thickness. (D) With estimated sample holder scattering added back for Rietveld analysis. (E) Fit with Pd. (F) hkl lines and relative intensities for bulk Pd (ICSD PDF 01-071-3757).

One of the main physical effects that can cause samples containing crystalline phases to require extra processing is sample displacement. Sample displacement, i.e. height error, occurs when the XRD sample is vertically offset from the XRD's goniometer circle (Figure 3.2, left). Its effect on a diffractogram is to shift peaks to higher or lower angles, depending on whether the sample is above

or below the goniometer circle. The peak shift (Δ2θ) is not constant (Figure 3.2, right), but varies with the cosine of the Bragg angle θ (Dinnebier, et al. [18]):

$$\Delta 2\theta(°) = -2\left(\frac{180°}{\pi}\right)\frac{cos\theta}{R_{DS}}c \qquad \text{Equation 56}$$

where R_{DS} is the distance from the detector to sample, and c is the height error in mm. In this notation, a positive displacement shifts peaks toward higher θ and is caused by negative c (corresponding to a sample above the goniometer circle, as shown in the left side of Figure 3.2).

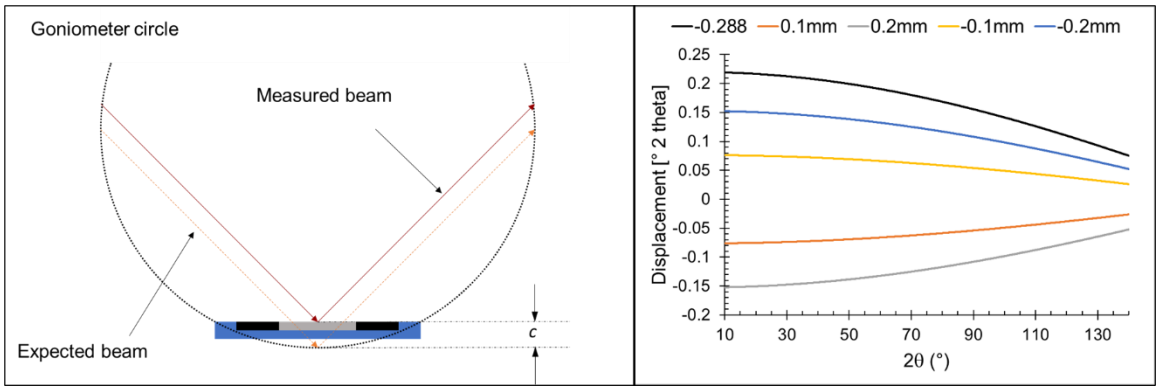

Figure 3.2 Sample displacement. Left: physical basis of height error. Right: angle-dependence of the peak shift due to varying displacements.

Figure 3.3 (A) shows a 0.72% Pt / Al_2O_3 sample with significant differences between the sample preparations of the nanoparticle sample and pure support. The sample contains much less mass (10.1 mg) than the pure support (25.4 mg), but since the differences in mass were recorded the support could still be adjusted. It is noted that, similarly to the 0.33% Pd / Al_2O_3 sample shown in Figure 3.1, the absorption coefficient $\bar{\mu}$ calculated for the nanoparticle sample had to be adjusted to make the peaks cancel out (from $\bar{\mu}$ = 12.8 cm^{-1} to $\bar{\mu}$ = 15.0 cm^{-1}). Based on the

difference in sample masses, one reason that may contribute to this discrepancy is the difference in density (the adjustments for x-ray absorption and finite thickness rely on the assumption that the density of the samples is constant). As a comparison, the 0.33% Pd / Al_2O_3 sample had a mass of 22.9 mg, and the pure Al_2O_3 had a mass of 24.6 mg; these sample masses were closer and the percent adjustment needed to manually correct for $\bar{\mu}$ was less. Future work could test this by preparing more samples with equivalent Al_2O_3 masses.

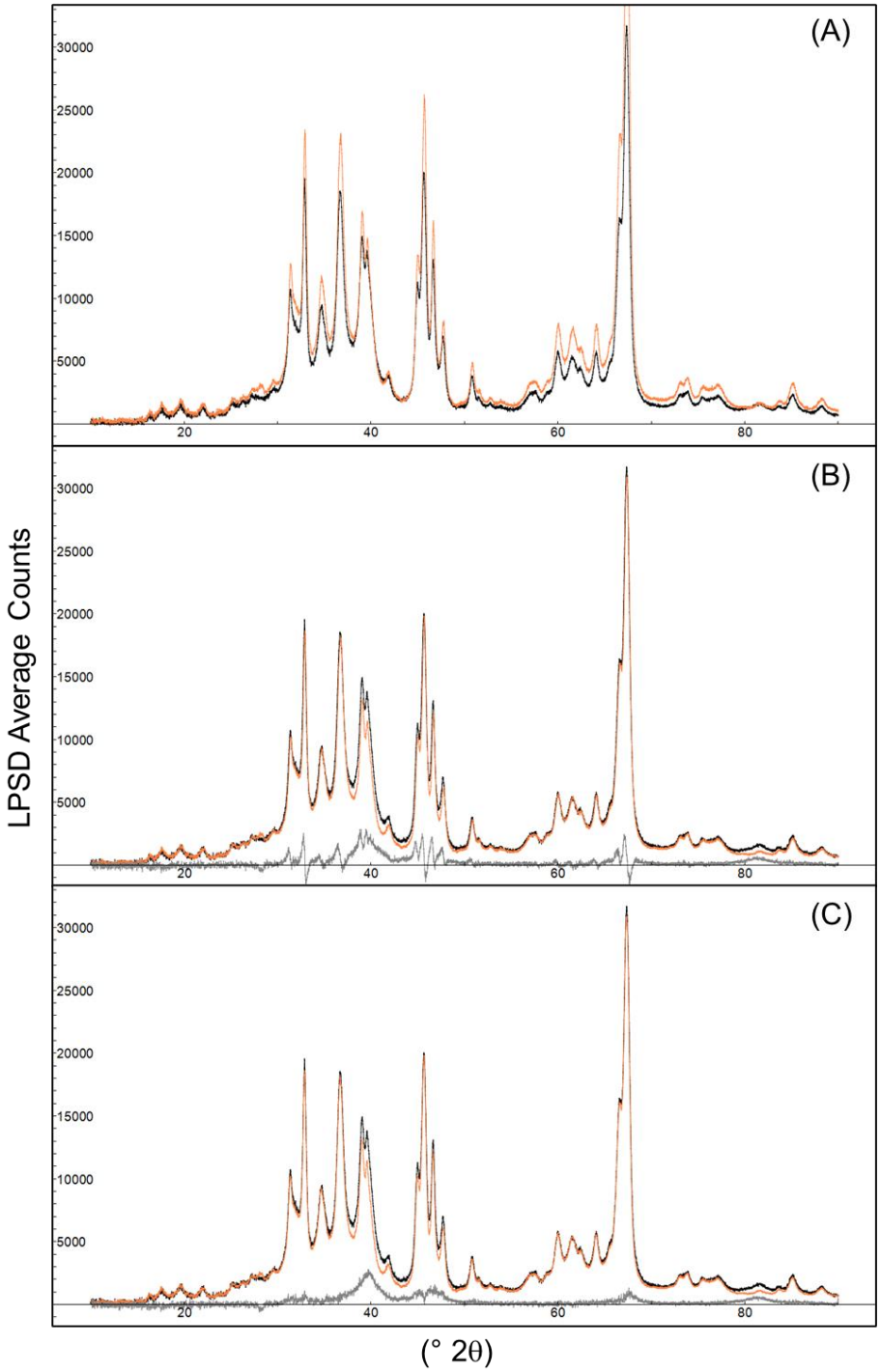

Figure 3.3 Background subtraction for 0.72% Pt / Al_2O_3. Black = 0.72% Pt / Al_2O_3, orange = pure Al_2O_3, grey = 0.72% Pt / Al_2O_3 minus pure Al_2O_3. (A) Data after normalizing incident intensity to NIST 1976c standard and subtracting the estimated scattering from the sample holder. (B) After adjusting for x-ray absorption and finite thickness, but not sample displacement. (C) After adjusting for sample displacement.

Fluorescence

Fluorescence adds another level of complexity to the analysis. The impact of fluorescence on a diffractogram is observed as an angle-independent vertical offset, as long as a constant sample volume is illuminated by the x-ray beam. The magnitude of the offset depends on the quantity and identity of the fluorescent element, and on the wavelength used. Whether or not an element fluoresces in the XRD depends directly on the wavelength of x-rays used. Figure 3.4 illustrates a rule of thumb for determining the possibility of fluorescence using the periodic table is as follows: for a given x-ray source element, the elements to the left of the source element in the periodic table will fluoresce (excluding the element directly next to the source element). For example, if a copper x-ray source is used, then cobalt will have the greatest amount of fluorescence, followed by iron, manganese, chromium, vanadium, titanium, and so on. In practice, if a monochromator is not used then the x-ray source element and the element immediately to the left of the source element (in this example, copper and nickel) will also exhibit fluorescence due to the Bremsstrahlung radiation given off by the source. Figure 3.4 also illustrates that the x-ray attenuation coefficients μ / ρ of elements are affected by fluorescence: elements that fluoresce extensively quickly attenuate the x-ray flux passing through a sample.

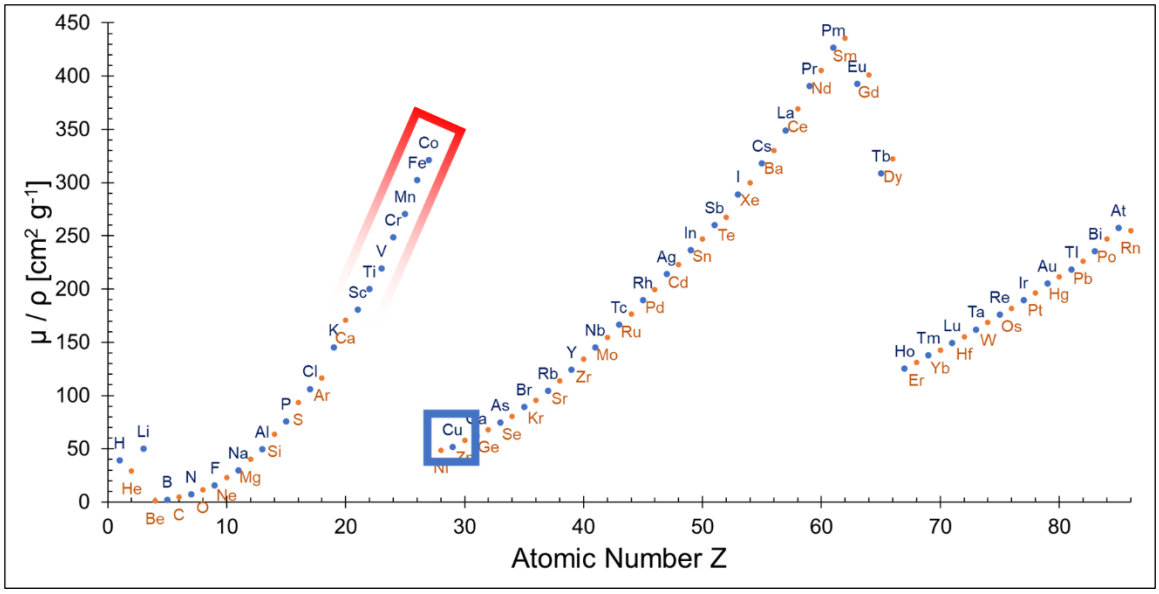

Figure 3.4. Fluorescent elements “rule of thumb” for copper K-α radiation.

The most accurate way to avoid fluorescence is to use an x-ray source that will not cause samples to fluoresce; however, this may not be easily accessible. It is therefore desirable to be able to correct diffractograms for differences in fluorescence. The assumption of constant illuminated volume means that fluorescence is also impacted by beam spill and finite sample thickness, therefore any attempts at corrections for fluorescence must account for these intensity effects. We propose the following modification to our method for separating out the support contribution: in addition to correcting the pure support’s diffractogram for differences in x-ray mass absorption and finite thickness between it and the supported nanoparticle sample, an angle independent vertical offset must also be added to the pure support that is itself multiplied by the angle-dependent beam spill and finite thickness corrections. The following sections provide examples.

Beam Spill

Figure 3.5 depicts a highly fluorescent Co_3O_4 nanopowder (Alfa Aesar) before and after the scattering from the sample holder is scattered. The offset caused by fluorescence is huge, and appears to have a significant decrease at low angles. The lower figure overlays our 2D beam spill correction onto the sample for two sample diameters: 10.13 mm (the diameter of the sample cavity) and a slightly larger 10.87 mm. The larger diameter beam spill correction matches the change in fluorescence intensity almost perfectly. Figure 3.6 shows a picture of the Co_3O_4 sample in the holder after careful preparation. The reason for the larger sample diameter is the small ring of sample that remains on the mirror surface around the sample cavity. This illustrates the need for careful sample preparation.

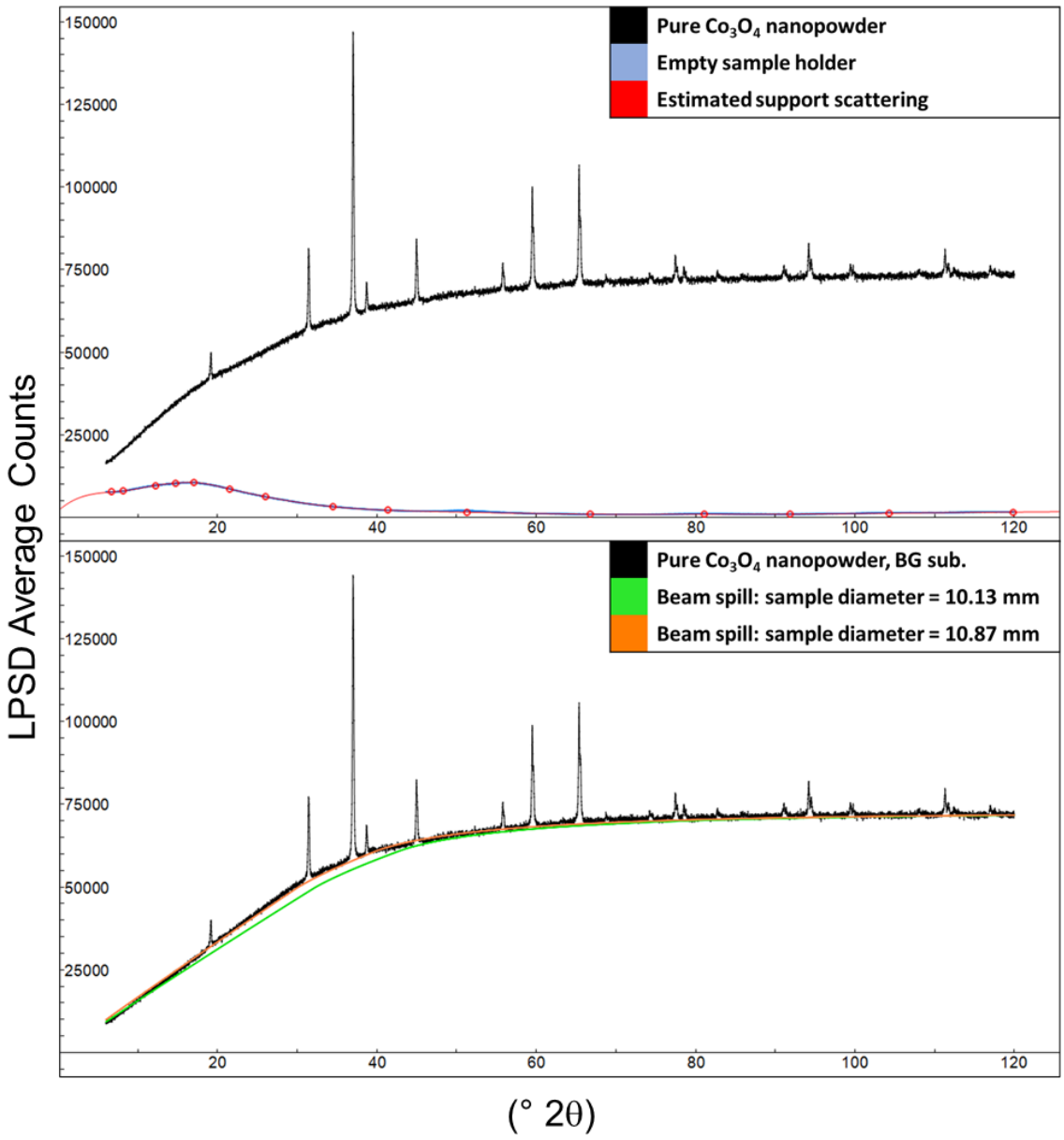

Figure 3.5 Effect of beam spill on Fluorescence.

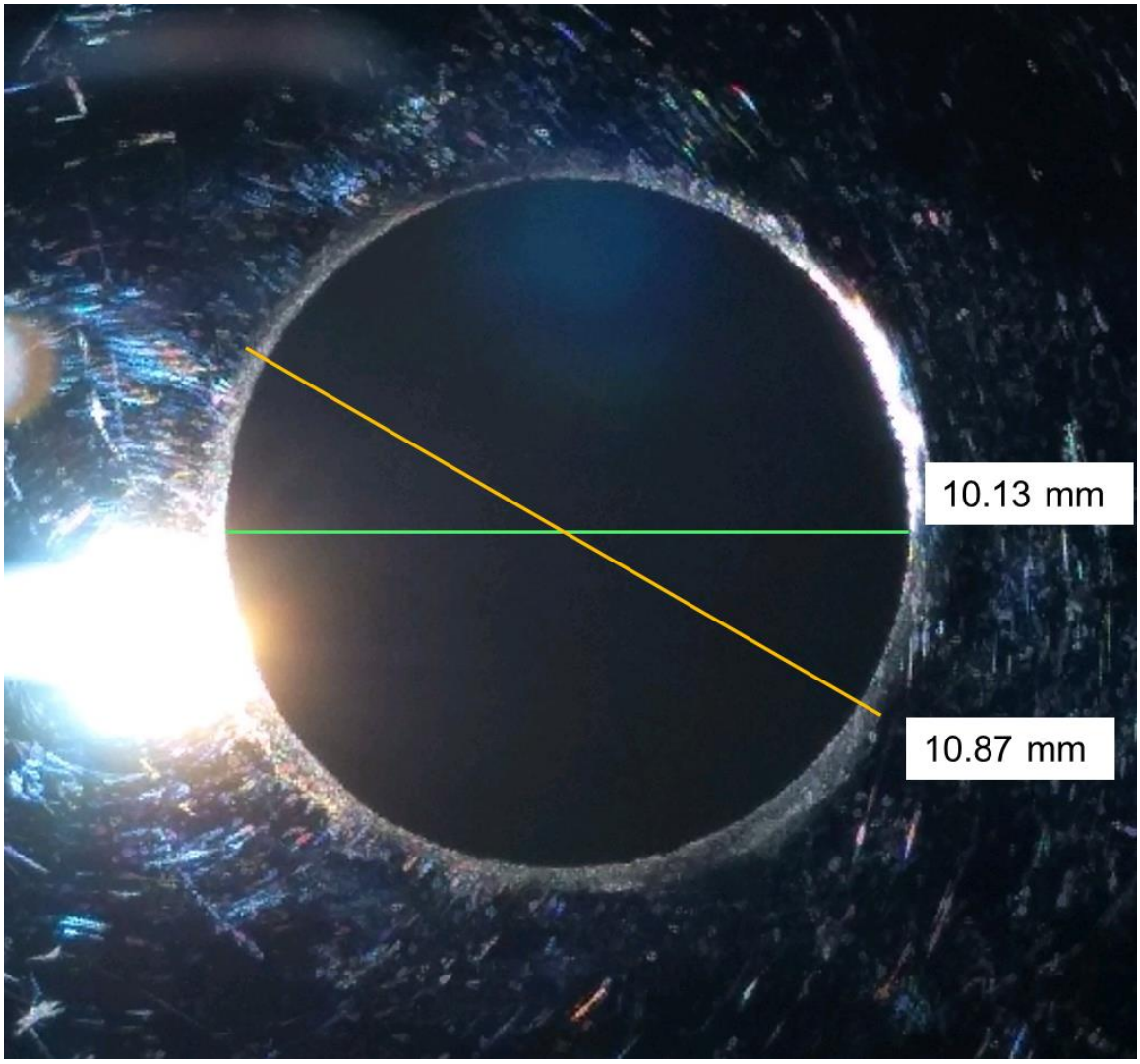

Figure 3.6 Ring of sample remaining on holder mirror after careful preparation.

Finite Thickness

The pure Co_3O_4 sample shows an angle-dependence due only to beam spill because the x-ray attenuation is so high none of the x-rays reach the bottom of the sample holder. For samples with lower x-ray attenuation, the finite thickness of the sample holder must also be considered. Figure 3.7 shows before and after such a correction is applied to a 4.2% cobalt / carbon (Ketjen Black) sample prepared with SEA (weight loading determined by ICP-OES). In this correction, the amount of

fluorescence (constant offset) is manually input based on the observed nanoparticle sample. Because the offset due to fluorescence is guessed, it is unclear whether any smaller nanoparticles are present in the sample.

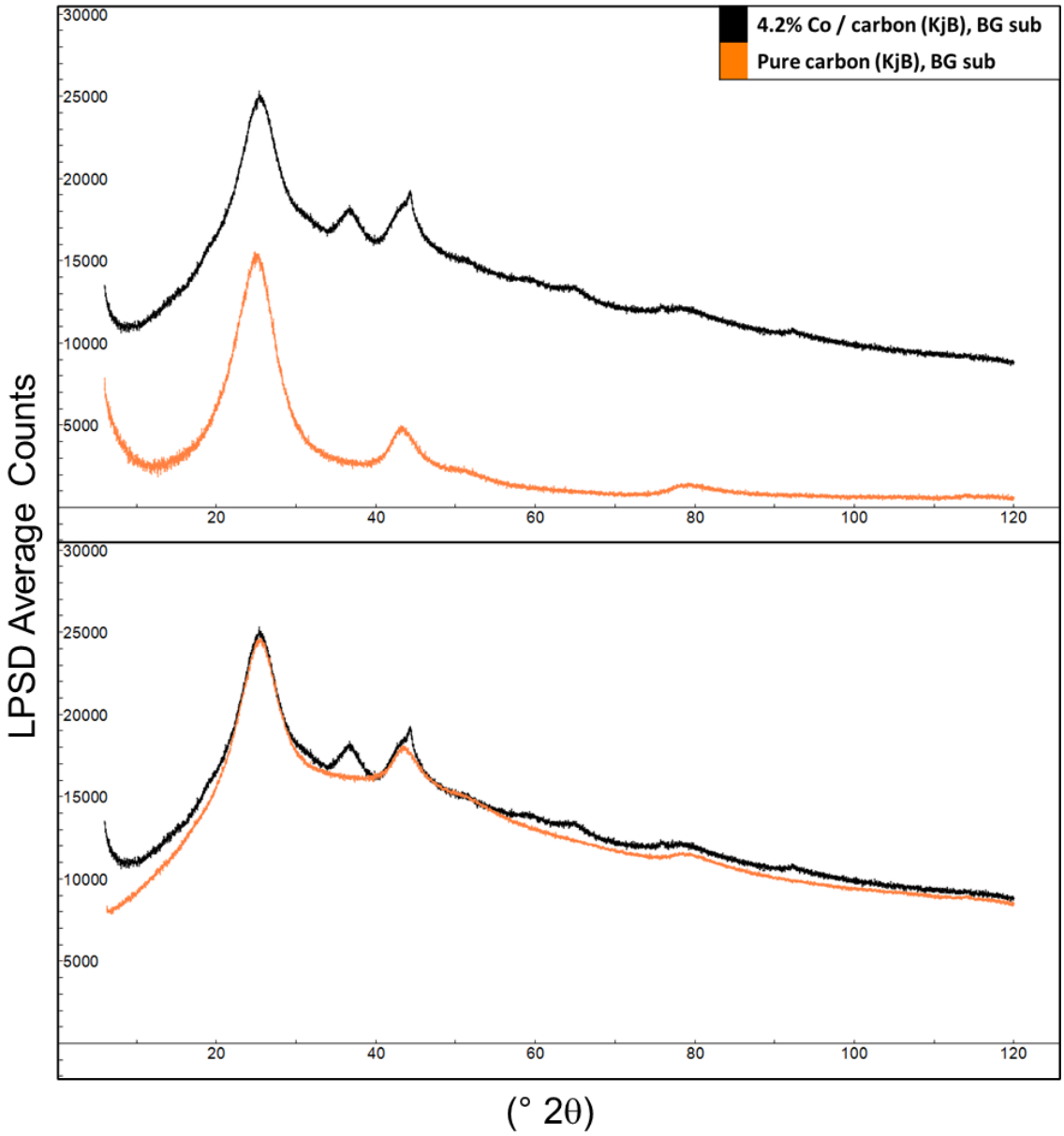

Figure 3.7 Correcting for differences in x-ray absorption, finite thickness, peak shift, and fluorescence between a pure carbon support and its cobalt sample.

Fluorescence calibration

We have attempted to calibrate the amount of fluorescence by preparing a series of samples including both physical mixtures of the Co_3O_4 nanopowder and samples prepared by dry impregnation (Figure 3.8). After normalizing the diffractograms using a NIST 1976c standard[61], the vertical offset at 120° 2θ was measured and plotted against the mass of cobalt in each sample. The results are linear and indicate a fair calibration.

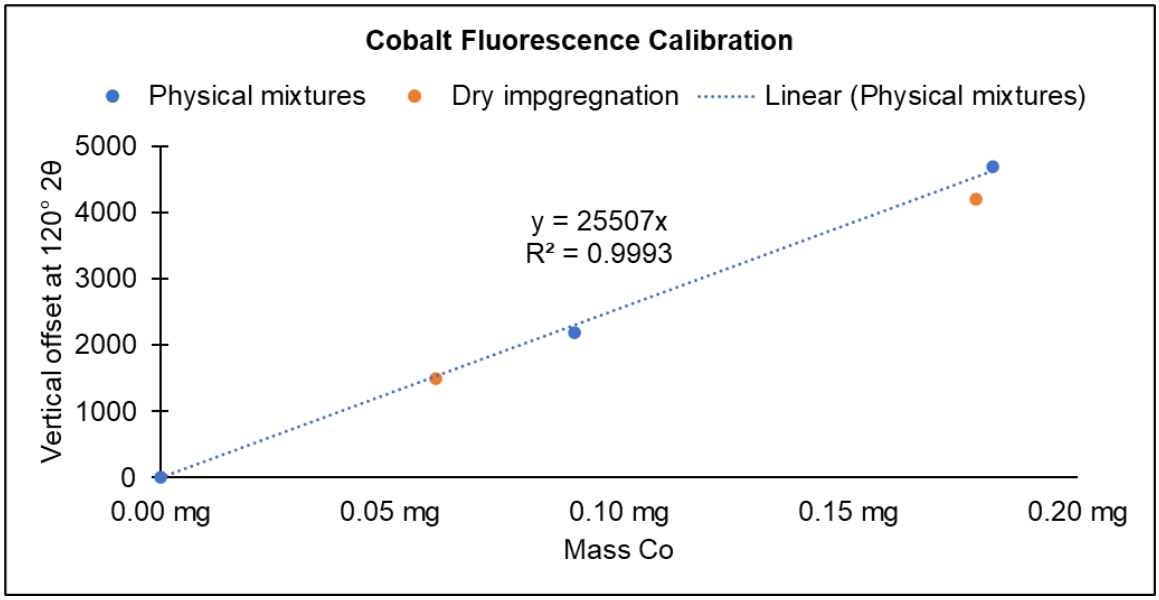

Figure 3.8 Calibration of cobalt fluorescence.

However, when this calibration is used to correct the pure support to the 4.2% Co SEA sample of Figure 3.7, the amount of fluorescence falls short. Figure 3.9 shows that the pure 4.2% Co / Ketjen Black sample is significantly offset from the supported corrected according to the calibration of Figure 3.8. A physical mixture of Co_3O_4 containing an equal amount of Co as the SEA sample is also shown, it agrees well with the corrected support.

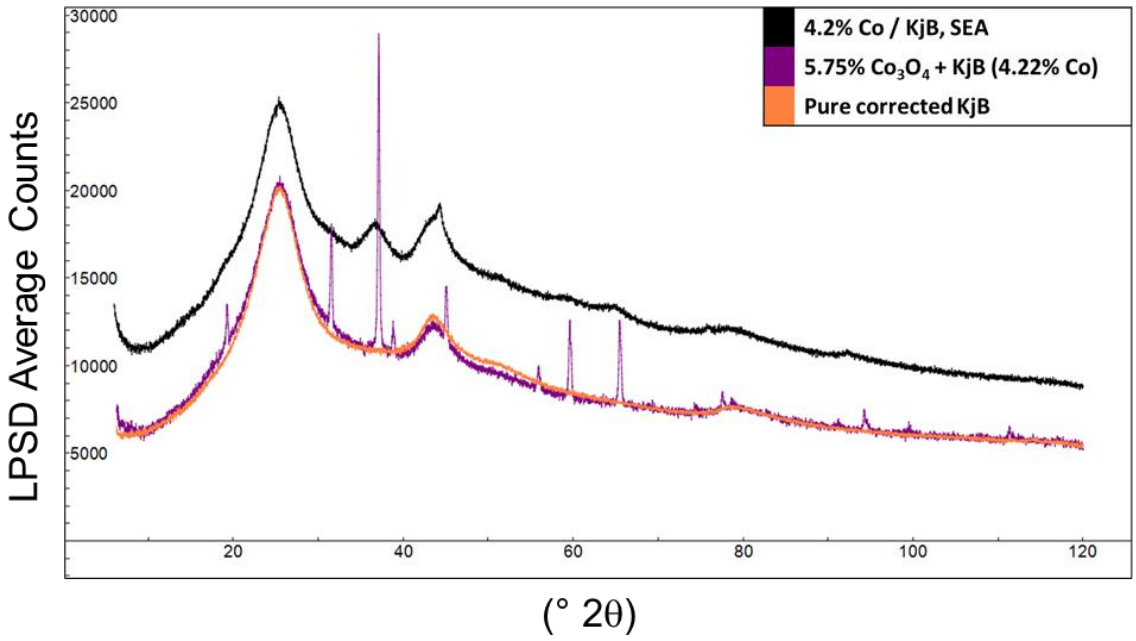

Figure 3.9 Greater fluorescence is observed for the SEA sample than what is expected from the calibration.

The reason for the apparently greater amount of fluorescence exhibited by the SEA sample is unknown. One hypothesis is that microabsorption may play a role. Microabsorption will be greater for the samples with larger Co particles, further work is needed to discern if microabsorption has a particularly strong effect on fluorescence.

Conclusion

The methods presented in chapter 1 can be extended to crystalline supports and greatly improve the analysis of such systems. An additional correction may be needed to account for any angle-dependent peak shifts caused by differences in sample displacement. Notably, the absorption corrections for our preliminary samples must be adjusted from the calculated values to match the peaks of the

crystalline phase between samples, we hypothesize that this may be due to differences in sample density resulting from the sample preparation. Further work is needed to test this hypothesis.

The methods presented in chapter 1 may also be extended to samples with fluorescent nanoparticles. The support contribution for such a sample may be approximated by multiplying an angle independent vertical shift by the 2D beam spill and finite thickness correction factors. The amount of vertical shift required for the correction seems to have a size dependence: smaller particles appear to display more fluorescence than larger particles. Further work is needed to confirm this.

CONCLUSIONS

Bragg diffraction via benchtop XRD can be used to characterize sub-nm crystallites – much smaller than what is commonly reported in the literature. Characterization is possible even when multiple phases are present – i.e. the particles do not need to be fully reduced. This increased ability of XRD is afforded by the careful accounting of intensity effects and is further enhanced by the enhanced signal-to-noise provided by solid state detectors.

Using the methods presented in Chapter 1, benchtop XRD is then used to characterize the oxidation of noble metals (Pt, Pd, Ir, Rh, Ru) under ambient conditions. Au is not observed to oxidize, though this could be due to the low weight loading (0.8%) resulting in any oxide being below the detection limit. The room temperature oxidation of these metals is a function of particle size; oxidation begins at the surface and tends to form an oxide shell around a metallic core unless the entire particle is oxidized – as is the case with Ru. Surface oxidation appears to expand the lattice parameter of the metallic core in core-shell particles; lattice contraction is observed for the Au sample, consistent with reduced nanoparticles. In-situ XANES reveals that the room temperature oxidation / reduction kinetics of these systems are quick, on the order of minutes. Future work is needed to examine the oxidation mechanism, including the role that water may play.

The methods presented in chapter 1 can be extended to crystalline supports and greatly improve the analysis of such systems. An additional correction may be needed to account for any angle-dependent peak shifts caused by differences in sample displacement. Notably, the absorption corrections for our preliminary samples must be adjusted from the calculated values to match the peaks of the crystalline phase between samples, we hypothesize that this may be due to differences in sample density resulting from the sample preparation. Further work is needed to test this hypothesis.

The methods presented in chapter 1 may also be extended to samples with fluorescent nanoparticles. The support contribution for such a sample may be approximated by multiplying an angle independent vertical shift by the 2D beam spill and finite thickness correction factors. The amount of vertical shift required for the correction seems to have a size dependence: smaller particles appear to display more fluorescence than larger particles. Further work is needed to confirm this.

Overall, these results demonstrate the ability of Bragg diffraction via Rietveld refinement to provide useful information for the characterization of ultra-small nanoparticles.

REFERENCES

1. Wong, A.; Liu, Q.; Griffin, S.; Nicholls, A.; Regalbuto, J., Synthesis of ultrasmall, homogeneously alloyed, bimetallic nanoparticles on silica supports. *Science* **2017,** *358* (6369), 1427-1430.

2. Miller, J.; Kropf, A.; Zha, Y.; Regalbuto, J.; Delannoy, L.; Louis, C.; Bus, E.; van Bokhoven, J. A., The effect of gold particle size on AuAu bond length and reactivity toward oxygen in supported catalysts. *Journal of Catalysis* **2006,** *240* (2), 222-234.

3. Gallagher, J. R.; Li, T.; Zhao, H.; Liu, J.; Lei, Y.; Zhang, X.; Ren, Y.; Elam, J. W.; Meyer, R. J.; Winans, R. E., In situ diffraction of highly dispersed supported platinum nanoparticles. *Catalysis Science & Technology* **2014,** *4* (9), 3053-3063.

4. O'Connell, K.; Regalbuto, J. R., High sensitivity silicon slit detectors for 1 nm powder XRD size detection limit. *Catalysis Letters* **2015,** *145* (3), 777-783.

5. Bazin, D.; Guczi, L.; Lynch, J., Anomalous wide angle X-ray scattering (AWAXS) and heterogeneous catalysts. *Applied Catalysis A: General* **2002,** *226* (1-2), 87-113.

6. Cromer, D. T.; Liberman, D., Relativistic calculation of anomalous scattering factors for X rays. *The Journal of Chemical Physics* **1970,** *53* (5), 1891-1898.

7. Cromer, D. T.; Liberman, D. A., Anomalous dispersion calculations near to and on the long-wavelength side of an absorption edge. *Acta Crystallographica Section A: Crystal Physics, Diffraction, Theoretical and General Crystallography* **1981,** *37* (2), 267-268.

8. Gallezot, P.; Avalos-Borja, M.; Poppa, H.; Heinemann, K., Structure and morphology characterization of nanometer-size metal aggregates by electron scattering patterns. *Langmuir* **1985,** *1* (3), 342-347.

9. Vogel, W.; Sachtler, W.; Zhang, Z., Formation of Metal Clusters in Zeolites Studied by Differential X-Ray Scattering. *Berichte der Bunsengesellschaft für physikalische Chemie* **1993,** *97* (3), 280-285.

10. Gnutzmann, V.; Vogel, W., Structural sensitivity of the standard platinum/silica catalyst EuroPt-1 to hydrogen and oxygen exposure by in situ X-ray diffraction. *Journal of Physical Chemistry* **1990,** *94* (12), 4991-4997.

11. Vogel, W.; Le Rhun, V.; Garnier, E.; Alonso-Vante, N., Ru clusters synthesized chemically from dissolved carbonyl: in situ study of a novel electrocatalyst in the gas phase and in electrochemical environment. *The Journal of Physical Chemistry B* **2001,** *105* (22), 5238-5243.

12. Vogel, W., Size contraction in Pt/C and PtRu/C commercial E-TEK electrocatalysts: An in situ X-ray diffraction study. *The Journal of Physical Chemistry C* **2008,** *112* (35), 13475-13482.

13. *TOPAS*, V.6.0; Bruker AXS: 2018.

14. Hubbel, J. H.; Seltzer, S. M., X-ray mass attenuation coefficients: NIST standard reference database 126. NIST: 2004.

15. Hermann, H.; Ermrich, M., Microabsorption correction of X-ray intensities diffracted by multiphase powder specimens. *Powder diffraction* **1989,** *4* (4), 189-195.

16. Zevin, L. S.; Kimmel, G.; Mureinik, I., Methodology of quantitative phase analysis. In *Quantitative X-Ray Diffractometry*, Springer: 1995; pp 100-225.

17. Brindley, G. W., XLV. The effect of grain or particle size on x-ray reflections from mixed powders and alloys, considered in relation to the quantitative determination of crystalline substances by x-ray methods. *The London, Edinburgh, and Dublin Philosophical Magazine and Journal of Science* **1945,** *36* (256), 347-369.

18. Dinnebier, R. E.; Leineweber, A.; Evans, J. S. O., *Rietveld refinement: practical powder diffraction pattern analysis using Topas*. Walter de Gruyter GmbH: Berlin/Boston, 2019.

19. Pecharsky, V. K.; Zavalij, P. Y., *Fundamentals of Powder Diffraction and Structural Characterization of Materials*. 2nd ed.; Springer: 2009.

20. Pitschke, W.; Mattern, N.; Hermann, H., Incorporation of microabsorption corrections into Rietveid analysis. *Powder Diffraction* **1993,** *8* (4), 223-228.

21. Hermann, H.; Ermrich, M., Microabsorption of X-ray intensity in randomly packed powder specimens. *Acta Crystallographica Section A: Foundations of Crystallography* **1987,** *43* (3), 401-405.

22. Harrison, R. J.; Paskin, A., The effects of granularity on the diffracted intensity in powders. *Acta Crystallographica* **1964,** *17* (4), 325-331.

23. Suortti, P., Effects of porosity and surface roughness on the X-ray intensity reflected from a powder specimen. *Journal of Applied Crystallography* **1972,** *5* (5), 325-331.

24. Pitschke, W.; Hermann, H.; Mattern, N., The influence of surface roughness on diffracted X-ray intensities in Bragg–Brentano geometry and its effect on the structure determination by means of Rietveld analysis. *Powder Diffraction* **1993,** *8* (2), 74-83.

25. Schreier, M.; Regalbuto, J. R., A fundamental study of Pt tetraammine impregnation of silica: 1. The electrostatic nature of platinum adsorption. *Journal of Catalysis* **2004,** *225* (1), 190-202.

26. Miller, J. T.; Schreier, M.; Kropf, A. J.; Regalbuto, J. R., A fundamental study of platinum tetraammine impregnation of silica: 2. The effect of method of preparation, loading, and calcination temperature on (reduced) particle size. *Journal of Catalysis* **2004,** *225* (1), 203-212.

27. Xia, Y.; Harrison, P.; Ornelas, I.; Wang, H.; Li, Z., HAADF-STEM image analysis for size-selected platinum nanoclusters. *Journal of microscopy* **2020,** *279* (3), 229-233.

28. Wojdyr, M., Fityk: a general-purpose peak fitting program. *Journal of Applied Crystallography* **2010,** *43* (5-1), 1126-1128.

29. Bucher, J.; Buttet, J.; Van der Klink, J.; Graetzel, M., Electronic properties and local densities of states in clean and hydrogen covered Pt particles. *Surface Science* **1989,** *214* (3), 347-357.

30. Banerjee, R.; Liu, Q.; Tengco, J. M. M.; Regalbuto, J. R., Detection of Ambient Oxidation of Ultrasmall Supported Platinum Nanoparticles with Benchtop Powder X-Ray Diffraction. *Catalysis Letters* **2017,** *147* (7), 1754-1764.

31. Lamber, R.; Wetjen, S.; Jaeger, N. I., Size dependence of the lattice parameter of small palladium particles. *Physical Review B* **1995,** *51* (16), 10968.

32. Goyhenex, C.; Henry, C.; Urban, J., In-situ measurements of the lattice parameter of supported palladium clusters. *Philosophical Magazine A* **1994,** *69* (6), 1073-1084.

33. Jacobs, J.; Schryvers, D., A high-resolution electron microscopy study of photodeposited Pd particles on TiO2 and their oxidation in air. *Journal of Catalysis* **1987,** *103* (2), 436-449.

34. Du, K.; Ernst, F.; Pelsozy, M.; Barthel, J.; Tillmann, K., Expansion of interatomic distances in platinum catalyst nanoparticles. *Acta materialia* **2010,** *58* (3), 836-845.

35. Momma, K.; Izumi, F., VESTA 3 for three-dimensional visualization of crystal, volumetric and morphology data. *Journal of applied crystallography* **2011,** *44* (6), 1272-1276.

36. Ahmadi, M.; Timoshenko, J.; Behafarid, F.; Roldan Cuenya, B., Tuning the structure of Pt nanoparticles through support interactions: an in situ polarized X-ray absorption study coupled with atomistic simulations. *The Journal of Physical Chemistry C* **2019,** *123* (16), 10666-10676.

37. Ankudinov, A.; Rehr, J.; Low, J. J.; Bare, S. R., Sensitivity of Pt x-ray absorption near edge structure to the morphology of small Pt clusters. *The Journal of chemical physics* **2002,** *116* (5), 1911-1919.

38. Frenkel, A. I.; Hills, C. W.; Nuzzo, R. G., A view from the inside: complexity in the atomic scale ordering of supported metal nanoparticles. *The Journal of Physical Chemistry B* **2001,** *105* (51), 12689-12703.

39. Daniel, O. M.; DeLaRiva, A.; Kunkes, E. L.; Datye, A. K.; Dumesic, J. A.; Davis, R. J., X-ray Absorption Spectroscopy of Bimetallic Pt–Re Catalysts for Hydrogenolysis of Glycerol to Propanediols. *ChemCatChem* **2010,** *2* (9), 1107-1114.

40. Jeong, E.-S.; Park, C.-I.; Jin, Z.; Hwang, I.-H.; Son, J.-K.; Kim, M.-Y.; Choi, J.-S.; Han, S.-W., Temperature-Dependent Local Structural Properties of Redox Pt Nanoparticles on TiO 2 and ZrO 2 Supports. *Catalysis Letters* **2015,** *145* (3), 971-983.

41. Chen, J. Z.; Gao, J.; Probus, P. R.; Liu, W.; Wu, X.; Wegener, E. C.; Kropf, A. J.; Zemlyanov, D.; Zhang, G.; Yang, X., The effect of strong metal–support interaction (SMSI) on Pt–Ti/SiO 2 and Pt–Nb/SiO 2 catalysts for propane dehydrogenation. *Catalysis Science & Technology* **2020,** *10* (17), 5973-5982.

42. Frenkel, A. I.; Yevick, A.; Cooper, C.; Vasic, R., Modeling the structure and composition of nanoparticles by extended X-ray absorption fine-structure spectroscopy. *Annual Review of Analytical Chemistry* **2011,** *4*, 23-39.

43. Jentys, A., Estimation of mean size and shape of small metal particles by EXAFS. *Physical Chemistry Chemical Physics* **1999,** *1* (17), 4059-4063.

44. Beale, A. M.; Weckhuysen, B. M., EXAFS as a tool to interrogate the size and shape of mono and bimetallic catalyst nanoparticles. *Physical Chemistry Chemical Physics* **2010,** *12* (21), 5562-5574.

45. Marinkovic, N. S.; Sasaki, K.; Adzic, R. R., Determination of single-and multi-component nanoparticle sizes by X-ray absorption spectroscopy. *Journal of The Electrochemical Society* **2018,** *165* (15), J3222-J3230.

46. Wu, Z.; Wegener, E. C.; Tseng, H.-T.; Gallagher, J. R.; Harris, J. W.; Diaz, R. E.; Ren, Y.; Ribeiro, F. H.; Miller, J. T., Pd–In intermetallic alloy nanoparticles: highly selective ethane dehydrogenation catalysts. *Catalysis Science & Technology* **2016,** *6* (18), 6965-6976.

47. Ma, Z.; Wu, Z.; Miller, J. T., Effect of Cu content on the bimetallic Pt–Cu catalysts for propane dehydrogenation. *Catalysis, Structure & Reactivity* **2017,** *3* (1-2), 43-53.

48. Wu, Z.; Bukowski, B. C.; Li, Z.; Milligan, C.; Zhou, L.; Ma, T.; Wu, Y.; Ren, Y.; Ribeiro, F. H.; Delgass, W. N., Changes in catalytic and adsorptive properties of 2 nm Pt3Mn nanoparticles by subsurface atoms. *Journal of the American Chemical Society* **2018,** *140* (44), 14870-14877.

49. Lipp, J. W. Fine Points for Broad Bumps: the Extension of Rietveld Refinement for Benchtop Powder XRD Analysis of Ultra-small Supported Nanoparticles. University of South Carolina, 2021.

50. Bertolotti, F.; Moscheni, D.; Guagliardi, A.; Masciocchi, N., When Crystals Go Nano–The Role of Advanced X-ray Total Scattering Methods in Nanotechnology. *European Journal of Inorganic Chemistry* **2018,** *2018* (34), 3789-3803.

51. Pakharukova, V. P.; Yatsenko, D. A.; Gerasimov, E. Y.; Vlasova, E.; Bukhtiyarova, G. A.; Tsybulya, S. V., Total Scattering Debye Function Analysis: Effective Approach for Structural Studies of Supported MoS2-Based Hydrotreating Catalysts. *Industrial & Engineering Chemistry Research* **2020,** *59* (23), 10914-10922.

52. Kaszkur, Z. In *Test of applicability of some powder diffraction tools to nanocrystals*, Ninth European Powder Diffraction Conference, Oldenbourg Wissenschaftsverlag: 2015; pp 147-154.

53. Block, B.; Bailar Jr, J. C., The Reaction of Gold (III) with Some Bidentate Coördinating Groups1. *Journal of the American Chemical Society* **1951,** *73* (10), 4722-4725.

54. Noble, S. R.; Barnes, S. E.; Banerjee, R.; Miller, J.; Regalbuto, J. R., Supported nanoparticle synthesis with Au bis-Ethylenediamine: The mechanism of adsorption onto oxides and carbons. *Journal of Catalysis* **2021,** *393*, 344-356.

55. Mendenhall, M. H.; Henins, A.; Hudson, L. T.; Szabo, C. I.; Windover, D.; Cline, J. P., High-precision measurement of the x-ray Cu Kα spectrum. *Journal of Physics B: Atomic, Molecular and Optical Physics* **2017,** *50* (11), 115004.

56. Hoffman, A. S.; Singh, J. A.; Bent, S. F.; Bare, S. R., In situ observation of phase changes of a silica-supported cobalt catalyst for the Fischer–Tropsch

process by the development of a synchrotron-compatible in situ/operando powder X-ray diffraction cell. *Journal of synchrotron radiation* **2018,** *25* (6), 1673-1682.

57. Asundi, A. S.; Hoffman, A. S.; Chi, M.; Nathan, S. S.; Boubnov, A.; Hong, J.; Bare, S. R.; Bent, S. F., Enhanced alcohol production over binary Mo/Co carbide catalysts in syngas conversion. *Journal of Catalysis* **2020,** *391*, 446-458.

58. Ravel, B.; Newville, M., ATHENA, ARTEMIS, HEPHAESTUS: data analysis for X-ray absorption spectroscopy using IFEFFIT. *Journal of synchrotron radiation* **2005,** *12* (4), 537-541.

59. Lytle, F., Report of the international workshop on standard and criteria in x-ray absorption spectoroscopy. *Physica* **1989,** *158*, 701-722.

60. rowlesmr; AlanCoelho, LP_Factor_X. In *Forum>Topas*, Topas Forum: 2019.

61. Lipp, J.; Banerjee, R.; Patwary, M. D. F.; Patra, N.; Dong, A.; Girgsdies, F.; Bare, S. R.; Regalbuto, J. R., The extension of Rietveld refinement for benchtop powder XRD analysis of ultra-small supported nanoparticles *Chemistry of Materials* **In Preparation**.

62. Rhodes, H. E.; Wang, P.-K.; Stokes, H. T.; Slichter, C. P.; Sinfelt, J., NMR of platinum catalysts. I. Line shapes. *Physical Review B* **1982,** *26* (7), 3559.

63. Martens, J.; Prins, R.; Koningsberger, D., Controlled oxygen chemisorption on an alumina supported rhodium catalyst. The formation of a new metal-metal oxide interface determined with EXAFS. *The Journal of Physical Chemistry* **1989,** *93* (8), 3179-3185.

64. Tong, Y.; van der Klink, J., Local metal to non-metal transition on oxygen-covered platinum particles from 195Pt nuclear magnetic resonance. *Journal of Physics: Condensed Matter* **1995,** *7* (12), 2447.

65. Chan, H. Y. H.; Zou, S.; Weaver, M. J., Mechanistic differences between electrochemical and gas-phase thermal oxidation of platinum-group transition metals as discerned by surface-enhanced Raman spectroscopy. *The Journal of Physical Chemistry B* **1999,** *103* (50), 11141-11151.

66. Saliba, N.; Tsai, Y.-L.; Panja, C.; Koel, B. E., Oxidation of Pt (111) by ozone (O3) under UHV conditions. *Surface science* **1999,** *419* (2-3), 79-88.

67. Saliba, N.; Parker, D.; Koel, B. E., Adsorption of oxygen on Au (111) by exposure to ozone. *Surface science* **1998,** *410* (2-3), 270-282.

68. Luo, H.; Park, S.; Chan, H. Y. H.; Weaver, M. J., Surface oxidation of platinum-group transition metals in ambient gaseous environments: role of

electrochemical versus chemical pathways. *The Journal of Physical Chemistry B* **2000,** *104* (34), 8250-8258.

69. Le Rhun, V.; Garnier, E.; Pronier, S.; Alonso-Vante, N., Electrocatalysis on nanoscale ruthenium-based material manufactured by carbonyl decomposition. *Electrochemistry communications* **2000,** *2* (7), 475-479.

70. Yang, C.-m.; Liu, P.-h.; Ho, Y.-f.; Chiu, C.-y.; Chao, K.-j., Highly dispersed metal nanoparticles in functionalized SBA-15. *Chemistry of Materials* **2003,** *15* (1), 275-280.

71. Rzeszotarski, P.; Kaszkur, Z., Surface reconstruction of Pt nanocrystals interacting with gas atmosphere. Bridging the pressure gap with in situ diffraction. *Physical Chemistry Chemical Physics* **2009,** *11* (26), 5416-5421.

72. Ingham, B.; Hendy, S.; Fong, D.; Fuoss, P.; Eastman, J.; Lassesson, A.; Tee, K.; Convers, P.; Brown, S.; Ryan, M., Synchrotron x-ray diffraction measurements of strain in metallic nanoparticles with oxide shells. *Journal of Physics D: Applied Physics* **2010,** *43* (7), 075301.

73. Herd, B.; Goritzka, J. C.; Over, H., Room temperature oxidation of ruthenium. *The Journal of Physical Chemistry C* **2013,** *117* (29), 15148-15154.

74. Bhattacharya, P.; Nasybulin, E. N.; Engelhard, M. H.; Kovarik, L.; Bowden, M. E.; Li, X. S.; Gaspar, D. J.; Xu, W.; Zhang, J. G., Dendrimer-encapsulated ruthenium oxide nanoparticles as catalysts in lithium-oxygen batteries. *Advanced Functional Materials* **2014,** *24* (47), 7510-7519.

75. Bavand, R.; Yelon, A.; Sacher, E., X-ray photoelectron spectroscopic and morphologic studies of Ru nanoparticles deposited onto highly oriented pyrolytic graphite. *Applied Surface Science* **2015,** *355*, 279-289.

76. Qin, B.; Yu, H.; Chi, J.; Jia, J.; Gao, X.; Yao, D.; Yi, B.; Shao, Z., A novel Ir/CeO 2–C nanoparticle electrocatalyst for the hydrogen oxidation reaction of alkaline anion exchange membrane fuel cells. *RSC advances* **2017,** *7* (50), 31574-31581.

77. Banerjee, R.; Chen, D. A.; Karakalos, S.; Piedboeuf, M.-L. C.; Job, N.; Regalbuto, J. R., Ambient oxidation of ultrasmall platinum nanoparticles on microporous carbon catalyst supports. *ACS Applied Nano Materials* **2018,** *1* (10), 5876-5884.

78. Ye, C.; Peng, M.; Cui, T.; Tang, X.; Wang, D.; Jiao, M.; Miller, J. T.; Li, Y., Revealing the surface atomic arrangement of noble metal alkane dehydrogenation catalysts by a stepwise reduction-oxidation approach. *Nano Research* **2021**, 1-7.

79. Wong, A. P.; Kyriakidou, E. A.; Toops, T. J.; Regalbuto, J. R., The catalytic behavior of precisely synthesized Pt–Pd bimetallic catalysts for use as diesel oxidation catalysts. *Catalysis Today* **2016,** *267*, 145-156.

80. Keels, J. M.; Chen, X.; Karakalos, S.; Liang, C.; Monnier, J. R.; Regalbuto, J. R., Aqueous-Phase Hydrogenation of Succinic Acid Using Bimetallic Ir–Re/C Catalysts Prepared by Strong Electrostatic Adsorption. *ACS Catalysis* **2018,** *8* (7), 6486-6494.

81. Liu, Q.; Joshi, U. A.; Über, K.; Regalbuto, J. R., The control of Pt and Ru nanoparticle size on high surface area supports. *Physical Chemistry Chemical Physics* **2014,** *16* (48), 26431-26435.

82. Robiche, N. *Comptage de particules*, 2.0; Laboratoire de Réactivité de Surface: Pierre and Marie Curie University.

83. Blomberg, S.; Westerström, R.; Martin, N.; Lundgren, E.; Andersen, J. N.; Messing, M.; Gustafson, J., A high pressure X-ray photoelectron spectroscopy study of oxidation and reduction of Rh (100) and Rh nanoparticles. *Surface science* **2014,** *628*, 153-158.